unclassified

SECURITY CLASSIFICATION OF THIS PAGE (When Data Entered)

REPORT DOCUMENTATION PAGE		READ INSTRUCTIONS BEFORE COMPLETING FORM
1. REPORT NUMBER Technical Report No. 25	2. GOVT ACCESSION NO.	3. RECIPIENT'S CATALOG NUMBER
4. TITLE (and Subtitle) Noise and Chaos in Driven Josephson Junctions		5. TYPE OF REPORT & PERIOD COVERED 6. PERFORMING ORG. REPORT NUMBER
7. AUTHOR(s) Qing Hu		8. CONTRACT OR GRANT NUMBER(s) N00014-83-K-0383 N00014-84-K-0465
9. PERFORMING ORGANIZATION NAME AND ADDRESS		10. PROGRAM ELEMENT, PROJECT, TASK AREA & WORK UNIT NUMBERS
11. CONTROLLING OFFICE NAME AND ADDRESS Division of Applied Sciences Harvard University Cambridge, MA 02138		12. REPORT DATE March, 1987 13. NUMBER OF PAGES 183
14. MONITORING AGENCY NAME & ADDRESS(If different from Controlling Office)		15. SECURITY CLASS. (of this report) unclassified 15a. DECLASSIFICATION/DOWNGRADING SCHEDULE

16. DISTRIBUTION STATEMENT (of this Report)

Reproduction in whole or in part is permitted for any purpose of the United States Government. Approved for public release; distribution unlimited.

17. DISTRIBUTION STATEMENT (of the abstract entered in Block 20, if different from Report)

18. SUPPLEMENTARY NOTES

19. KEY WORDS (Continue on reverse side if necessary and identify by block number)

Josephson junctions
laser radiation
noise sources

20. ABSTRACT (Continue on reverse side if necessary and identify by block number)

We have studied in detail the response of several Nb-aSi-Nb junctions to laser radiation at far-infrared frequencies, 245, 419, and 604 GHz. All these Nb-aSi-Nb junctions were made by the SNAP (Selective Niobium Anodization Process) procedure on a single wafer. They all have the plasma frequency $f_p=(2eI_c/\hbar C)^{1/2}/2\pi$ about 400 GHz. When we irradiate the junctions at 419 GHz, the radiation frequency is very close to the plasma resonance frequency. We saw very rich nonlinear dynamic effects exhibited in the dc I-V characteristics, such as, negative resistance regions, subharmonic steps, and noisy I-V curves which cannot

DD FORM 1 JAN 73 1473 EDITION OF 1 NOV 65 IS OBSOLETE
S/N 0102-014-6601

unclassified
SECURITY CLASSIFICATION OF THIS PAGE (When Data Entered)

be explained by thermal or other noise sources.

By using a RCSJ (Resistively and Capacitively Shunted Junction) model, modified to include a piecewise nonlinear resistance, with an appropriate amour of noise, we can reproduce the dc I-V curves of the irradiated junctions very accurately in both digital and analog simulations. The agreement between the simulations and the experimental results is excellent in those qualitative features on dc I-V curves such as the appearance of certain subharmonic steps a negative resistance regions. The agreement is very good in some of the quanti- tative comparisons such as the step width dependence on the laser power.

The simulations showed that the response of the junctions to the laser radiation is extremely sensitive to the plasma frequency f_p when the laser frequency $f_L \approx f_p$. Changing f_L/f_p by 10%, say, from $f_L/f_p = 0.97$ to 1.07, the I-V curves of different irradiated junctions showed quite unmistakable differer The one with $f_L/f_p = 1.07$ showed the 2/3 subharmonic Josephson step and the oth one with $f_L/f_p = 0.97$ showed the 1/2 subharmonic Josephson step with a little bump at the edge. These very distinctive features on dc I-V curves can serve a "fingerprints" for each junction. Since the parameter range of f_p to see those fingerprints is very narrow, by scanning f_p to reproduce the experimental I-V curves in simulations, we can quite accurately determine the experimental f_p value, which is the most important parameter in the nonlinear dynamics of Josephson junctions.

Aided by simulations, we discovered that the noisy I-V curves are caused b various nonlinear dynamic effects. There are I-V curves irradiated at certain laser power levels which show intrinsic chaos, i.e. the system motion is random even in the absence of noise. The simulations showed that the chaotic state ha been reached through either period-doubling bifurcation or intermittency or quasiperiodicity depending on the particular bias conditions on the I-V curve. On the other hand, there are quite a few noisy regions in the experimental I-V curves that do not show intrinsic chaos in the noise-free simulations, but instead show the coexistence of two or more attractors. Adding noise comparabl to that of the experiment makes the system switch randomly between the attracto thus producing noisy I-V curves which are indistinguishable from those of intri ically chaotic regime.

In one of those noise-induced chaos regions, we found in digital simulati that the boundary which separates the two coexisting basins of attraction is a fractal, with dimension bigger than one. At certain dc bias current, the dimension can be quite close to two, which would mean that the whole phase pla is occupied by basin boundaries. In these circumstances, any uncertainty in t initial conditions will cause tremendous uncertainty in the later motion of th system. In this case, the system will be extremely sensitive to noise. From digital calculation of dimension of the fractal basin boundary, we found that peak postion of the boundary dimension vs. dc current coincides with the peak position of noise density vs. dc current in the experiment. This agreement is strong evidence that the noise sensitivity is indeed related to the dimension of the basin boundaries.

Office of Naval Research

Contract N00014-83-K-0383 NR-319-116
Contract N00014-84-K-0465 NR-372-012

NOISE AND CHAOS IN DRIVEN JOSEPHSON JUNCTIONS

By

Qing Hu

March 1987

Technical Report No. 25

Division of Applied Sciences
Harvard University, Cambridge, Massachusetts

Office of Naval Research

Contract N00014-83-K-0383 NR-319-116
Contract N00014-84-K-0465 NR-372-012

NOISE AND CHAOS IN DRIVEN JOSEPHSON JUNCTIONS

By

Qing Hu

Technical Report No. 25

March 1987

The research reported in this document was made possible through support extended the Division of Applied Sciences, Harvard University, by the Office of Naval Research, under Contract N00014--83-K-0383 and Contract N00014-75-C-0648.

Division of Applied Sciences

Harvard University · Cambridge, Massachusetts

ABSTRACT

We have studied in detail the response of several Nb-aSi-Nb junctions to laser radiation at far-infrared frequencies, 245, 419, and 604 GHz. All these Nb-aSi-Nb junctions were made by the SNAP (Selective Niobium Anodization Process) procedure on a single wafer. They all have the plasma frequency $f_p=(2eI_c/\hbar C)^{1/2}/2\pi$ about 400 GHz. When we irradiate the junctions at 419 GHz, the radiation frequency is very close to the plasma resonance frequency. We saw very rich nonlinear dynamic effects exhibited in the dc I-V characteristics, such as, negative resistance regions, subharmonic steps, and noisy I-V curves which can not be explained by thermal or other noise sources.

By using a RCSJ (Resistively and Capacitively Shunted Junction) model, modified to include a piecewise nonlinear resistance, with an appropriate amount of noise, we can reproduce the dc I-V curves of the irradiated junctions very accurately in both digital and analog simulations. The agreement between the simulations and the experimental results is excellent in those qualitative features on dc I-V curves such as the appearance of certain subharmonic steps and negative resistance regions. The agreement is very good in some of the quantitative comparisons such as the step width dependence on the laser power.

The simulations showed that the reponse of the junctions to the laser radiation is extremely sensitive to the plasma resonance frequency f_p when the laser frequency $f_L \approx f_p$. Changing f_L/f_p by 10%, say, from $f_L/f_p = 0.97$ to 1.07, the I-V curves of different irradiated junctions showed quite unmistakable differences. The one with $f_L/f_p = 1.07$ showed the 2/3 subharmonic Josephson step and the other one with $f_L/f_p = 0.97$ showed the 1/2 subharmonic Josephson step with a little bump at the edge. These very distinctive features on dc I-V curves can serve as "fingerprints" for each junction. Since the parameter range of f_p to see those fingerprints is very narrow, by scanning f_p to reproduce the

experimental I-V curves in simulations, we can quite accurately determine the experimental f_p value, which is the most important parameter in the nonlinear dynamics studies of Josephson junctions.

Aided by simulations, we discovered that the noisy I-V curves are caused by various nonlinear dynamic effects. There are I-V curves irradiated at certain laser power levels which show intrinsic chaos, i.e. the system motion is random even in the absence of noise. The simulations showed that the chaotic state has been reached through either period-doubling bifurcation or intermittency or quasiperiodicity depending on the particular bias conditions on the I-V curve. On the other hand, there are quite a few noisy regions in the experimental I-V curves that do not show intrinsic chaos in the noise-free simulations, but instead show the coexistence of two or more attractors. Adding noise comparable to that of the experiment makes the system switch randomly between the attractors, thus producing noisy I-V curves whioh are indistinguishable from those of intrinsically chaotic regime.

In one of those noise-induced chaos regions, we found in digital simulations that the boundary which separates the two coexisting basins of attraction is a fractal, with dimension bigger than one. At certain dc bias current, the dimension can be quite close to two, which would mean that the whole phase plane is occupied by basin boundaries. In these circumstances, any uncertainty in the initial conditions will cause tremendous uncertainty in the later motion of the system. In this case, the system will be extremely sensitive to noise. From the digital calculation of dimension of the fractal basin boundary, we found that the peak position of the boundary dimension vs. dc current coincides with the peak position of noise density vs. dc current in the experiment. This agreement is a strong evidence that the noise sensitivity is indeed related to the dimension of the basin boundaries.

TABLE OF CONTENTS

		page
ABSTRACT		i
TABLE OF CONTENTS		iii
LIST OF FIGURES		vi
LIST OF TABLES		xi
CHAPTER I:	INTRODUCTION	1
CHAPTER II:	THEORY	7
2.1	Introduction	7
2.2	The RCSJ model	8
2.3	Chaos in a Josephson junction	15
2.3.1	Routes to chaos	15
2.3.2	Chaotic regions in a Josephson junction	20
2.4	Effect of noise on a Josephson junction	32
2.4.1	Noise effect on an autonomous Josephson junction	33
2.4.2	Noise effect on a nonautonomous Josephson junction	43
CHAPTER III:	EXPERIMENTAL TECHNIQUES	46
3.1	Introduction	46
3.2	Sample preparation	46
3.3	Laser and coupling antenna	53
3.3.1	The laser source	53
3.3.2	Coupling antenna	53
3.4	Noise reduction	60
3.4.1	Introduction	60

	3.4.2 Techniques of noise reduction	63
CHAPTER IV:	ANALOG SIMULATIONS	81
4.1	Introduction	81
4.2	Analog circuit of Magerlein design simulator	83
	4.2.1 The principle of operation	83
	4.2.2 Converting experimental values into simulation ones	92
4.3	Performance of the simulator	96
	4.3.1 Performance in the linear region	96
	4.3.2 Performance in the nonlinear region	98
4.4	Study of noise effects with the simulator	101
CHAPTER V:	DATA ANALYSIS	109
5.1	Introduction	109
5.2	Survey of experimental results	110
5.3	Analysis of I-V characteristics by comparison with simulations	119
	5.3.1 The importance of added noise	119
	5.3.2 Determination of ω_p	123
	5.3.3 Calibration of i_{ac}	126
	5.3.4 Experiments at 604 GHz and 245 GHz	132
5.4	Effect of noise in a fractal basin boundary regime	135
5.5	Power spectrum of noise-induced intermittency	145
5.6	Concluding remarks	154
CHAPTER VI:	CONCLUSIONS	156
6.1	Summary and conclusions	156
6.2	Future work	159
REFERENCES		162

ACKNOWLEDGEMENTS 168

LIST OF FIGUERS

		page
Fig. 2.1	Circuit of the RCSJ model.	9
Fig. 2.2	Schematic I-V curve of an ac and dc voltage-biased Josephson junction.	11
Fig. 2.3	Schematic I-V curve of an ac voltage-biased, but dc current-biased Josephson.	12
Fig. 2.4	The inverse square of the average periods N of the periodic state vs. the ac current amplitude measured from the critical point I_{ac}^{c} in an analog simulation.	19
Fig. 2.5	(a) State diagram in the i_{ac} - f_L/f_p plane, β_c=25, i_{dc}=0. (b) State diagram in the i_{ac}-f_L/f_p plane. β_c=16, i_{dc}=0.	22
Fig. 2.6	(a) Threshold curves for transition to chaos in the i_{ac}-f_L/f_p plane. (b) State diagram in the i_{ac}-β_c plane with f_L/f_p=0.65.	24
Fig. 2.7	(a) The initial phases of the m=1 (period-one) and m=2 (period-two) solutions on the n=1 step. (b) Maximum Liapunov exponent for the stable m=1 and m=2 solutions. (c) Generalized plasma frequency for the stable m=1 and m=2 solutions.	28
Fig. 2.8	Theoretical threshold of transition to chaos in the i_{ac}-f_L/f_p plane.	31
Fig. 2.9	Schematic of the tilted washboard potential.	35
Fig. 2.10	Current-voltage characteristics of Josephson junction at different noise levels in the β_c=0 limit.	37
Fig. 2.11	(a) Schematic of the probability of the noise-induced premature switching vs. the dc bias current. (b) Schematic of the width of the switching distribution vs. temperature.	40

		page
Fig. 3.1	Cross sectional view of a SNAP junction.	48
Fig. 3.2	SEM photographs of a SNAP junction.	50
Fig. 3.3	Dc I-V curve of the SNAP1 junction.	52
Fig. 3.4	Optically-pumped far-infrared laser set-up.	54
Fig. 3.5	Equivalent circuit of a dipole antenna.	55
Fig. 3.6	(a) Effective length h_e of receiving antenna normalized to the wavelength λ_0 as a function of $\pi L/\lambda_0$. (b) Measured impedance of receiving antenna as function of $L/2\lambda_0$.	57
Fig. 3.7	Calculated results of the square of the effective length over the antenna impedance vs. $\pi L/\lambda$.	59
Fig. 3.8	Reduction factor α of resonant frequency vs. the relative dielectric constant of the substrate.	59
Fig. 3.9	Probabilities of switching distribution measured from a Sn-SnO_x-Sn junction in the temperature range of 1.37K-2.83K.	62
Fig. 3.10	Illustration of noise coupling into an experimental system.	64
Fig. 3.11	Illustration of transmitted electric and magnetic fields through a plane sheet.	65
Fig. 3.12	Shielding effectiveness of a 0.02-in. thick copper shield in the far field.	71
Fig. 3.13	Results of inductive coupling experiment; all circuits are grounded at both ends.	74
Fig. 3.14	Results of inductive coupling experiment; all circuits are grounded at only one end.	74
Fig. 3.15	Experimental set-up.	76

		page
Fig. 3.16	Power spectra measured from a 1kΩ resistor connected at the position of the "sample" in Fig. 3.15. (a) From the present set-up (Fig. 3.15); (b) from the previous set-up, in which no special care was taken to minimize noise pick-up.	78
Fig. 3.17	1/f power spectrum measured from a SNAP junction at room temperature.	80
Fig. 4.1	Illustration of the principle of function of Magerlein's analog simulator.	85
Fig. 4.2	Block diagram of Magerlein's analog simulator.	86
Fig. 4.3	Circuit diagram of sinϕ generator.	88
Fig. 4.4	(a) Analog circuit of the RCSJ model; (b) circuit of the piecewise nonlinear resistor.	91
Fig. 4.5	(a) Voltage response of the simulator as function of the drive frequency of an ac current with a small amplitude. (b) Resonant frequency vs. the dc bias current.	97
Fig. 4.6	Simulated I-V curves with different damping.	99
Fig. 4.7	Simulated threshold of transition to chaos in the i_{ac}-f_L/f_p plane by using both linear and nonlinear resistance.	100
Fig. 4.8	Simulated I-V curves taken at different noise levels with β_c=4 (using R_n), and β_c=36 (using R_{leak}).	102
Fig. 4.9	Measured critical current from the simulated I-V curves vs. γ with different damping.	104
Fig. 4.10	Measured critical current from the simulated I-V curves vs. β_c at different noise levels.	106

		page
Fig. 4.11	Measured critical current from nonhysteretic I-V curves vs. $\log(\gamma/\beta_c^{3/2})$.	107
Fig. 5.1	Chaotic I-V curves of the SNAP1 junction irradiated with 419 GHz radiation.	112
Fig. 5.2	I-V curve of the SNAP1 junction taken at i_{ac}=2.0.	114
Fig. 5.3	(a) I-V curves of the SNAP2 junction irradiated with 419 GHz radiation. (b) Simulated I-V curve with f_L/f_p=0.97 and i_{ac}=1.0. (c) The same as (b) except adding a 20K white Gaussian noise.	118
Fig. 5.4	Threshold of current amplitude of perturbation required to remove the hysteresis of I-V curve in Fig. 5.3(b) as a function of frequency.	123
Fig. 5.5	Approximate state diagram of appearance of certain featrues of I-V curves in i_{ac}- ω_L/ω_p plane.	125
Fig. 5.6	Experimental I-V curves of the SNAP2 junction irradiated at 419 GHz. The critical current of the junction is magnetically suppressed.	127
Fig. 5.7	(a) Experimental I-V curve of the SNAP2 junction with a laser power 13.9 times higher than that of one with i_{ac}=1.0 in Fig. 5.3(a). (b) Simulated I-V curve with ω_L/ω_p=0.97 and i_{ac}=3.73. (c) Same as (b) except adding 40K white Gaussian noise.	129
Fig. 5.8	The zeroth Josephson step width vs. i_{ac}. The junction is irradiated at 419 GHz.	131
Fig. 5.9	Step width vs. i_{ac}. The junction is irradiated at 604 GHz.	133
Fig. 5.10	Phase orbits and Poincaré sections from noiseless analog simulation with i_{ac}=1.5 and f_L/f_p=1.07 at different dc bias.	136

		page
Fig. 5.11	Basins of attraction for i_{ac}=1.0 and i_{dc}=0.15.	138
Fig. 5.12	Illustration of basin boundary of attraction.	139
Fig. 5.13	The measured noise density and the calculated dimension of basin boundary vs. dc bias current. (a) Simulated and (b) experimental I-V curves. (c) Dependence of the critical current on the laser drive. (d) Computed basin boundary dimension and (e) experimental noise power measurements at 10 kHz as a function of dc bias.	142
Fig. 5.14	Effect of added noise on the Poincaré sections for the system: (a), (b) in fractal basin boundary regime at i_{dc}=0.18 and i_{ac}=1.0, and (c), (d) in an "intrinsic" chaotic regime at i_{dc}=0.15 and i_{ac}=1.5.	144
Fig. 5.15	Effect of added noise on the power spectra calculated from the digital simulations with i_{dc}=0.18 and i_{ac}=1.0.	146
Fig. 5.16	Measured Lorentzian power spectrum from the analog simulation with i_{dc}=0.17, i_{ac}=1.0, f_L/f_p=1.07 and T=50K.	147
Fig. 5.17	Normalized mean-square fluctuation deduced from the measured quantities S(0) and f_{3dB} vs. the noise level.	151
Fig. 5.18	Logarithmic plot of lifetimes deduced from the measured S(0) and f_{3dB} through (5.14) as functions of the noise temperature.	153

LIST OF TABLES

		page
Table 2.1	Location and spacing of dc bias of the bifurcation points for the period-doubling cascade.	17
Table 3.1	Skin depth of various materials.	67
Table 3.2	Impedance value of various metals.	69
Table 4.1	Converting relations between the experimental parameters and the simulational ones.	95

CHAPTER I

INTRODUCTION

Ever since Brian Josephson suggested in 1962 that two weakly-coupled superconductors might show some very distinctive nonlinear effects now named after him,[1] Josephson junction systems have been a research subject interesting to a broad range of scientists, from those who are interested in the universal nature of nonlinear dyamics and the fundamentals of quantum mechanics, to application-oriented scientists who are trying to build the fastest, most sensitive and precise instruments by using Josephson devices.

The major attraction of the Josephson system is its simplicity and richness of nonlinear dynamics and quantum mechanical effects. Although the complete theory of Josephson tunneling is based on a very complicated microscopic many-body theory,[2] for most purposes a Josephson junction can be very well characterized by the so-called RCSJ model (Resistively and Capacitively Shunted Junction). Its equation of motion turns out exactly the same as a damped driven pendulum, except its characteristic frequency is about 10^9-10^{12} times higher than that of a typical mechanical pendulum, which makes the Josephson junction a useful device for high frequency purposes. Also, its characteristic energy is typically in the order of thermal noise at several degrees temperature. This feature makes the Josephson device sensitive to some very weak signals that are comparable to thermal noise level, which is by far the most sensitive device at high frequency up to far-infrared region ($\sim 10^{12}$ Hz).

However simple the Josephson system is, it is a nonlinear system; thus it shares some universal behaviors with a large variety of other nonlinear systems.

Feigenbaum[3] first studied a pattern by which a nonlinear system might go into

chaos: As one of the system parameters is changed towards a chaotic region from nonchaotic ones, the system shows a sequence of appearances of subharmonic frequencies 1/2, 1/4, 1/8, ... of the original driving frequency. Eventually the $1/2^{\infty} = 0$ frequency comes out, and the motion of the system is no longer periodic even though it is a deterministic system driven at a single frequency.

Manneville and Pomeau[4] have studied another route to chaos through intermittency: As one of the system parameters exceeds a critical value, the otherwise periodic motion becomes interupted by occasional random bursts. The bursts happen more and more often as the parameter approaches the chaotic region, and eventually the random bursts happen so often that the periodic feature of the motion is totally washed out.

Besides these two most well known routes to chaos, other routes and the associated universal features have been studied also. One of those is the transition from quasiperiodic motion to a chaotic one in a system driven by two or more incommensurate frequencies.[5]

It was Huberman, Crutchfield and Packard[6] who first applied those theories for general nonlinear systems to Josephson junction system. They computed a chaotic-periodic state diagram in the i_{ac}-ω_{drive} plane. Since then, the study of chaos in Josephson systems has been one of the most active fields in physics. Many simulations have been made, very detailed and complicated state diagrams have been computed,[7-11] some of the universal constants and universal laws predicted for general nonlinear systems have been checked.[12-14] However, in spite of the rich publications in the quantitative simulation studies of universal chaotic behaviors in Josephson junctions, the experimental studies on a real Josephson junction have remained somewhat qualitative and descriptive.[15-20] The main reason is that the characteristic fequency of a Josephson junction is so high (at least 10 GHz) that the direct observation of many predicted features of chaos, such as period doubling bifurcation to chaos, is impossible. All people can see in an experiment on a real

Josephson junction is some time averaged quantities such as dc I-V curves and low frequency power spectrum. All the clues about chaos they can find in an experiment are some unusual I-V characteristics such as negative resistance or noisy Josephson steps and the associated exceptionally high level of low-frequency noise power density. To model the junction correctly and find the right parameters for the junction to reproduce the I-V characteristics in a much slower simulation is a very crucial step to bridge the gap between the general knowledge we have about chaos and the data taken from a real Josephson junction.

This report is focused on the experimental and the associated simulational work done on several Nb-aSi-Nb junctions made by the SNAP (Selective Niobium Anodization Process) procedure. These junctions have critical current densities of about 9000A/cm^2. Together with the dielectric properties of the amorphous Si barrier, this gives the plasma resonance frequency of the junction $f_p = (2eI_c/\hbar C)^{1/2}/2\pi$ about 400 GHz. The junctions are located at the center of a half wave dipole antenna which is broadly resonant about 400 GHz. We have studied the responses of these junctions to laser radiation at three frequencies, 245, 419 and 604 GHz. At 604 GHz, which is 1.5 times the plasma frequency, we did not see any unusual behavior such as a noisy step or a negative resistance region, except the ac Josephson step width is somewhat smaller than expected. This absence of chaos is consistent with the digitally calculated state diagrams, which show that the chaos threshold of ac drive amplitude diverges quite quickly when the driving frequency is increased above the plasma frequency. At 419 GHz and 245 GHz, 1 and 0.6 times the plasma frequency respectively, the state diagram suggests we should be able to see chaotic phenomena at a modest driving amplitude even at zero dc current. And indeed, we saw some quite distinctive features on the dc I-V curves: Noisy and meandering steps; negative resistance regions; subharmonic steps in the absence of an adjacent integer step; and extremely high levels of low frequency noise. None of these

features above will be seen in a well-behaved Josephson junction, for example, a voltage-biased Josephson junction, which is very well characterized by the Bessel function dependence of the step width on driving amplitude. Also, all those features can not be explained solely by thermal or other kinds of random noise in the system, or by the fluctuations in the laser power. There must be something intrinsic behind those unusual behaviors.

We did extensive digital and analog simulations to find out what happened in the real junctions. Both digital and analog simulations are based on a RCSJ (Resistively and Capacitively Shunted Junction) model modified to include a piece-wise nonlinear resistance approximating the nonlinear quasiparticle I-V structure at the gap. First, we need to know all the parameters to reproduce the experimental result in the simulations, especially the plasma resonance frequency f_p. The simulation results showed that the specific features on I-V curves are extremely sensitive to f_p when f_p is close to the drive frequency. But due to the uncertainty in the area of the junction and the parasitic capacitance, we can not determine the plasma frequency of the junction to within less than 20% by using the specific capacitance value times the apparent area. The simulations reveal that some qualitative features on dc I-V curves, such as the appearance of certain subharmonic steps, appear only for a very narrow range of plasma frequency, when the driving frequency is near it. For example, in changing the ratio f_L / f_p by 10% from $f_L / f_p = 0.97$ to 1.07, the I-V curve with $f_L / f_p = 1.07$ shows the 2/3 Josephson subharmonic step, which is the characteristic feature of one of the SNAP junctions, but the one with $f_L / f_p = 0.97$ shows the 1/2 step, which is the feature of another junction. Since the 1/2 and 2/3 steps appear for such a narrow f_p range (10%), these specific features of the I-V curve can serve as a "fingerprint" of each junction to tell which parameter range it belongs to. By trying to reproduce those fingerprints in simulations, we can thus determine the parameter f_L / f_p unambiguously to a few per cent.

Although chaos is an intrinsic phenomena for a deterministic nonlinear system in the sense that, even in the absense of any random perturbation, the motion of the system can be very randomlike, in a real physical system we can never establish a noise free environment like most of the simulation studies have assumed. There is always thermal noise at finite temperature and shot noise at finite voltage plus other less intrinsic noise. The interplay of these noise sources and a highly nonlinear system is something that we must deal with. Including noise appropriately in the simulations by taking into account the difference in the averaging cycles between the experiment (10^{12} cycles) and the simulations (10^4 cycles), we could reproduce the experimental I-V curves in the simulations in a very impressive way both in the qualitative features of I-V curves, such as the appearance of certain subharmonic steps, and the quantitative features, such as the dependence of the step width on the laser power.

The simulation also revealed that the similarly noisy I-V curves can be caused by quite different reasons. For some noisy I-V curves, the noise free simulations showed that the phase motion of the system is intrinsically chaotic; adding some noise comparable or bigger than in the experimental case does not change the motion qualitatively. On the other hand, the noise free simulations for some other noisy I-V curves do not show chaotic motion; instead the system has more than one stable periodic solution, but which periodic motion the system will converge to depends very sensitively on the initial conditions. When we computed the basins of attraction (i.e. the region in the phase space from which the system will evolve into a specific attractor), the pattern is extremely complicated. The boundary between the basins is usually fractal, and the dimension of such boundary can be quite close to 2. This would mean that the whole phase space is occupied by basin boundary, so that any uncertainty in the initial conditions, no matter how small, can cause the system to evolve to a different attractor. Apparently, this high dimension of the basin boundary corresponds to a high sensitivity of the system to noise. This hypothesis has

been supported by the fact that the peak of the dimension of the fractal basin boundary coincides with the peak of the noise density measured in the experiment vs. dc bias current.

This report is organized into six chapters. Following this brief introductory chapter, Chapter II will lay out the theoretical framework for the analysis of later chapters. Chapter III is devoted to the experimental aspect of this research work, including sample preparation, laser set up and coupling antennas, and low noise measurement. Chapter IV will describe in detail the analog simulator we have been using, its principle of operation and performance. In Chapter V, we will discuss the analysis of the experimental data and comparison with the simulation results. The major conclusions will be summarized in Chapter VI, as will proposals of future investigation in this field.

CHAPTER II

THEORY

2.1 Introduction

Although the complete theory about Josephson tunneling is based on a very complicated microscopic theory derived by Werthamer[2] in 1966, for a lot of purposes, a Josephson junction is very well characterized by the so called RCSJ (Resistively and Capacitively Shunted Junction) model. This model has a very clear physical picture: the electrical conduction of a Josephson junction takes place through three separate channels:

1. The Josephson phase-dependent current channel which is due to dissipationless Cooper pair tunneling;
2. The quasiparticle tunneling channel which always exists at finite temperature;
3. The capacitive channel which is inevitable due to the sandwich geometry of Josephson junctions.

The equation of motion of the RSCJ model is a second order nonlinear differential equation which is considerably easier to handle than Werthamer's microscopic theory, although the RCSJ equation is itself not solvable analytically. Also, the RCSJ equation is exactly the same in mathematical form as that of a damped driven pendulum. This mechanical analogy is extremely helpful in understanding the motion of a Josephson system. It makes insightful physical intuition instead of complicated mathematical computation play the important role.

Just like most of the physicists working in superconductivity today prefer to use Ginzburg-Landau theory, which is a phenomenological mean-field version of BCS theory valid in a special case ($T \sim T_c$), the author prefers to stay with the RCSJ model wherever it is applicable. Thus this theory chapter will be mostly devoted to the RCSJ model. But we

have to keep in mind the limits of the model, such as heating and the high frequency limit. Heating effects occur in a junction when the Ohmic heat produced by quasiparticle current raises the local temperature above the ambient temperature, thus depressing the superconductivity of the junction.[21] This can cause serious deviations from the RCSJ model, in which the critical current I_c is assumed to be a constant independent of bias condition. But due to the high resistance nature of a tunnel junction, the heating effect is much less significant than in a metallic microbridge. At high frequencies, when the frequency concerned is above the gap, pair breaking starts happening, the critical current is no longer a constant, and we should expect a large deviation between the behaviors of a real Josephson junction and the RCSJ model[2]. For a tunnel junction made of Nb, the gap frequency is above 1THz, so below that frequency, we can safely apply the RCSJ model. Besides these classical limitations on the RCSJ model, when the characteristic energy $h\omega_p$ associated with the plasma oscillation exceeds the thermal energy k_BT, we have to treat the mechanical particle governed by the RCSJ equation in a quantum mechanical way, that is, replace the Newtonian equation by the Schrodinger equation. A quantum mechanical effect called "macroscopic quantum tunneling" will dominate the thermally activated escape of the mechanical particle. This effect arises from the statistical nature of quantum mechanics and has no analogies to a classical mechanical particle[22-25]. Fortunately or unfortunately, for the samples studied in this report, none of the above effects is so dominant that a serious deviation from the RCSJ model occurs.

2.2 The RCSJ model

The model of a Josephson junction is illustrated in Fig. 2.1:

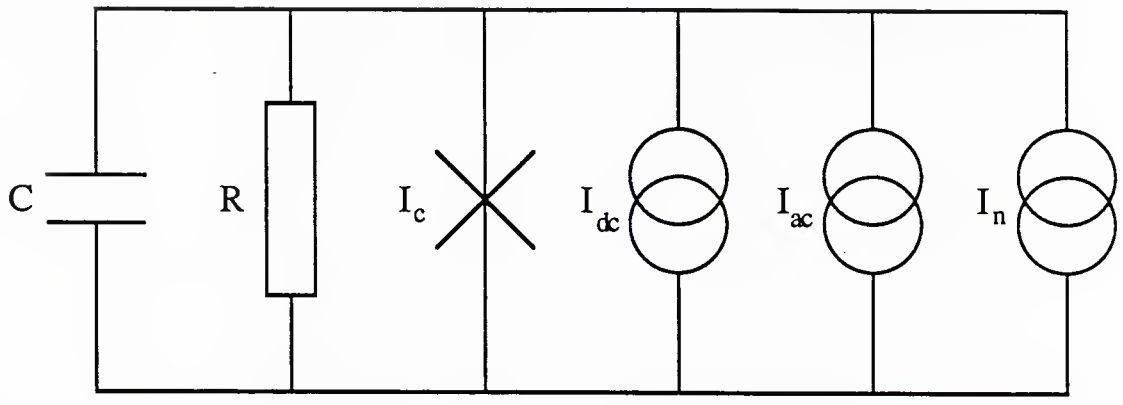

Fig. 2.1

Circuit of the RCSJ model.

If we write down the current-voltage relation of this model, apparently we will get

$$C\frac{dV}{dt} + I_{qp}(V) + I_c \sin\phi = I_{dc} + I_{ac}(t) + I_n(t) \qquad (2.1)$$

If we introduce the Josephson phase-voltage relation

$$\frac{d\phi}{dt} = \frac{2eV}{\hbar} \qquad (2.2)$$

we should be able in principle to solve the voltage for given current or vice versa. The voltage dependence of the quasiparticle current is usually a nonlinear form, but for the time being, we will neglect the nonlinearity in $I_{qp}(V)$, and assume $I_{qp}=V/R$. That will not affect our discussion qualitatively as long as we are not considering photon-assisted-tunneling (PAT).[26,2] Also we will leave out the noise term $I_n(t)$ until section 2.4.

We are going to discuss separately the different ways a Josephson junction can be biased experimentally.

i) <u>Junction is both dc and ac voltage biased.</u>

In this case we can write

$$V = V_{dc} + V_{ac}\cos(\omega_L t) \tag{2.3}$$

both V_{dc} and $V_{ac}(t)$ are externally controllable variables, and ω_L is the laser drive frequency. I_{dc} and $I_{ac}(t)$ are to be determined. Plug (2.3) into (2.2) and then into (2.1), and we get:

$$C\frac{dV}{dt} + \frac{V}{R} + I_c \sin[\omega_o t + 2\alpha \sin(\omega_L t) + \phi_o] = I_{dc} + I_{ac}(t) \tag{2.4}$$

$$\omega_o = \frac{2eV_{dc}}{\hbar}, \quad \alpha = \frac{eV_{ac}}{\hbar}$$

In an experiment, we can only measure time-averaged quantities, so we take the time average of equation (2.4), and get:

$$I_{dc} = \frac{V_{dc}}{R} + I_c \sum_{n=-\infty}^{\infty} (-1)^n J_n(2\alpha) \sin(\phi_o)\, \delta_{\omega_0,\, n\omega_L} \tag{2.5}$$

Equation (2.5) implies that the irradiated I-V curves will have a set of infinitesimal thin spikes superposed on an otherwise linear curve as shown in Fig. 2.2, the positions of those spikes are at $V_n = n(\hbar\omega_L/2e)$ (n=0, ±1, ±2, ...), and the height of each spike is given by

$$\Delta I_n = 2J_n(2\alpha)\, I_c \tag{2.6}$$

(since $\sin\phi_O$ can be varied from -1 to +1).

It is impossible to see something infinitesimal in experiments. Besides, the impedance of a Josephson junction is usually quite low, compared to the source and dc leads impedance, especially at the steps, where the dynamic resistance is zero; so the dc voltage-bias is not a quite realistic case.

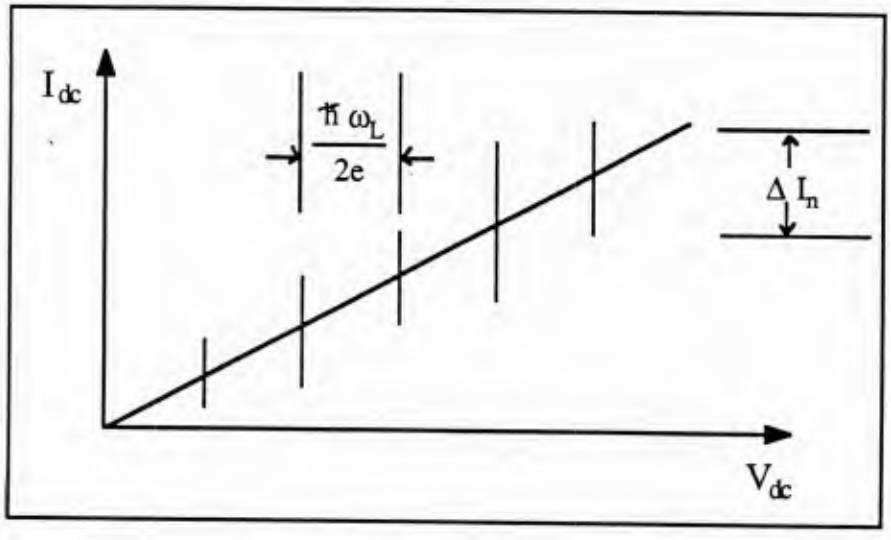

Fig. 2.2

Scheamtic I-V curve of an ac and dc voltage-biased Josephson junction.

ii) Junction is dc current biased but ac voltage biased.

This means that I_{dc} and V_{ac} are externally controllable parameters; V_{dc} and $I_{ac}(t)$ remain to be found. Write

$$I = I_{dc} + I_{ac}(t)$$

$$V = V_{dc} + V_{ac}\cos(\omega_L t)$$

plug the second equation into equation (2.2), and we get, as before,

$$\phi(t) = \omega_o t + 2\alpha \sin(\omega_L t) + \phi_O$$

Putting this into equation (2.1), we have

$$C\frac{d(V_{ac}\cos\omega_L t)}{dt} + \frac{V_{dc} + V_{ac}\cos\omega_L t}{R} + I_c \sin[\omega_o t + 2\alpha \sin(\omega_L t) + \phi_o] = I_{dc} + I_{ac}(t) \qquad (2.7)$$

This equation is the same in form as the equation (2.4) except now it is I_{dc} instead of V_{dc} that is the controllable variable. Taking the time average of equation (2.7), we have

$$V_{dc} = R\left[I_{dc} - I_c \sum_{n=-\infty}^{\infty} (-1)^n J_n(2\alpha) \sin(\phi_o)\, \delta_{\omega_o, n\omega_L} \right] \qquad (2.8)$$

From the phase-locking argument given later in this section, in the region

$$V_{dc} = n\frac{\hbar\omega_L}{2e} \qquad n = 0, \pm1, \pm2, \ldots$$

$$\frac{V_{dc}}{R} - I_c J_n(2\alpha) < I_{dc} < \frac{V_{dc}}{R} + I_c J_n(2\alpha)$$

the initial phase ϕ_o will vary in such a way to keep V_{dc} constant, forming a zero dynamic resistance step; outside these regions the V_{dc}- I_{dc} curve will approach the original ohmic line as the operating point considered moves away from the step region. Thus the V_{dc}- I_{dc} curve in this case will look like the one in Fig. 2.3. The step width of the nth step is given by

$$\Delta I_n = 2\, I_c\, J_n(2\alpha) \qquad (2.9)$$

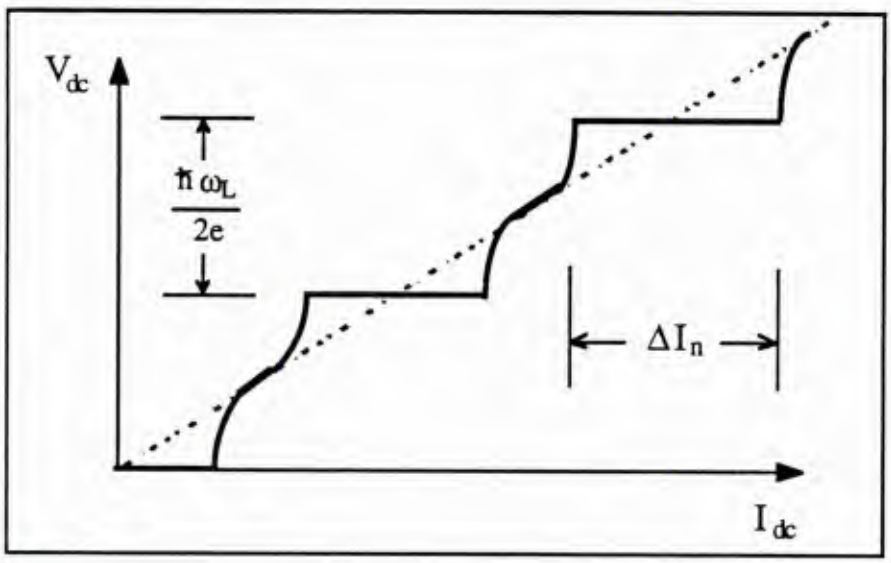

Fig. 2.3

Schematic I-V curve of an ac voltage-biased, but dc current-biased Josephson junction.

This well-known result has been verified in many junctions at different frequencies[27-29]. One thing to point out is that in both cases i) and ii), as long as the time dependent voltage has only a single frequency component, i. e.

$$V_{ac}(t) = V_{ac} \cos(\omega_L t)$$

then we can only get integer Josephson steps, regardless of whether we can control the dc voltage or not.

iii) Junction is both dc and ac current biased.

In this case, the controllable variables are:

$$I = I_{dc} + I_{ac} \cos \omega_L t$$

and we must solve to find:

$$V = V_{dc} + V_{ac}(t)$$

Even though this case is only one step further, it is a qualitative change. Because now we do not know the time evolution form of $\phi(t)$ a priori, we can not use the method of cases i) and ii). We have to deal with a second-order nonlinear differential equation; it is not analytically solvable in general. However, in three special cases, the case iii) will reduce to case ii):

$$\begin{aligned} &1. \quad \omega_L L >> R \\ &2. \quad \omega_L L >> \frac{1}{\omega_L C} \\ &3. \quad I_{ac} >> I_c \end{aligned} \tag{2.10}$$

(Here $L = \hbar/2eI_c$ is the minimum of the nonlinear Josephson inductance.) The first two conditions mean that the impedance of one of the linear elements (R or C) is much lower than that of the Josephson inductance, so that most of the ac current will flow through the linear element with the lowest impedance. Condition 3 means that the ac current amplitude is much bigger than the critical current, which is the maximum current the Josephson

element allows to flow, so that again most of the ac current has to flow through the other two linear channels. In any of these three cases, most of the ac current will flow through the linear element with the lowest impedance, and the nonlinear Josephson element is effectively ac voltage-biased by the voltage across this internal linear element, whatever the external source impedance may be.

If none of the conditions (2.10) is satisfied, we have to deal with a nonlinear equation. Combining equations (2.1) and (2.2), we get:

$$\frac{\hbar C}{2e}\frac{d^2\phi}{dt^2} + \frac{\hbar}{2eR}\frac{d\phi}{dt} + I_c \sin\phi = I_{dc} + I_{ac}\cos\omega_L t \qquad (2.11)$$

Introducing the dimensionless parameters:

$$\omega_p = \sqrt{\frac{2eI_c}{\hbar C}}$$

$$\beta_c = (\omega_p RC)^2$$

$$\tau = \omega_p t$$

$$i_{dc} = I_{dc}/I_c$$

$$i_{ac} = I_{ac}/I_c$$

we reduce equation (2.11) to a dimensionless equation:

$$\frac{d^2\phi}{d\tau^2} + \frac{1}{\beta_c^{1/2}}\frac{d\phi}{d\tau} + \sin\phi = i_{dc} + i_{ac}\cos\frac{\omega_L}{\omega_p}\tau \qquad (2.12)$$

Four parameters ω_L/ω_p, β_c, i_{dc} and i_{ac} totally determine the outcome of equation (2.12). This equation resembles the equation of motion of a driven damped pendulum, or, in a purely dc-biased case, a ball moving in a tilted "washboard" potential. Which mechanical analogy is more useful depends on the situation. When we deal with phase-locking problems, the driven pendulum is a more helpful picture, as it is easier to visualize a pendulum rotating commensurately with a driving torque. When we deal with switching phenomena, in which the junction switches from the zero voltage state to the

nonzero voltage state or the other way around, the tilted washboard potential is definitely a better picture.

With the help of the mechanical analogies, even without being able to solve equation (2.12) analytically, we can still predict qualitatively what might happen:

For a mechanical pendulum, if the rotation of the pendulum is commensurate with the driving frequency, i.e. if the pendulum rotates **m** turns for **n** cycles of driving force, this motion is apparently more stable against perturbations than incommensurate motion. This is the so-called phase-locking motion, a phenomena first observed by the Dutch physicist Huygens in the 17th century, when he noticed that two closely located pendulums tend to synchronize their oscillations. In terms of I-V characteristic, this means at certain voltage values ($V \propto d\phi/dt$)

$$V_{n,m} = n/m\ (\hbar\omega_L/2e) \qquad n = 0, 1, 2, \ldots \quad m = 1, 2, \ldots \qquad (2.13)$$

the voltage tends to stay at that value even though the current is changed away from $V_{n,m}/R$, thus forming a constant voltage step, resembling those described in case ii), but with the difference:

1) Now we have not only integer steps (m=1) but also subharmonic steps (m>1), which will never appear in cases i) and ii).

2) The width of each step is no longer an analytical function of the driving power. Experimentally, this means that it is much more difficult to deduce i_{ac} from the dc I-V curves of the irradiated junction.

2.3 Chaos in a Josephson junction

2.3.1 Routes to chaos

Most of the literature in the chaos field is addressed to the problem of how a nonlinear system goes into chaos near the chaotic-nonchaotic boundary. This phenomenon

is very much like the critical phenomena associated with a phase transition in other fields of condensed matter physics. By applying the powerful scaling theory to discrete return maps, people discovered some universal behaviors similar to critical exponents in critical phenomena for several routes to chaos. The following are the three most studied scenarios a nonlinear system might follow in going into chaos.

A. The Feigenbaum scenario: Period doubling bifurcation to chaos.

Feigenbaum[3] discovered a pattern by which a nonlinear system might go into chaos from the study of a quadratic return map

$$x_{n+1} = b\, x_n (1 - x_n)$$

and claimed the result holds for a large variety of nonlinear systems. Its implication to a driven nonlinear system can be specified as follows: In a certain parameter range of a nonlinear system, as one parameter *r* approaches the chaotic-nonchaotic boundary from the nonchaotic region, the period takes on the sequential values

$$T = 2^k T_{drive} \qquad k = 0, 1, 2 \ldots.$$

where T_{drive} is the period of the driving force. The ratio between successive intervals $\Delta r_{k-1}/\Delta r_k$ (where $\Delta r_k = r_k - r_{k-1}$) approaches a universal constant $\delta = 4.6692...$ as *k* goes to infinity, i.e.

$$\lim_{k \to \infty} \frac{\Delta r_{k-1}}{\Delta r_k} = \delta = 4.6692... \qquad (2.14)$$

This implies that the series of parameter ranges corresponding to successive periods forms a geometric series in the limit of large k; also the series is convergent so that the system will reach chaos at finite *r*.

Kautz[12] has checked the universality of (2.14) in a digital simulation of the RCSJ model. He chose i_{dc} as the varying parameter. Table 2.1 shows how good the agreement is between the simulation and the theoretical prediction.

Table 2.1

k	j_k	$\Delta j_k = j_k - j_{k-1}$	$\Delta j_{k-1} / \Delta j_k$
1	1.84834330	...	...
2	1.87077911	0.02243581	...
3	1.87584258	0.00506347	4.431
4	1.87697352	0.00113094	4.477
5	1.87721813	0.00024461	4.623
6	1.87727067	0.00005254	4.656
7	1.87728192	0.00001125	4.670

Table 2.1. Location and spacing of the bifurcation points for the period-doubling cascade at the lower end of the 10th step. j_k is the dc bias at which the period changes from 2^{k-1} to 2^k. (After Ref. 11)

B. The Pomeau-Manneville scenario: Transition to chaos through intermittency.

Pomeau and Manneville[4] discovered this route to chaos through study of the Lorenz equation system in fluid dynamics, which is

$$\frac{dx}{dt} = \sigma (y - z); \qquad \frac{dy}{dt} = -xz + rx - y; \qquad \frac{dz}{dt} = xy - bz,$$

where x, y, z are some time-dependent variables which describe the state of the Lorenz system, and σ, r, b are parameters of the system independent of time. They found out that as the parameter r surpasses the critical value r_c, the otherwise "laminar" phase is interrupted by random "turbulent" bursts. The duration of the "laminar" phase becomes shorter and shorter as r gets bigger. The average duration of "laminar" phase N near the critical point r_c diverges as r approaches r_c

$$N \propto (r - r_c)^{-1/2} \qquad (2.15)$$

This has been seen in an electronic Josephson junction simulator by Yeh and

Kao.[13] In their simulations, they chose the ac current amplitude i_{ac} as the varying parameter, and they measured the average periods N of the periodic state (corresponding to the laminar phase in the Lorenz system). Fig.2.4 shows the fit of the data to the N^{-2} vs. $(i_{ac} - i_{ac}^{c})$ line. Fluctuations in N are due to the random nature of the process including the intrinsic noise in the Josephson simulator and external noise in the current source.

C. The quasiperiodicity scenario: Transition from quasiperiodicity to chaos.

Several groups[5] have studied the 1-dimensional return map

$$\theta_{n+1} = \theta_n + \Omega - \frac{K}{2\pi} \sin 2\pi\theta_n$$

which is the discrete map isomorphic to the continous RCSJ equation. In this circle map, K characterizes the nonlinear coupling strength, while Ω is a bias term analogous to the dc bias current i_{dc} in the RCSJ equation. The winding number W is defined as:

$$W = \lim_{n\to\infty} \frac{\theta_{n+1} - \theta_1}{n}$$

which is the average phase velocity analogous to the dc voltage in the RCSJ model. There are three possible solutions for W:

(1) W=q/p, where both q and p are prime numbers. This corresponds to a phase-locked solution.

(2) W is an irrational number. This corresponds to a quasiperiodic solution.

(3) W is not a well-defined number. This corresponds to a chaotic solution.

At K<1, the W-Ω plot is a combination of phase-locked steps and quasiperiodic parts; there are no overlapped steps and chaotic solutions.

At K>1, there are overlapped steps in the W-Ω plot, and there are chaotic solutions for certain values of Ω.

At the critical point K=1, the W-Ω plot is composed purely of nonoverlapped

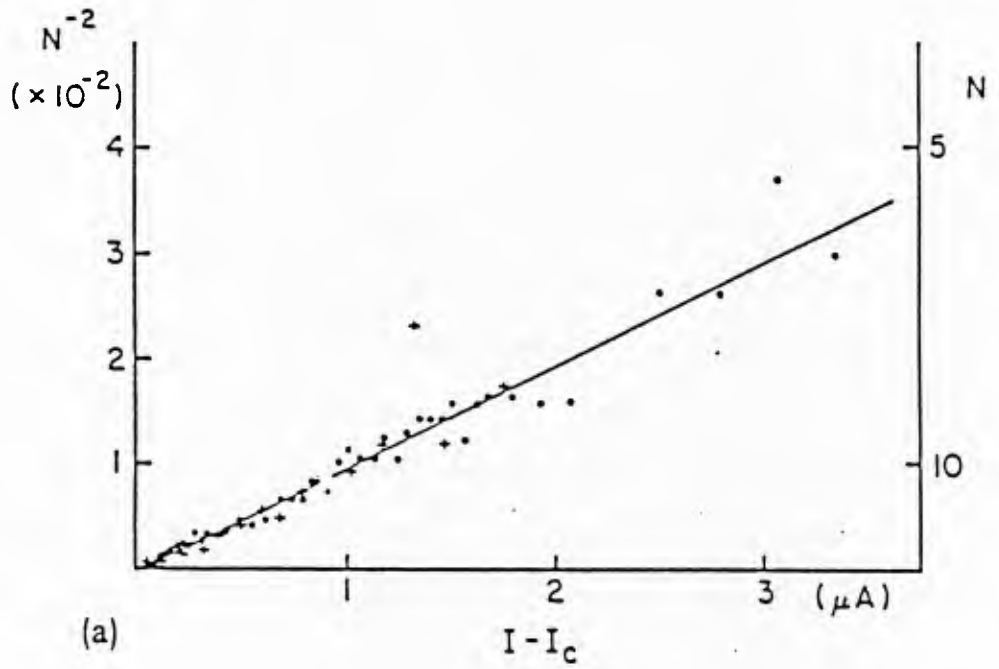

Fig. 2.4

The inverse square of the average periods N of the periodic state vs. the ac current amplitude measured from the critical point I_{ac}^{c} [(I - I_c) in the figure] in an analog simulation. (After Ref. 13)

phase-locked steps, forming a complete devil's staircase, with the dimension of the fractal structure D=0.87.

Two groups[13,14] have checked this prediction with an electronic Josephson simulator. They did find at certain critical values of certain parameters, the local V_{dc}- I_{dc} curve indeed showed a complete devil's staircase. i.e. part of the V_{dc}- I_{dc} curve is totally composed of non-overlapping subharmonic steps. Their measurements of D, 0.91±0.04 in ref. 13, and 0.87±0.02 in ref. 14, are in a quite good agreement with the prediction.

2.3.2 Chaotic regions in a Josephson junction.

Although all the scenarios described above are extremely important to study the universal behavior of how a Josephson junction and other nonlinaear dynamic systems go into chaos, practically, it is very difficult to observe all these phenomena in a real Josephson junction due to the high frequency nature of Josephson junctions. Besides, the unavoidable noise, thermal or nonthermal, will wash out all the fine structures, making it impossible to see a complete devil's staircase and to check those universality constants such as D. In an experiment on a real Josephson junction, we are more interested in finding out under what circumstances chaotic phenomena might appear.

It was Huberman, Crutchfield and Packard[6] who first studied chaos exhibited by an ac-driven Josephson junction, offering a possible explanation for the unusually high level of noise in a Josephson parametric amplifier. In that first paper, the authors also computed a chaotic-nonchaotic state diagram in the i_{ac} - f_L/f_p plane. Although the sketch is quite rough, so the chaotic-nonchaotic boundary appears to be a smooth curve, this was later found out to be incorrect, because the boundary has in general a fractal structure if we study the state diagram in a finer grid. Still, it provided guidance for further studies. Pedersen and Davidson[7] digitally integrated the RCSJ equation for the zero dc bias case. Their chaotic-nonchaotic state diagram is shown in Fig. 2.5a, in which the RCSJ equation

was numerically integrated with McCumber parameter $\beta_c = 25$. Clearly, the chaotic-nonchaotic boundary is much more complicated than just a simple smooth curve; also, the chaotic regions are separated by windows of periodic motion. The window index (p, q) indicates the p th subharmonic on the q th rf induced step. One interesting point in this state diagram is that the minimum drive amplitude i_{ac} for chaos takes place at $f_L/f_p \approx 0.67 \approx 2/3$ instead of at the plasma resonance frequency itself. The explanation lies in the fact that large drive amplitudes drive the Josephson junction into a nonlinear region, where the potential is softer than that of a harmonic oscillator, so the actual resonant frequency is lower than the plasma frequency, which is the natural oscillation frequency of the system when it is near the bottom of the potential well.

D'Humieres et al.[9] did an extensive study of the chaos-nonchaos state diagram on an analog simulator. Their bias conditions, $i_{dc} = 0$, $\beta_c = 16$, are very similar to those of Pedersen and Davidson, and their state diagram (Fig. 2.5b) comes out quite similar to Fig. 2.5a. Again, the minimum drive amplitude i_{ac} for seeing chaos occurs at lower than the plasma frequency, at $f_L/f_p \approx 0.6$ in their diagram. Their larger f_L/f_p range showed interesting phenomena at both high and low frequency ends. At the high frequency end, $f_L/f_p \approx 1$, the chaos threshold goes up quite quickly, up from $i_{ac} \approx 0.5$ at $f_L/f_p \approx 0.6$ to $i_{ac} \approx 1.8$ at $f_L/f_p = 1$. In fact, our own analog simulation shows that the chaos threshold i_{ac} diverges very quickly when the driving frequency is above the plasma frequency; the minimum i_{ac} for seeing chaos is bigger than 5 when $f_L \approx 1.5 f_p$ (cf. Fig. 4.7). The argument given later in this section will predict that when $f_L >> f_p$, chaos is very unlikely to happen. At the low frequency end, the chaos threshold seems flat at $i_{ac} \approx 1.0$. The onset of this flat curve takes place at $f_L/f_p \approx 0.25 = Q^{-1} = \beta_c^{-1/2}$ (ref. 9). This seems to be true in general from our own studies of the state diagram (cf. Fig. 4.7) for the underdamped case ($\beta_c > 1$). A possible explanation is that when $f_L < (1/RC)$ (equivalent to $f_L/f_p < \beta_c^{-1/2}$), the system is in an adiabatic regime so that its responses are frequency

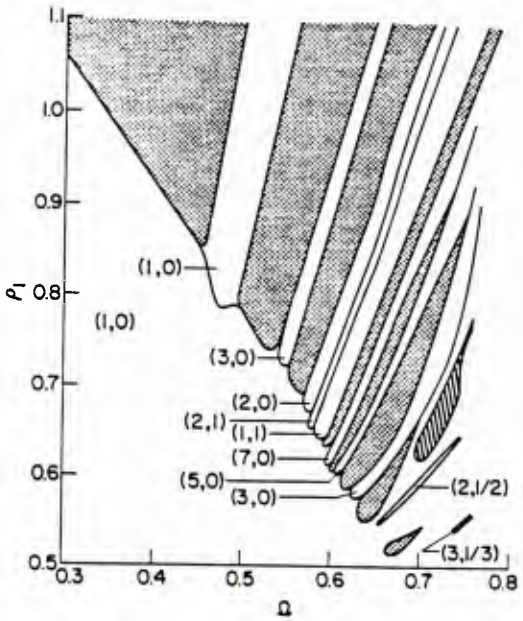

Fig. 2.5(a) State diagram in the i_{ac} - f_L/f_p plane ($\rho_1=i_{ac}$, $\Omega=f_L/f_p$ in the figure), $\beta_c=25$, $i_{dc}=0$. Cross-hatched region: chaos. Hatched region: complicated periodic solutions. Indexing (p, q) corresponds to the pth subharmonic on the qth step. (After Ref. 7)

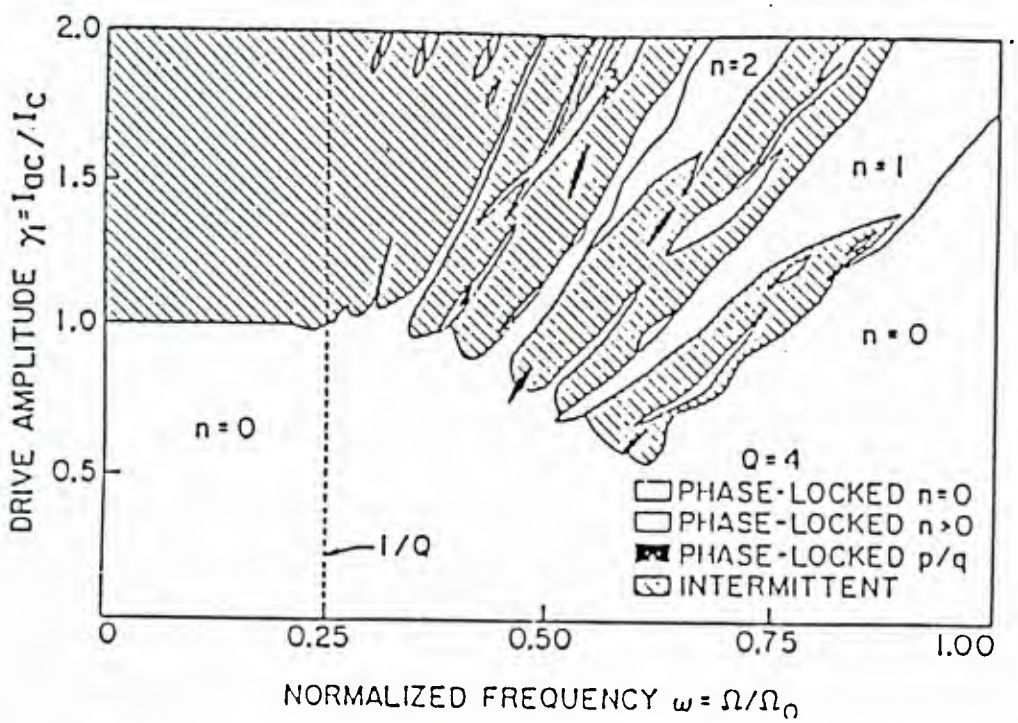

Fig. 2.5(b) State diagram in the i_{ac}-f_L/f_p plane ($\gamma_1=i_{ac}$, $\omega=f_L/f_p$ in the figure). $\beta_c=16$, $i_{dc}=0$. (After Ref. 9)

independent.

The effect of damping on the chaotic-nonchaotic state diagram can be appreciated from the state diagram computed by Cirillo and Pedersen[8] shown in Fig. 2.6a, where the curves are the chaos threshold plotted in a coarse scale. Again, the computation is done with zero dc bias, and β_c is the parameter whose numerical value appeared on each curve. We can see from Fig. 2.6a that as the damping increases (β_c decreases), the driving frequency corresponding to the minimum of the chaos threshold shifts towards lower frequency. This can be easily understood as damping tends to slow down the motion of the system. For a harmonic oscillator, damping decreases the resonance frequency by a factor of $[\,1 - 1/(4\beta_c)\,]^{1/2}$. Besides shifting the threshold curve to lower frequency, damping also increases the chaos threshold. From Fig. 2.6a, we can see for $\beta_c = 1.5$, the minimum i_{ac} for seeing chaos is already bigger than 1. Later discussion will show that chaos will not occur in a very overdamped regime. In a very underdamped regime, $\beta_c >> 1$, damping seems to have no effect on the chaotic threshold. Two threshold curves computed with $\beta_c = 25$ and $\beta_c = 175$, respectively, coincide; the curve with $\beta_c = 17$ is not too much different from the one with $\beta_c = 25$ either. This result is not surprising at all since for a harmonic oscillator, when $\beta_c \geq 10$, there is virtually no effect of damping on the natural oscillation frequency ($(1 - 1/4\beta_c)^{1/2} \approx 1$).

Octavio[10] computed the state diagram in the i_{ac} - β_c plane in a very fine scale. Fig.2.6b shows the result computed with $f_L/f_p = 0.65$. The chaotic-nonchaotic boundary for the lowest value of i_{ac} is consistent with what we inferred from Fig. 2.6a: the chaos threshold flattens out at $\beta_c \geq 20$, and diverges quite sharply when β_c approaches zero. Again, like the state diagram of fine-grid in Fig. 2.5, the state diagram of fine-grid in i_{ac}-β_c also showed a complicated structure, the chaotic regions are interupted by windows of periodic solutions as we move along either on i_{ac} or β_c.

For the four parameters in the RCSJ model (f_L/f_p, β_c, i_{dc} and i_{ac}), so far to our

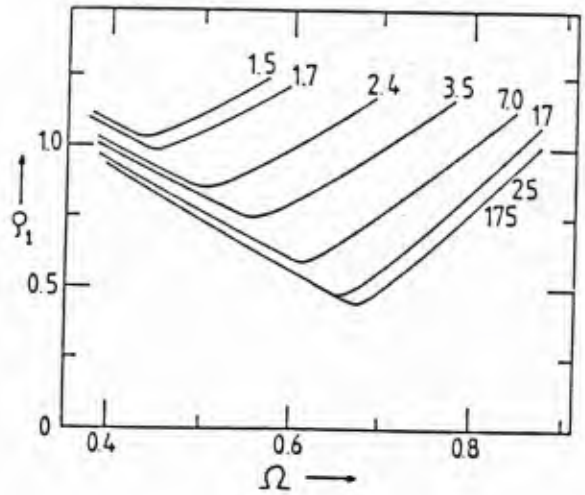

Fig. 2.6(a) Threshold curves for transition to chaos in the i_{ac}-f_L/f_p plane ($\rho_1=i_{ac}$, $\Omega=f_L/f_p$ in the figure) and β_c is the parameter. (After Ref. 8)

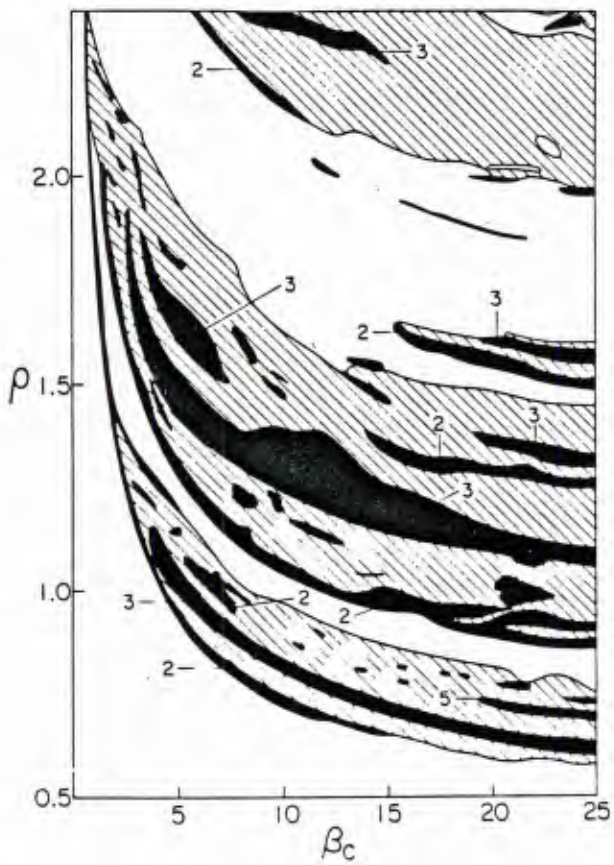

Fig. 2.6(b) State diagram in the i_{ac}-β_c plane ($\rho=i_{ac}$ in the figure) with $f_L/f_p=0.65$. Empty regions correspond to period-one solutions. Solid regions correspond to period doubling, tripling and quintupling, as indicated in the figure. The hatched regions indicate chaotic solutions. (After Ref. 10)

knowledge, there is no convincing chaotic-nonchaotic state diagrams made with i_{dc} as one of the dimensions. The main reason is that, from our own experience of studying the state diagram in the i_{ac} - i_{dc} plane in the analog simulations, unlike the i_{ac} - f_L/f_p and i_{ac} - β_c state diagrams, in which the state at a particular point is single valued (chaotic or non-chaotic), the state in the i_{ac}-i_{dc} plane is very hysteretic; it can be chaotic or periodic with different periods depending on the direction in which we sweep i_{dc} and i_{ac}. It would be very difficult to construct a several layered state diagram in i_{dc} taking the hysteresis into account. But qualitatively, we know that a small dc bias i_{dc} can cause the following effects:

1) External symmetry breaking is introduced; the effective potential is no longer symmetric for $\phi \rightarrow -\phi$ transformation; 2) the resonant frequency is lowered because the curvature at the bottom of the potential well is reduced by i_{dc}; 3) the quality factor is decreased since $Q = \omega_R RC$; 4) the critical ac drive required to produce rotation is reduced. Some of the four effects will lower the chaos threshold in certain conditions, but some will raise the threshold in other conditions. It cannot be said in general that the dc bias will definitely make chaos more likely to happen or the other way around. But qualitatively, a small dc bias ($i_{dc} < 1$) does not change the results in Fig. 2.5 and Fig. 2.6 dramatically. Thus we can still use these results for guidance in the studies of both ac and dc driven junctions. However, later discussion in this section will show that chaos will not occur for a very large dc bias current.

The attempts of making quantitative predictions on the chaos-nonchaos boundaries in Fig. 2.5 and Fig. 2.6 have not been very successful. In spite of the efforts[33,34] many people attempted to derive a quantitative boundary in parameter space within which chaos might occur, at best they can only get some lower limit of such a boundary. So far we only know qualitatively in what parameter range we might see chaos. The following discussion is based on the heuristic argument of Kautz and Monaco[27] on a model in which chaos is

caused by the interference of two incommensurate frequencies. In their model, a driven Josephson junction is characterized by a drive-dependent resonant frequency Ω_p; Ω_p is the generalized plasma frequency defined as follows. If ϕ_o is a solution of the RCSJ equation (2.12), consider a perturbed solution $\phi(t) = \phi_o(t) + \varepsilon(t)$, where $\varepsilon(t)$ is assumed to be infinitesimal. Substitution of the perturbed solution into Eq.(2.12) and linearization in ε yields

$$\frac{d^2\varepsilon}{d\tau^2} + \frac{1}{\beta_c^{1/2}}\frac{d\varepsilon}{d\tau} + \varepsilon \cos\phi_o = 0 \qquad (2.16)$$

Solution of this linear equation in ε can be written as

$$\varepsilon(\tau) = P(\tau)\, e^{a\tau} \qquad (2.17)$$

There are usually two solutions $a_\pm$ for a, where $a_\pm$ are the solutions with different sets of initial conditions:

$$\varepsilon_+(0) = 1 \qquad \frac{d\varepsilon_+(0)}{d\tau} = 0$$

$$\varepsilon_-(0) = 0 \qquad \frac{d\varepsilon_-(0)}{d\tau} = 1$$

The $a_\pm$ are in general complex numbers; their real parts determine the local stability of the solution and are known as the Liapunov exponents.

$$\lambda_\pm = \mathrm{Re}\,|\,a_\pm\,| \qquad (2.18)$$

Positive λ corresponds to an unstable solution, whose motion will diverge from the unperturbed solution exponentially in time under an infinitesimal perturbation. Not surprisingly, these exponents relate to the damping factor β_c in a very simple way:

$$\lambda_+ + \lambda_- = -\frac{1}{\beta_c} \qquad (2.19)$$

When the response of the system to infinitesimal perturbations is oscillatory, the exponent a has an imaginary part which is related to the frequency of the oscillation. These oscillations are a generalization of the plasma oscillations which exist in the absence of ac bias. We thus define:

$$\Omega_p = | \mathrm{Im} (a_{\pm}) | \qquad (2.20)$$

Ω_p is the natural response frequency (normalized to ω_p) when we bring the system from its unperturbed orbit infinitesimally. Clearly, it reduces to the resonant frequency $\omega_R=\omega_p(1-i_{dc}^2)^{1/4}$ in the absence of ac bias; in that case the unperturbed orbit is the equilibrium position in phase space. In general, Ω_p is a function of the bias conditions.

It has been known for a long time that chaos usually occurs at the bias conditions where the solutions are unstable,[11,12] i.e. $\lambda \geq 0$. The significance of Ω_p is appreciated only recently through Kautz's recent work.[32] Fig. 2.7 shows a striking coincidence of the period doubling point and $\Omega_p = \omega_L/2\omega_p$ solution. The two plots (b) and (c) are the maximum Liapunov exponent λ and Ω_p vs. $\alpha = (\omega_p/\omega_L)^2$. We can see at the critical value $\alpha_c = 0.28$, the period of RCSJ solution is doubled (i.e., the initial phase in the plot (a) is doubly valued). Correspondingly, Ω_p takes a value at <u>exactly</u> half of the normalized drive frequency ω_L/ω_p. Meanwhile, the maximum of Liapunov exponent vanishes, implying that the original period 1 solution is unstable. This striking coindidence of $\lambda = 0$, $\Omega_p = \omega_L/2\omega_p$, and period doubling has been observed under other bias conditions[32], and the coincidence of higher orders of period doubling bifurcation is observed.

What this coincidence suggests is that a Josephson junction can be viewed as a dynamic system whose response frequency is Ω_p and damping is λ, where the response frequency and damping are in the dynamic sense, as opposed to the equilibrium case in a

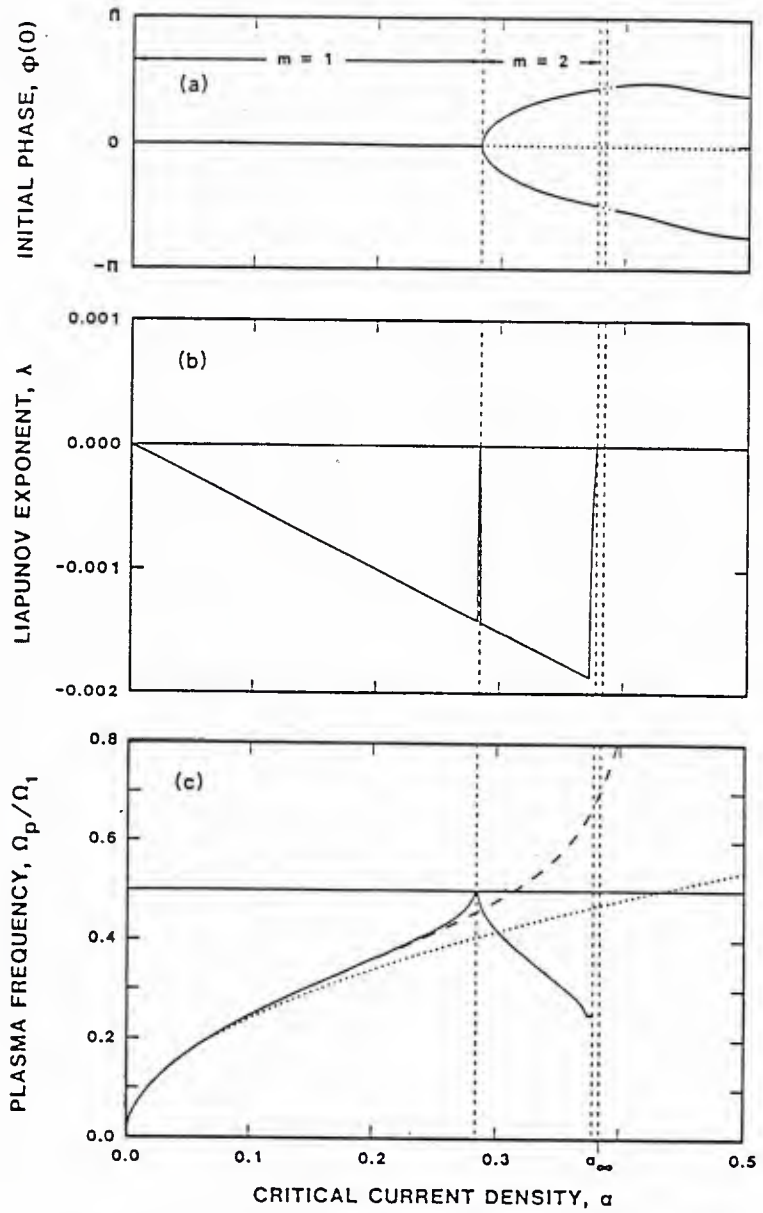

Fig. 2.7 (a) The initial phases of the m=1 (period-one) and m=2 (period-two) solutions on the n=1 step. Solid and dotted lines indicate stable and unstable solutions respectively. (b) Maximum Liapunov exponent for the stable m=1 and m=2 solutions. (c) Generalized plasma frequency normalized to the drive frequency [$\Omega_p/\Omega_1=\Omega_p(f_p/f_L)$ in the figure] for the stable m=1 and m=2 solutions, with a solid line indicating the result of numerical calculation and dotted and dashed lines indicating analytical results from approximate formulas. The horizontal axis is $\alpha=(f_p/f_L)^2$. Note the coincidence of the period doubling of ϕ ($\phi(0)$ is doubly valued), vanishing of λ, and $\Omega_p=f_L/(2f_p)$ at the same value of α. (After Ref. 32)

non-driven junction, where ω_p and β_c are the parameters. Chaos and period-doubling bifurcations are the consquences of the interference of the driving frequency and Ω_p under zero damping condition ($\lambda = 0$). Thus to make chaos happen, the driving frequency must not be too far from Ω_p.

Kautz[11] derived an approximate expression for the maximum Ω_p on a phase-locked step, which is

$$\max(\Omega_p) \approx (\Delta i_n)^{1/2} \tag{2.21}$$

where Δi_n is the width of the step concerned normalized to $2I_c$, and Ω_p is normalized to ω_p. Apparently, the maximum value of Ω_p is one, meaning the maximum of the generalized plasma resonant frequency is ω_p.

The assumption that chaos and period doubling phenomena are the consequences of the interference of the drive frequency and the natural response frequency Ω_p of the system is a plausible picture. It is supported by the evidence that period doubling and $\lambda=0$ and $\Omega_p = \omega_L/2\omega_p$ tend to associate with each other. Based on this picture, Kautz and Monaco[31] studied the parameter ranges of ω_L/ω_p, β_c, i_{dc} and i_{ac}. They claimed that chaos will not occur at those regions where the interference of the drive and Ω_p is minimum or the dynamic system is heavily damped. They predicted the non-chaotic parameters ranges as following:

$$\begin{aligned}
&(1) \quad \beta_c \ll 1 \\
&(2) \quad i_{ac} \ll 1 \\
&(3) \quad \omega_L \gg \omega_p \\
&(4) \quad \rho_{ac} \gg (\omega_p/\omega_L)^4 \\
&(5) \quad i_{dc} \gg \rho_{ac}\,(\omega_L L/R) \\
&(6) \quad \rho_{ac} \gg (\omega_L L/R)^2
\end{aligned} \tag{2.22}$$

where

$$\rho_{ac} = i_{ac}\,(R/\omega_L L)\,[\,1 + (\omega RC)^2\,]^{-1/2}$$

The first three relations are quite straight forward: (1) In the overdamped regime, there is no natural oscillatory motion; the system can do nothing but follow the driving force. (2) When the driving amplitude i_{ac} is too small, the system remains in a linear regime ($|\phi| << \pi/2$); apparently, chaos will not happen in this case. (3) When the driving frequency is far above the plasma frequency, the impedance of the capacitance is much smaller than that of the Josephson inductance, so the junction is effectively voltage biased; chaos will not happen in this case either. In Kautz's model, he argued that when ω_L/ω_p is far away from the region (0, 1), none of the natural frequency modes can be excited by the driving force (since $0 \le \Omega_p \le 1$), thus chaos will not occur. In fact, several groups[33,34] derived a theoretical prediction of (1), (2) and (3) by using the Melnikov-function technique, which assumes that chaos occurs at the bias conditions that the stable orbit intersects the unstable one. Their prediction of the threshold i_{ac}^T of chaos as a function of ω_L/ω_p, β_c, and i_{dc} is

$$i_{ac}^T > \left| |i_{dc}| - \frac{4}{\pi}\beta_c^{-1/2} \right| \cosh\left(\frac{\pi}{2}\frac{\omega_L}{\omega_p}\right) \qquad (2.23)$$

for $$|i_{dc}| \le (4/\pi)\,\beta_c^{-1/2}$$

Eq. (2.23) indicates that the chaos threshold i_{ac}^T diverges both at $\beta_c << 1$, (condition (1) in (2.23)); and $\omega_L >> \omega_p$ (condition (3) in (2.23)). The comparison[34] between this prediction and the digitally calculated state diagram is shown in Fig. 2.8. The dots are the digitally computed chaos threshold with the same bias conditions as those in Fig. 2.5a, which is i_{dc}=0, β_c=25. The solid curve is the result from (2.23) with the same i_{dc} and β_c values. The apparent lower value given by the theory is due to the coexistence of a stable periodic solution, even though there exists a non-stable chaotic solution; until i_{ac} is above the digitally calculated curve, the system will stay at the stable periodic motion.

(4) and (5) are not as apparent as (1), (2), and (3). They are due to the depression of the resonance frequency Ω_p at a finite voltage step. As stated in (2.21), the maximum

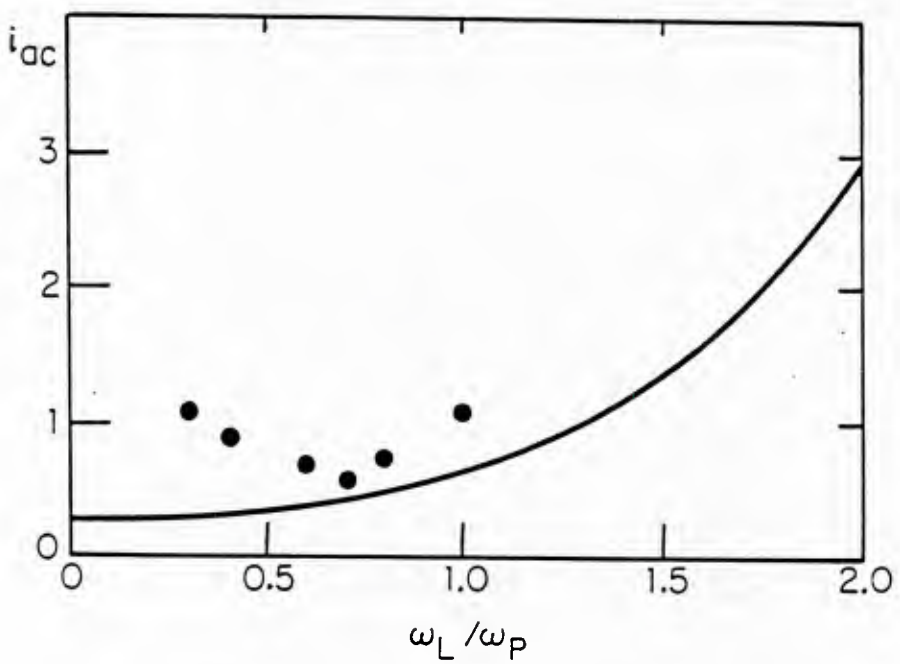

Fig. 2.8

Threshold of transition to chaos in the i_{ac}-ω_L/ω_p plane, with $i_{dc}=0$, $\beta_c=25$. Solid curve is the result calculated from Eq. (2.23). The dots are the results from numerical simulation. (After Ref. 34)

resonance frequency on a step max(Ω_p) scale as $(\Delta i_{step})^{1/2}$ (which is always less than 1 on a finite voltage step), which is a function of i_{ac} and i_{dc}. From the argument given above, we know that chaos can only occur when the normalized driving frequency ω_L/ω_p is roughly in the range (0, max(Ω_p)). Because of this depression of Ω_p at a finite voltage step, chaos will not occur for a given driving frequency if either (4) or (5) is satisfied.

(6) comes from the fact that chaos usually occurs when there are overlapping steps. (cf. 2.3.1(C), in the transition from quasiperiodicity to chaos, chaos does not occur until the bias conditions are reached, at which there are overlapping steps.) At very high ac amplitude, all the steps are so small that none of them are overlapping, thus chaos will not occur in this case.

So far, all the published digitally calculated state diagrams[6-10] are consistent with the conditions (2.22), so we can use (2.22) to guide the search for chaos in a Josephson junction or the design of a non-chaotic practical device.

2.4 Effect of noise on a Josephson junction

Most of the simulation studies done on chaos are focused on the noise-free case. People are interested in the chaotic output of a purely deterministic nonlinear system with a clean sinusoidal signal input. But in the study of a real Josephson junction, we can not afford ignoring the inevitable fluctuations at finite temperature and finite voltage. In some highly nonlinear regions, where the system is extremely sensitive to perturbations, the noise equivalent to thermal noise of several degrees temperature can trigger some chaotic motions which are experimentally indistinguishable from intrinsically chaotic ones. Thus in a real experiment, we are always dealing with the interplay of noise and a nonlinear system. In the following argument, we will estimate how strongly the noise affects the Josephson system.

In thermal equilibrium, each degree of freedom has a $(1/2)k_BT$ energy. If we apply

this to the RCSJ model (2.1), we can find the root-mean-square of the distribution of the phase:

$$\delta\phi_{rms} = \left[k_B T \left(\frac{2e}{\hbar I_c}\right)\right]^{1/2} = \left[\frac{2}{\gamma}\right]^{1/2} \qquad (2.24)$$

If we use standard theoretical relations[35] to relate I_c to the normal-state resistance of the junction R_n and the superconducting transition temperature T_c through the superconducting gap energy, this can be transformed to

$$\delta\phi_{rms} = \left[\frac{T}{T_c}\right]^{1/2} \left[\frac{R_n}{1.38\hbar/e^2}\right]^{1/2} \sim 0.01 \qquad (2.25)$$

for $T/T_c \sim 1/2$ and $R_n \approx 1$ohm, which are typical parameters for the junctions studied in this report.

This magnitude of fluctuation certainly can have very significant effects in washing out subtle structures found in noise-free calculations. Many people have studied the noise effect on a Josephson junction with or without ac driving.[36-38] The agreement between these theories and the experiments is very good, showing the power of classical statistical mechanics in predicting a totally random process.

2.4.1. Noise effect on an autonomous Josephson junction ($i_{ac} = 0$).

In this case, the RCSJ model including noise is:

$$\frac{d^2\phi}{d\tau^2} + \frac{1}{\beta_c^{1/2}} \frac{d\phi}{d\tau} + \sin\phi = i_{dc} + i_n(\tau) \qquad (2.26)$$

where β_c, i_{dc} are defined the same way as (2.12); i_n is the noise current. For the time being, for simplicity reasons, we assume that i_n is the noise current caused by thermal noise. Then its power spectrum is frequency independent, and its randomness can be fully characterized by the autocorrelation function:

$$\langle i_n(\tau)\, i_n(\tau+\tau')\rangle = \frac{4}{\beta_c^{1/2}}\,\frac{1}{\gamma}\,\delta(\tau') \qquad (2.27)$$

where τ and τ' are times measured in units of ω_p^{-1}, and γ is defined the same way as in (2.24). Eq. (2.27) is the dimensionless equivalent of the more conventional formula:

$$\langle I_n(t)\, I_n(t+t')\rangle = 4\,\frac{k_B T}{R}\,\delta(t') \qquad (2.27a)$$

(Note that $\delta(t') = \delta(\tau')\,\omega_p$). The dimensionless formula (2.27) tells that the combination of the dimensionless parameters β_c and γ is the measure of the noise level in the system. Two systems having the same values of β_c and γ are subject to the same level of noise, regardless of whatever their absolute parameters may be. Apparently, this statement is also valid in a nonautomous case ($i_{ac}\neq 0$).

Eq. (2.26) is exactly the same as that for a particle moving in a potential with damping and subject to Brownian bombardment. The potential $U(\phi) = -(\cos\phi + i_{dc}\phi)$ is plotted vs. ϕ in Fig. 2.9. Pictorially, it looks very much like a tilted washboard, and people quite often refer this potential as a "tilted washboard" potential. Without noise, the particle will stay in one of the potential wells (if it was there at the initial moment) until the tilt makes the energy barrier ΔE vanish, which corresponds to $i_{dc} = 1$. Then the particle starts rolling down the potential; the finite speed it gains as it slides down in the presence of damping corresponds to the finite voltage ($V \propto d\phi/dt$), which appears on the dc I-V curve. However, in the presence of noise, even before $i_{dc} = 1$ is reached, the noise can kick the particle out of the potential well and make it start sliding down. The way the particle slides down can be quite different, depending on the damping. For a harmonic oscillator:

$$\frac{d^2\phi}{d\tau^2} + \frac{1}{\beta_c^{1/2}}\,\frac{d\phi}{d\tau} + \phi = 0$$

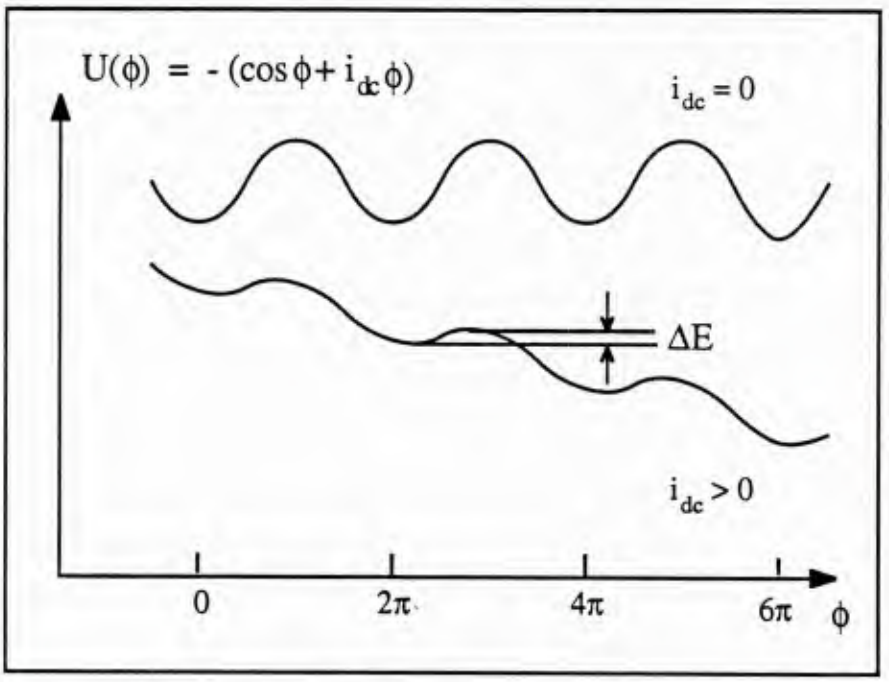

Fig. 2.9

Schematic of the tilted washboard potential.

we know that the critical value of $\beta_c = 1/4$ divides the solutions into two quite different categories. One ($\beta_c > 1/4$) is underdamped, the motion is oscillatory, and the pendulum will pass its equilibrium point many times before settles down. The other ($\beta_c < 1/4$) is overdamped, the pendulum will approach the equilibrium point with infinitesimal speed, and never pass it. In our case, even though the system is nonlinear, the above picture is still correct in the sense that there is a critical value of damping. Above it is the overdamped regime, in which the escaping particle will be recaptured by the next well and has to stay there for a while to be kicked out again. Below the critical damping, in the underdamped regime, the particle will gain enough kinetic energy during the acceleration process to be able to climb over the next energy barrier. It then keeps accelerating until the stable speed

is reached, at which the damping force counter-balances the gravitational force. The I-V curves corresponding to the two regimes have quite different features; also, the noise effects in the two regimes are quite different. One can imagine the noise has more effect on an underdamped regime since when the particle is kicked out, nothing will stop it; while in the overdamped regime, the noise has to kick the particle out of each well in turn.

Kramers[39] did a very detailed study on noise-activated escape phenomena in his historic paper dated in 1940. He discussed three separate approximations, depending on the degree of damping: light, moderate, and heavy damping. Other researchers[36-38] applied his results to Josephson junctions and found the following results:

A) Overdamped regime.

Ambegaokar and Halperin[36] first studied the extremely overdamped case with β_c=0. Their results can be summarized as follows.

In an extremely overdamped regime ($\beta_c = 0$), the heavy damping makes the drift velocity much smaller than the average speed of Brownian motion, so the velocity distribution can be well characterized by a Maxwell distribution. Then the two-dimensional Fokker-Planck equation which governs the two-dimensional distribution function $P(\phi, d\phi/dt, t)$ will reduce to the one-dimensional Smoluchowski equation, which can be solved by integration. The escape rate τ^{-1} thus obtained can be related to measurable quantities in such a way that in an overdamped regime, since the particle can only hop a distance 2π at once, $2\pi\tau^{-1}$ gives the average speed of the particle thus the average voltage of the junction, i.e.

$$\frac{2eV_{dc}}{\hbar} = 2\pi\tau^{-1} \qquad (2.28)$$

The numerically integrated I-V curves are shown in Fig. 2.10, where different curves correspond to different levels of noise characterized by γ. Although the results of

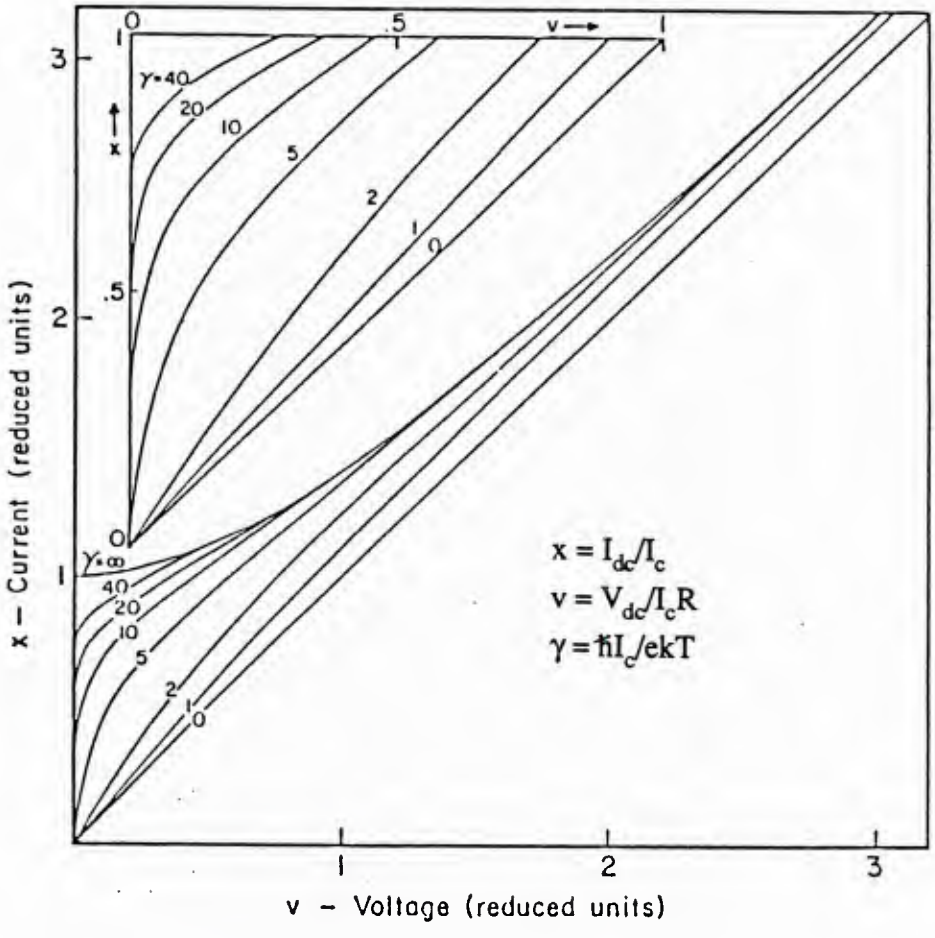

Fig. 2.10

Current-voltage characteristics of Josephson junction at different noise levels in the β_c=0 limit. (After Ref. 36)

Ambegaokar and Halperin were derived in the limit of $\beta_c=0$, P.A. Lee showed[36] that these results were also valid in the finite β_c case, as long as $\beta_c<<1$ is satisfied. The results of Fig. 2.10 have been very well verified by many experimental groups. (Ref. 40, for example.)

B) Underdamped regime. ($\beta_c >> 1$)

P.A. Lee[38] got the following result for the escape rate from a potential well.

$$\tau^{-1} = \frac{\omega_A}{2\pi} e^{-\Delta E/k_B T} \qquad (2.29)$$

where $\omega_A = \omega_p(1 - i_{dc}^2)^{1/4}$ is the oscillation frequency at the bottom of the potential well reduced from ω_p due to dc bias.

$$\Delta E = \frac{\hbar I_c}{e} [\, i_{dc} (2\sin^{-1} i_{dc} - \pi) + 2 \cos (\sin^{-1} i_{dc})] \qquad (2.30)$$

is the energy barrier shown in Fig. 2.9. This result (2.29) can be understood very easily: in unit time, the particle will try $\omega_A/2\pi$ times to escape, but only those which have energy comparable to ΔE have a chance to succeed. The fraction of these particles among the total is $e^{-\Delta E/kT}$, which explains the Boltzmann factor in (2.29).

In principle, we can measure this escape rate directly. In this underdamped regime, the particle will accelerate to its full speed whenever it is kicked out of the well. By providing a sudden dc bias i_{dc}, and measuring the delay time for the system to switch to the finite voltage state, we will get the lifetime τ as a function of i_{dc}. However, this is not the way most people measure τ^{-1}.

Since this premature switching (switch at $i_{dc} < 1$) is caused by random kicking, the system will not switch at the same place if we repeat the process. Instead, we will get a distribution $P(i_{dc})$ which is related to τ^{-1} by[41]

$$P(i_{dc}) = \tau^{-1}(i_{dc})(\dot{I})^{-1}\left[1 - \int_0^{i_{dc}} P(u)\,du\right] \qquad (2.31)$$

where the third factor on the right is the fraction of the systems (in a statistical ensemble) which remain unswitched when i_{dc} is reached in the sweep. Apparently, the switching probability should be proportional to that. Also, the switching probability should be proportional to the escape rate τ^{-1}. I is the rate at which we sweep the dc bias current. If we sweep very fast, the system will not have much chance to switch at i_{dc}, thus $P(i_{dc})$ is inversely proportional to the sweep rate.

Fig. 2.11a is a schematic drawing of a set of $P(i_{dc})$ at different temperatures. It shows that, as the temperature increases, the system tends to switch at smaller dc current i_{dc}; also the switching spreads out over a bigger range. The width of the distribution σ varies with temperature roughly as $T^{2/3}$, as shown in Fig. 2.11b[24].

With the measured switching distribution $P(i_{dc})$, we can easily infer the escape rate τ^{-1}. Many experiments[41, 23-25] have been done to check (2.29), and, so long as sufficient care is given to excluding extraneous noise, all the reports agree with (2.29) very well except at very low temperature, where the macroscopic quantum tunneling rate dominates the thermally activated hopping.[23-25]

From Fig. 2.11a, we can see that the peak postion of $P(i_{dc})$ is changing with temperature. In an experiment, this peak position corresponds to the measured critical current, since the maximum of $P(i_{dc})$ is the point at which the system most likely to switch to nonzero voltage state. Danchi et al.[42] derived an approximate formula to relate this peak position i_c^{exp} with γ (inversely proportional to temperature). Their result is:

$$i_c^{exp} = 1 - \left\{\left[\frac{3}{\sqrt{8}\,\gamma}\right]\ln\left[\frac{\omega_p I_c}{\pi\sqrt{8}\,\gamma\dot{I}}\right]\right\}^{2/3} \qquad (2.32)$$

We have checked this result in our simulations (Chapter IV). The agreement is

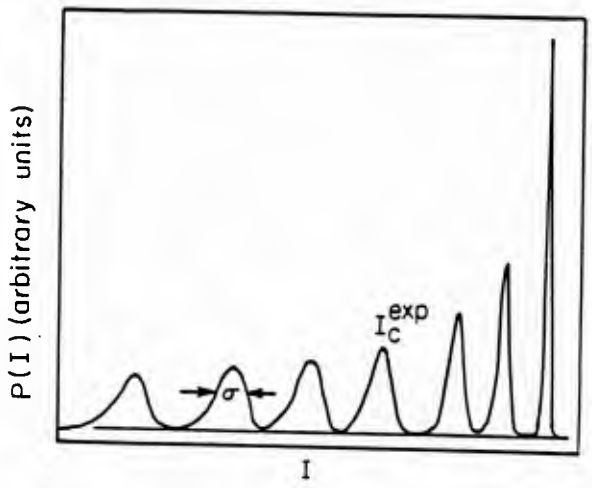

(a)

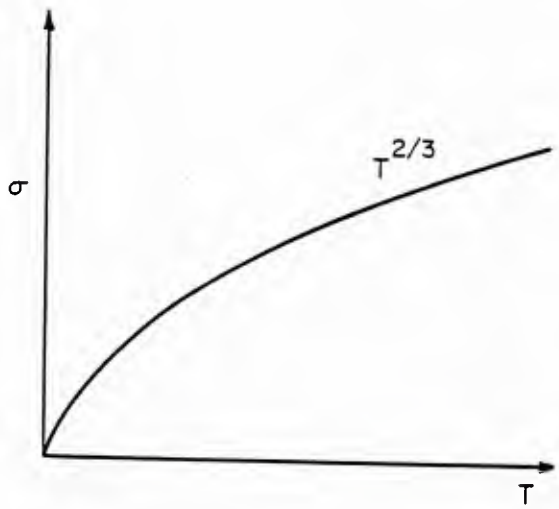

(b)

Fig. 2.11

(a) Schematic of the probability of the noise-induced premature switching vs. the dc bias current. (b) Schematic of the width of the switching distribution vs. temperature.

very good even for the $\beta_c \approx 1$ case, even though this formula is derived in the $\beta_c = \infty$ limit.

From (2.32), we can see that besides the thermal energy parameter γ, the dimensionless factor $(\omega_p I_c / \dot{I})$ also determines the measured critical current. Although this logarithmic dependence is not a very sensitive function, in a simulation study, due to the slowness of simulations, digital or analog, $\omega_p I_c / \dot{I}$ is usually many orders of magnitude smaller than that of an experiment. In a digital simulation, we can make ω_p and I_c the same as that in the experiment, but in order to produce an I-V curve in ~10 hours, we have to make the sweep rate dI/dt about 10^8 times of the experimental sweep rate, thus making the factor $\omega_p I_c / \dot{I}$ about 10^8 times smaller than that in the experiment. In an analog simulation, we can make I_c and I the same as that in the experiment, but $\omega_p/2\pi$ is typically not much higher than 10^4 Hz, compared to the typical plasma frequency in a real Josephson junction 10^{12} Hz, so we have a factor of 10^8 difference again in the factor $\omega_p I_c / \dot{I}$.

One must compensate for this large disparity in $\omega_p I_c / \dot{I}$, which makes infrequent events not observable in simulations. Quantitatively, if we wish to make the simulated measured critical current the same as that of the experimental one, we have the following relation:[42]

$$\frac{\gamma^{exp}}{\gamma^{sim}} = \frac{\ln\left[\omega_p^{exp} I_c^{exp} / \sqrt{8}\,\pi\gamma^{exp}\dot{I}^{exp}\right]}{\ln\left[\omega_p^{sim} I_c^{sim} / \sqrt{8}\,\pi\gamma^{sim}\dot{I}^{sim}\right]} \qquad (2.33)$$

This result can be generalized to a more general case when an ac drive is present. Recalling from (2.24) that

$$\gamma = \frac{\hbar I_c}{e k_B T} = \frac{2}{(\delta\phi_{rms})^2} \qquad (2.34)$$

which tells the relative height the energy barrier compared to the thermal energy, γ

determines the effect of noise on switching behavior. However, we have to keep in mind that the frequency range in a real experiment (the attempt frequency $\omega_a/2\pi \sim 10^{12}$ Hz) is quite different from that of simulations (10^4 Hz typically). This large disparity in frequencies makes some rare switching event observable in a real experiment but not in a simulation for the same noise level γ. To compensate this lack of chances, we have to increase the noise temperature in simulations to make the less frequent events observable in simulations. Quantitatively, if we assume the peak rather than the rms value of noise plays the key role in triggering the system switch from one state to another (which is apparently the case in dc switching, since only the noise that can kick the particle above the energy barrier plays a role in triggering switching), then for Gaussian noise, the probability that an excursion equalling or exceeding a critical amplitude $\Delta\phi$, sufficient to switch to another attractor, is reached in $N_a = \omega_a/2\pi$ attempts (per unit time), is

$$P = N_a e^{-\gamma(\Delta\phi)^2/4}$$

Roughly speaking, P=1 can serve as a criterion, below which the system remains unswitched, and above which the system has switched. With this rough criterion, we can determine a threshold value of noise level, above which the noise will trigger the system switch from one state to another. Thus by setting P equals to unity, we obtain the threshold condition:

$$\gamma(\Delta\phi)^2/4 = \ln N_a$$

Notice that in both experiments and simulations, the critical amplitude $\Delta\phi$ is the same. Thus we can relate the threshold of noise level in the experiment and simulation in the following way[43]:

$$\frac{T_{sim}}{T_{exp}} = \frac{\gamma_{exp}}{\gamma_{sim}} = \frac{\ln N_a^{exp}}{\ln N_a^{sim}} = \frac{\ln 10^{12}}{\ln 10^4} = 3 \qquad (2.35)$$

This result is consistent with the result derived for the autonomous case (2.33)

where the effective noise temperature in experiments and simulations is scaled the same way as (2.35) except where N_a is more explicitly written as $(\omega_p I_c / \dot{I})$.

2.4.2 Noise effect on a nonautonomous Josephson junction ($i_{ac} \neq 0$).

P.A. Lee[38] studied the noise effect on a radiation-induced Josephson step for an overdamped case. His results are summarized as follows: In an ac voltage-biased junction, on a radiation-induced step (n = integer), the corresponding Fokker-Planck equation is essentially the same as that for a purely dc biased junction in the zero-voltage state, except

a) The current and the voltage should be understood as the increments from the center of the step.

b) The critical current I_c is replaced by the noiseless half width of the current step in question $I_n = I_c J_n(\alpha)$. Thus the dimensionless noise intensity now is

$$\frac{1}{\gamma} = \frac{k_B T}{\hbar I_n / e}$$

c) There is an extra noise term due to the finite linewidth Δf of the radiation. The equivalent effective noise temperature is given by

$$T_{\Delta f} = \frac{n^2 \Delta f}{2\left(\frac{2e}{\hbar}\right)^2} \frac{I_c}{I_n} \frac{1}{R k_B} \qquad (2.36)$$

for the nth step.

a) and b) will make a radiation-induced step have a noise-rounded corner very much like the one in the autonomous case (Fig. 2.10) except the current and the voltage are now measured from the center of the step. As for c), for the typical parameters of the junctions we have studied, and a narrow linewidth of a coherent laser radiation, ($\Delta f \approx$ 1-10 MHz) $T_{\Delta f}$ is not too important for lower order Josephson steps ($T_{\Delta f} \leq 0.2$K for Δf=10MHz, I_c/I_n=5, R=3Ω, and $n \leq 2$).

Although Lee's theory has been tested favorably[42,44], its applicability to the junctions studied in this report is very questionable. The main reason is that we are in an ac current biased case, and the associated subharmonic steps are not included in the theory. In addition, our high β_c (≥ 4) values make our junctions underdamped, and the associated hysteresis is another feature not included in the theory. A noise-induced premature switching seems to be a better picture in this region. But due to all the complexities of nonlinear dynamics, the noise effect on both dc and ac current driven junctions is far more complicated than the autonomous ($i_{ac}=0$) case (Eq. (2.29)). To our knowledge, there is no analytical result for the effect of noise on an ac current-biased junction in an underdamped regime. In Chapter V, we will discuss the noise-induced switching in a special region where the dimension of the basin boundaries is close to the dimension of the basin itself.[45]

So far, all the theoretical derivations assumed the noise current in (2.26) is caused by thermal noise. From its autocorrelation function (2.27), we know that the noise power spectrum is white (frequency-independent), and its spectral density only depends on the thermal bath temperature T. This assumption is justified when we deal with the switching problem from a zero-voltage state, and it has been very well verified[41,23-24]. However, in an ac driven Josephson junction, unlike a dc switching experiment in which the junction stays in the zero voltage state until switches, we often deal with Josephson steps at finite voltage. Especially in the far-infrared frequency range, the eV at the finite voltage steps is of the order of thermal energy $k_B T$. There is then an extra noise in addition to thermal noise at the bath temperature, due to the incoherent quasiparticle tunneling current. The noise power spectrum caused by quasiparticle current is given by[46]

$$P_I(\omega) = \frac{e}{2\pi}\left\{ I_{qp}(V+\frac{\hbar\omega}{e}) \coth\left[\frac{eV+\hbar\omega}{2k_B T}\right] + I_{qp}(V-\frac{\hbar\omega}{e}) \coth\left[\frac{eV-\hbar\omega}{2k_B T}\right] \right\} \tag{2.37}$$

where the noise power spectrum is related to the rms value of noise current by the relation:

$$\langle \delta I^2 \rangle = \int P_I(\omega)\, d\omega \qquad (2.38)$$

In the zero voltage and frequency limit, this noise power spectrum will reduce to that of the Johnson noise formula. But in general, this power density is higher than a pure thermal noise, since besides thermal fluctuations, this formula includes two more fluctuations: 1) fluctuation in the numbers of charge carriers in transport due to the discreteness of quasiparticles; 2) quantum fluctuation of an electromagnetic field in its ground state. At far-infrared frequencies, these two fluctuations are comparable or larger than thermal fluctuations, so we can not ignore them anymore. From (2.37), we can see that the complete noise form is a nonlinear function of V and ω. It is difficult to construct such a complicated noise form in simulations, especially in analog simulations. Chapter V will discuss how to approximate this complicated noise form by an equivalent thermal noise.

There are two kinds of charge carriers participating in the charge transportation process: Cooper pairs and quasiparticles. If the pairs tunnel independently of one another in analogy with quasiparticles, a dc supercurrent I_s should be accompanied by a pair shot noise of spectral density:

$$P_s = \frac{2}{2\pi} (2e)\, I_s \qquad (2.39)$$

where 2e is the pair charge. The existence of such a noise source would play an important role, especially on the zero-voltage state. But so far, all experimental evidence indicates that such a fluctuation does not exist (10^{-5} - 10^{-11} below the predicted value from (2.39)[47]). This suggests that the Cooper pair tunneling is a coherent process, with no associated fluctuation.

CHAPTER III

EXPERIMENTAL TECHNIQUES

3.1 Introduction

The major experimental work reported here was done on a series of Nb-aSi-Nb junctions made by the SNAP (Selective-Niobium-Anodization-Process) technique. These junctions have a fairly high critical current density (~ 9000 A/cm^2) and low resistance (a few ohms). The all-refractory-metal nature of these junctions turns out to be a very attractive feature for practical purposes. The junctions are extremely durable. During four years, the junctions' I-V characteristics have not changed noticeably, despite the fact that some of the junctions have thermally cycled between room temperature and liquid helium temperature about one hundred times. Besides, the junctions' tunneling barrier (~40Å Si) is very resistant to electric shocks; the junctions' resistance can be measured directly with a hand-held digital voltmeter, which sends an electric shock big enough to damage quite a few other types of junctions (Sn, NbN for example).

The radiation source is a CO_2 laser-pumped far-infrared laser, described in detail in two previous Technical Reports[48,49]. The cryostat is a metal dewar made by Cryogenic Associates with a quartz window allowing the desired radiation to go through. Extremely careful attention has been paid to noise shielding and ground loop problems. This chapter will deal with all these experimental aspects.

3.2 Sample preparations

The Nb-aSi-Nb junctions were made at Sperry Research Laboratory by their well-developed SNAP (Selective-Niobium-Anodization-Process) technique[50-52]. The following is a brief review of it.

A cross-sectional view of the completed device is shown in Fig. 3.1. The process begins with a trilayer of Nb, amorphous Si (aSi), and Nb, which have been previously deposited on a 2" oxidized Si wafer. The aSi barrier was partially hydrogenated, as part of a series of experiments aimed at improving device quality. A layer of SiO_2 (not shown) is deposited and patterned by a wet chemical etch, leaving squares of material wherever junctions are desired. This serves as a mask during the anodization step, during which the Nb counterelectrode is converted to Nb_2O_5 everywhere except under the SiO_2. The anodization is performed at room temperature. The electrolyte is a mixture of 156-g ammonium pentaborate, 1120 ml ethylene glycol, and 760 ml H_2O. A platinum cathode is used, and electrical contact to the partially submerged Nb anode is made above the surface of the electrolyte. Niobium is the only anodic conductor exposed to the electrolyte. A bar of photoresist prevents the surface of the meniscus of the electrolyte from contacting the niobium, which insures that a well-defined area is anodized. With these precautions the anodization process itself provides a means of detecting when the entire unprotected Nb layer is completely anodized. The remainder of the SiO_2 is then etched away. While photoresist can also be used as the anodization mask, SiO_2 is preferred for small undercutting or perimeter effects. The anodized trilayer, which has essentially been converted to an insulated base electrode, is next patterned by plasma etching, forming half of the antenna structure. A second SiO_2 layer is then deposited, and "vias" are etched down to the junctions. This SiO_2 serves three functions: 1) it insulates the edges of the patterned trilayer; 2) it reduces the parasitic capacitance of the completed device; 3) it serves as an etch stop for the final Nb layer. The device is completed by depositing and patterning a Nb layer which contacts the junction and forms the other half of the antenna. With the sole exception of the Nb_2O_5, all layers were formed by sputter deposition and were subsequently patterned by subtractive etching through a photoresist mask. It is important to point out that the crucial part of the junction, the Nb-aSi-Nb trilayer, is deposited

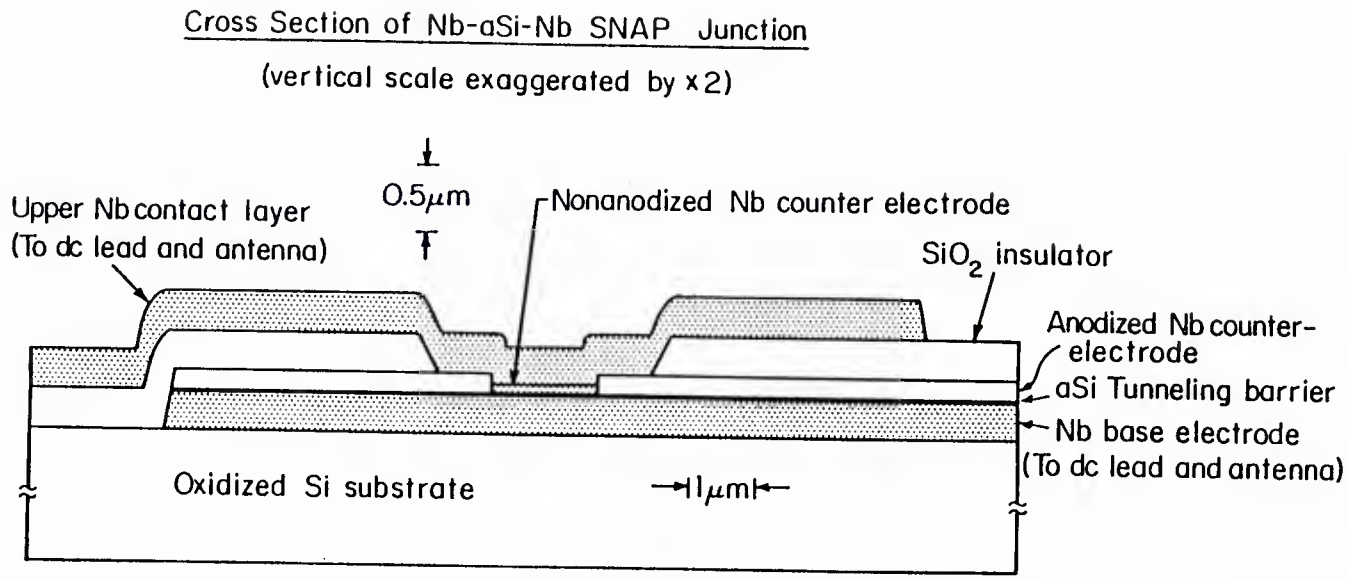

Fig. 3.1

Cross sectional view of a SNAP junction.

without breaking vacuum.

Fig. 3.2 displays four SEM micrographs at increasing magnification of a SNAP junction at the center of a ~180 μm long dipole antenna used for coupling to the FIR laser source. The junction has a tunnel area ~2μm^2. Fig. 3.2(a) shows one-half of a 2mm×4mm chip upon which two devices are fabricated. The dipole antenna is the top of the "T" in the top part of Fig. 3.2(a). At the bottom of the figure 100μm×200μm pads can be seen, to which 25μm diameter gold lead wires have been bonded. This sample chip is glued to a 6mm×6mm Si carrier chip. Gold lead wires connect the small pads on the 2mm×4mm junction chip to larger (1mm×1mm) pads on the carrier. A close-up of the 10 μm line-width antenna is shown in Fig. 3.2(b). In this micrograph the antenna axis is vertical. The horizontal bars on the left are the two dc leads. A further close-up is shown in Fig. 3.2(c) and (d). The smallest square at the center is the tunnel junction, which consists of successive layers of Nb, aSi, nonanodized Nb, and the contact layer of Nb, as also shown in the center of Fig. 3.1.

The next larger square, ~3.3μm across, is the via etched in SiO_2. Here, the base electrode and the contact layer are separated by the thin aSi barrier layer and Nb_2O_5. This region is estimated to contribute 0.016pF of the parasitic capacitance across the tunnel junction. The larger (11μm)^2 region of overlap, where the SiO_2 greatly decreases the specific capacitance, is estimated to contribute another 0.016pF to the parasitic capacitance.

The capacitance of the junctions cannot be measured directly; we can only estimate it from the measured area and the specific capacitance of the junction. The junction area could not be accurately measured from the micrograph, because the junction is covered by a layer of Nb which tends to shift the apparent edge of the junction inward by an unknown distance, as shown in Fig. 3.2. A better estimate of the area is found by dividing its measured critical current by the critical current density, which was estimated to be 9000Å/cm^2 from measurements with larger junctions. The specific capacitance was

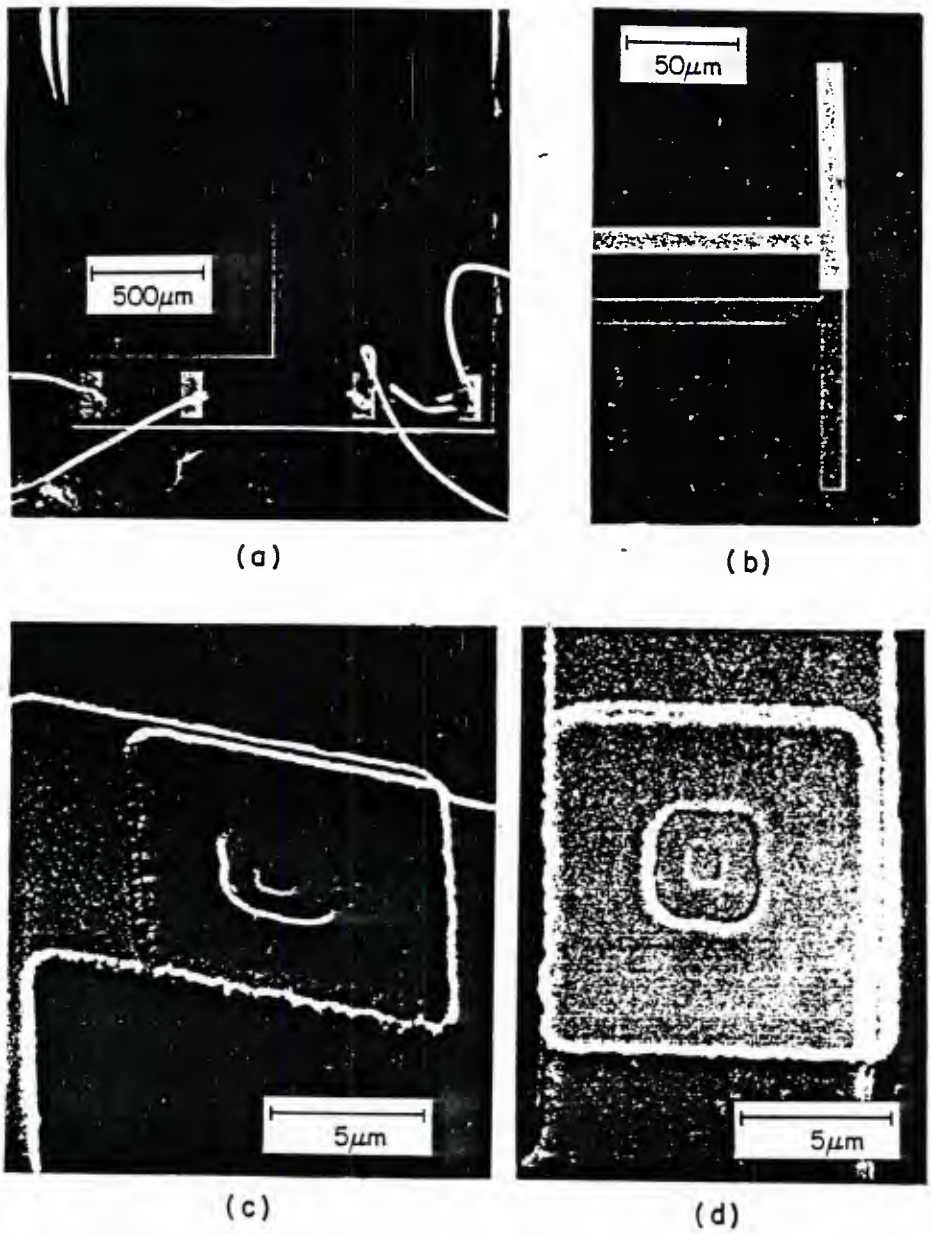

Fig. 3.2

SEM photographs of a SNAP junction.

(a) One-half of a 2mm×4mm chip with two devices. (b) Close-up of the antenna region at the center of (b). (c) Close-up of the junction region at the center of (b). The junction is the smallest area at the center of the two larger squares. (d) Same magnification with (c) but viewed from a different angle.

measured to be (0.035 pF/μm^2) (±15%) from resonances in SQUIDs prepared on the same wafer, using junctions of the same current density but of larger area (7μm^2). Since the critical current density varies by 50% accross the whole wafer, the junction area estimated in this way can only be accurate to several tens of per cent. Including the uncertainty in the specific capacitance, we can only estimate the junction capacitance at best to 20-30% (0.11±0.03pF). Chapter V will discuss how to determine the capacitance more accurately by comparing the experimental results with simulations.

A typical dc I-V curve without radiation is shown in Fig. 3.3. The not-too sharp gap structure and the subgap structure at $(\Delta_1+\Delta_2)/2$ indicate that the junction is shorted by some small area metallic link[52]. This is verified by our measurement of the depression of the critical current by a magnetic field; we could not depress the critical current to zero but only to 10% of its original value by magnetic field. Also, the R_{leak}/R_n ratio is quite low (~3) compared to the oxidized-soft-metal-barrier junction (~10 typically). This high leakage feature makes the junction not a very good candidate for SIS mixers; its photon-assisted-tunneling steps are not too sharp. But despite this drawback, the junction is extremely robust in both thermal cycling and surviving electric shocks. At Sperry Lab. it has been reported[51] that some of the similar junctions have been thermally cycled 600 times between room temperature and liquid helium temperature, with no apparent changes in critical current greater than ~1%. Also, the aSi barrier seems to be very strong to electric shock. It was reported[53] that the junction can stand a half-volt electric shock; this enables us to use a normal DVM to measure the resistance of the junctions. The junctions have perhaps gone through many unexpected shocks without being destroyed. Its robust features make a SNAP junction a very reliable element in all the potential applications of Josephson devices.

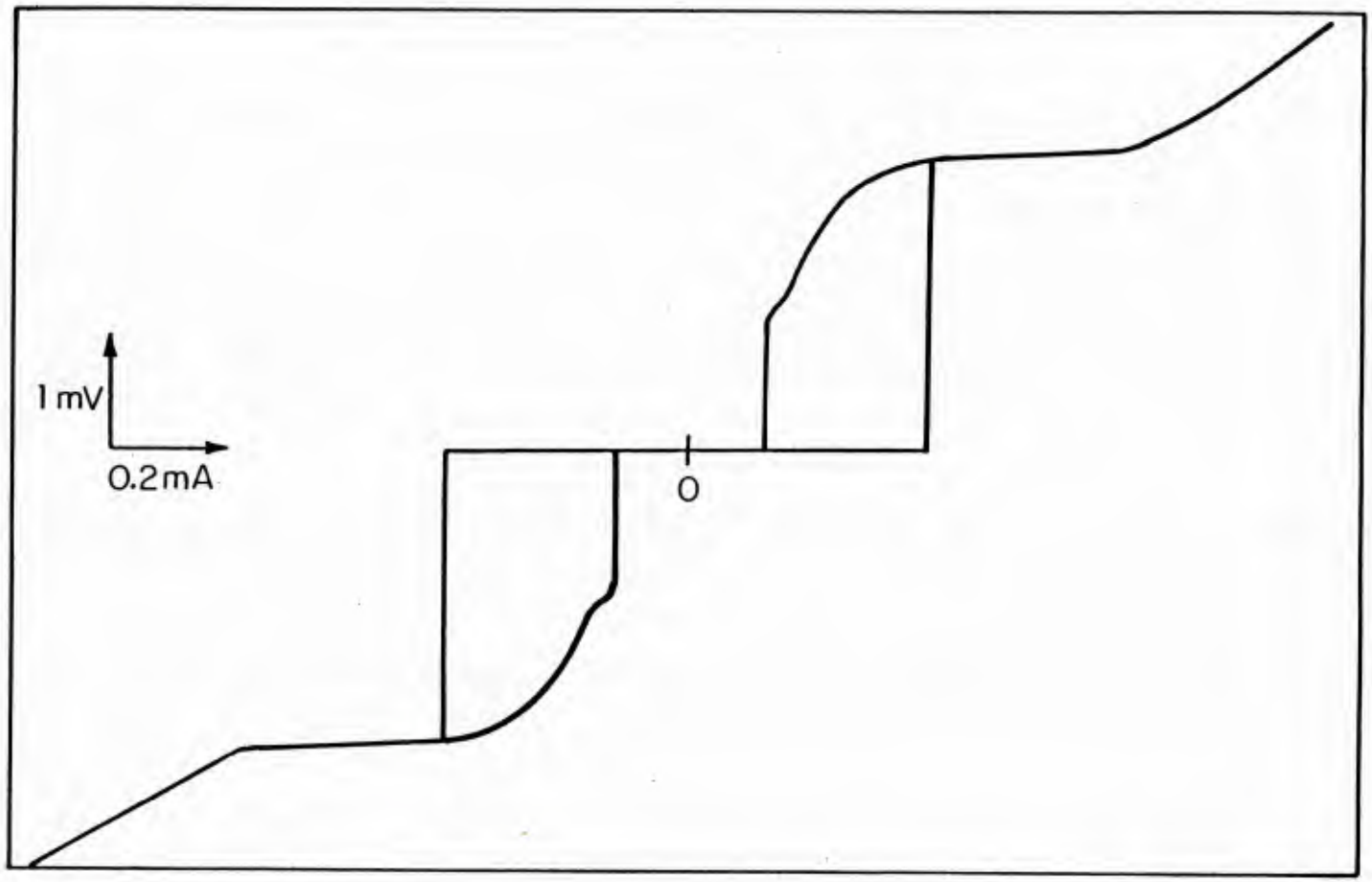

Fig. 3.3

Dc I-V curve of the SNAP1 junction.

3.3 Laser and coupling antenna

3.3.1 The laser source

The laser set up shown in Fig. 3.4 is essentially the same as that in the previous Technical Report[49], except for some minor changes:

i) We moved the chopper from in front of the CO_2 laser to in front of the pyroelectric detector. The advantage of doing this is that we do not have to stop the chopper when we take data, so we can continue monitoring the laser power level during data taking. Also, the new optical path makes the beam splitter more perpendicular to the beam (~80° compared to ~45° before), so less power is reflected by the beam splitter, more power goes into the dewar.

ii) The vacuum window for the FIR laser cavity used to be made of BaF_2, which functions pretty well in the shorter wavelength range of the CO_2 laser radiation, 9.2-11.2μm, (the pump line for the 604 GHz far-infrared radiation is 9.5 μm). But in the longer wavelength range, the high absorption of BaF_2 makes it fragile to thermal shock. In fact, we broke quite a few BaF_2 windows when we tried to run at the 10.3μm CO_2 line, which is the pump line for the 419 GHz far-infrared laser radiation. As a solution, we replaced the BaF_2 window by a ZnSe window, which has a very low absorption coefficient in the range of 0.5-22μm; with the anti-reflection coating, those ZnSe windows are supposed to have a transmission coefficient bigger than 99% at 10μm wavelenth.[54]

3.3.2 Coupling antenna

At far-infrared frequencies, due to the short wave-length (submillimeter), the standard wave guide and resonance cavity techniques become awkward. Instead, integrated thin-film antennas have been used extensively. Among various types of thin-film antennas, dipole and bow-tie antennas are the most commonly used. The bow-tie antenna is a broadband device; its impedance is virtually frequency independent, which is an

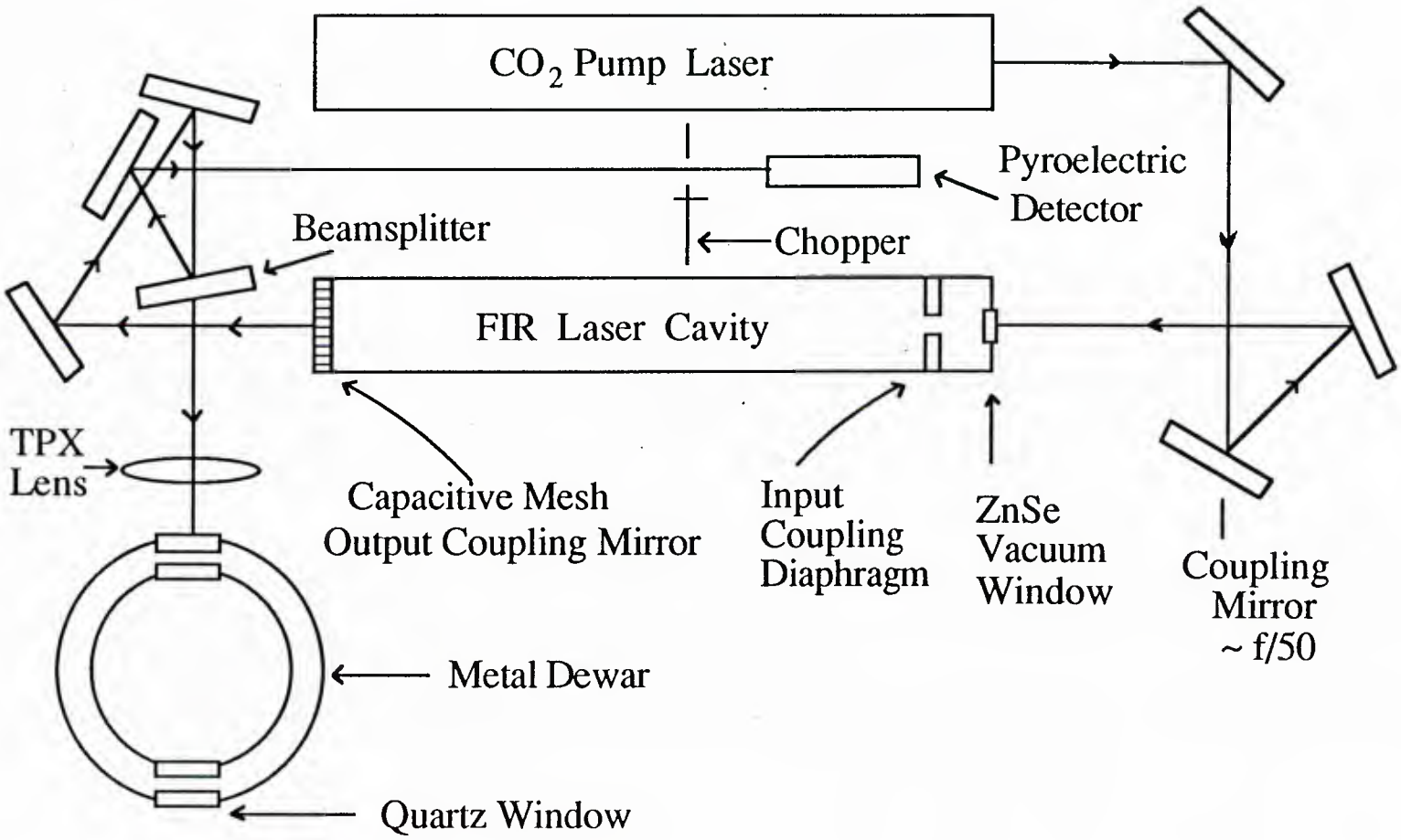

Fig. 3.4

Optically-pumped far-infrared laser set-up

attractive feature for coupling in a broad frequency range. We will discuss this in more detail in Chapter VI. The junctions studied in this report are attached to dipole antennas. In the following, we discuss the resonant frequency and resonance width of a dipole antenna with a finite width on a dielectric substrate.

By using an equivalent circuit depicted in Fig. 3.5,

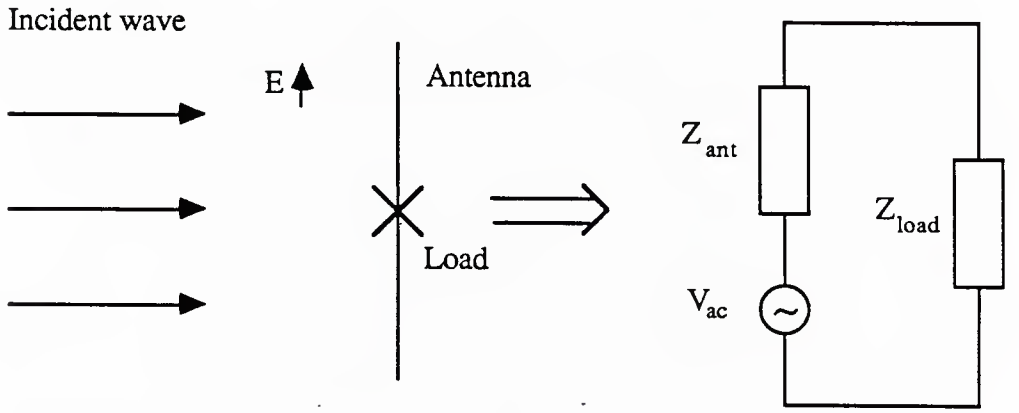

Fig. 3.5

Equivalent circuit of a dipole antenna.

we can treat the coupling dipole antenna as an ac voltage source with a finite impedance; the e.m.f. and the impedance of the source are functions of length and width of the antenna relative to the wavelength of the radiation source. The power dissipated in the load impedance is given by:

$$P = \frac{1}{2} |I|^2 \, \mathrm{Re}\,(Z_{load}) = \frac{1}{2} \frac{|E\, h_{eff}|^2}{|Z_{ant} + Z_{load}|^2} \mathrm{Re}\,(Z_{load}) \qquad (3.1)$$

where h_{eff} is the effective length of antenna. It is defined in such a way that the product of h_{eff} and the incident electric field E in the far space gives the source voltage V_{ac} across

$Z_{ant}+ Z_{load}$. Both h_{eff} and Z_{ant} are complicated functions of the length and width of the dipole antenna. In order to optimize the coupling, which is the power dissipated in the load, we have to optimize:

1) h_{eff}

2) $$\frac{\mathrm{Re}\,(Z_{load})}{|Z_{ant}+Z_{load}|^2}$$

1) Optimizing h_{eff}.

For a thin flat strip dipole antenna with a width *w*, it can be shown[55] that it is equivalent to a cylindrical antenna with a radius $a = w/4$. Then we can use all the numerically calculated results for a finite radius cylindrical antenna in reference 55. The parameter $\Omega=2\ln(L/a)$ characterizes the resonance width of antenna, where L is the full length of the dipole antenna concerned. As shown in Fig. 3.6(a), the peak of $|h_{eff}|$ for an infinite thin antenna ($\Omega=\infty$) takes place at $L = \lambda$.

In Fig. 3.6(a), as Ω decreases (the radius of the antenna increases), not only the resonance broadens, but also the resonance peak shifts in the $L<\lambda$ direction. This shift is caused by the finite-size effect: the thicker the cylindrical antenna is, the larger its capacitance is, thus the lower its resonant frequency is, which is equivalent to a smaller value of L/λ at resonance. In our case, the length and the width of the antenna are respectively

$$L = 180\ \mu m, \quad w = 4a = 10\ \mu m$$

which gives:

$$\Omega = 2 \ln (L/a) = 8.54$$

From the $\Omega = 10$ curve in Fig.3.6(a), we can see that the peak position takes place at $L\approx(2.5/\pi)\lambda=0.8\lambda$.

2) Optimizing $$\frac{\mathrm{Re}\,(Z_{load})}{|Z_{ant}+Z_{load}|^2}$$

In the general case, when Z_{load} can be varied, the product is maximum when

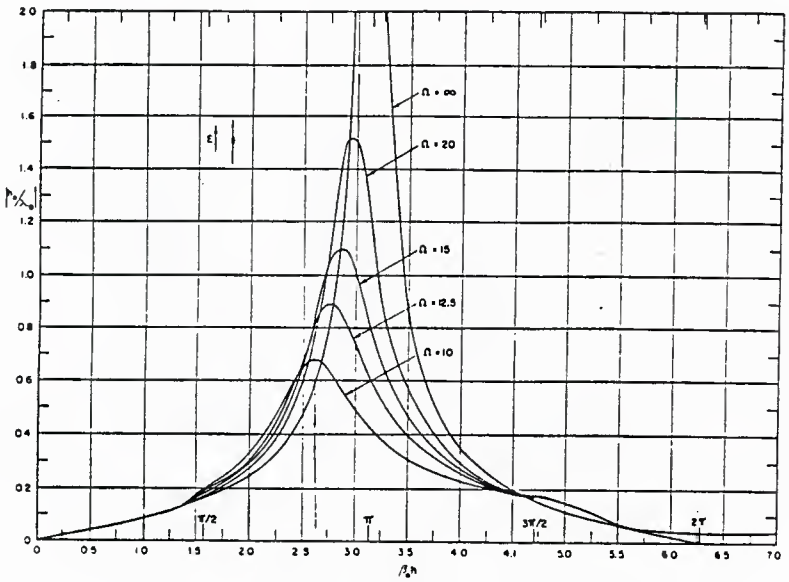

(a)

(b)

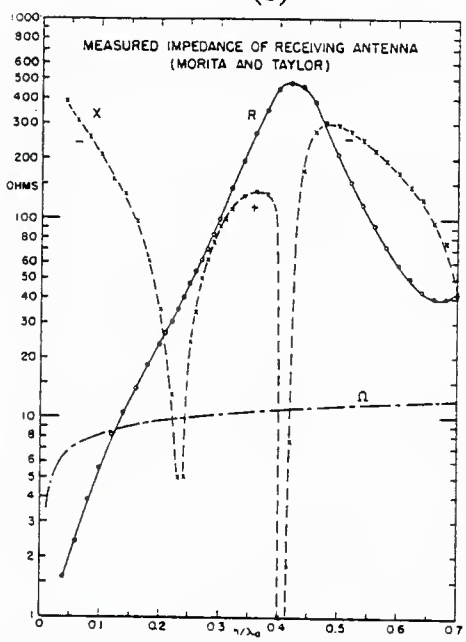

Fig. 3.6 (a) Effective length h_e of receiving antenna normalized to the wavelength λ_0 as a function of $\pi L/\lambda_0$ ($=\beta_0 h$ shown in the figure) with Ω=10, 12.5, 15, 20, ∞. (After Ref. 55) (b) Measured impedance of receiving antenna as function of $L/2\lambda_0$ ($=h/\lambda_0$ in the figure). The solid line is the real part of the impedance and the dashed line is the imaginary part. (After Ref. 55)

$$Z_{load} = Z_{ant}^{*}$$

But in our case, Z_{load} is fixed; also Z_{load} is the impedance of the parallel connection of R, C, and L (the nonlinear Josephson inductance), which is typically a few ohms for the SNAP junctions we have studied. This impedance is two orders of magnitude smaller than that of the lowest impedance of the antenna near any resonance. So the problem of optimizing $\{Re(Z_{load})/|Z_{ant}+Z_{load}|^2\}$ reduces to minimizing $|Z_{ant}|$. From Fig. 3.6(b), we can see that both the real and imaginary parts of the impedance of the antenna are very sensitive functions of the antenna length.One feature to be noticed is that the imaginary part is minimum at $L\approx\lambda/2$ and $L\approx\lambda$, these are the resonant wavelengths of the antenna. At these values, the antenna is purely resistive; when L/λ crosses these resonances, the reactance of the antenna changes from capacitive to inductive or vice versa, like that in a resonant LCR circuit. However, the variation of the real part R makes the overall performance of the antenna quite different at the half-wave resonance and the full-wave resonance. From Fig. 3.6(b), we can see that R is maximum at $L\approx\lambda$, the resonance at full wavelength is antiresonance[55] ($|Z_{ant}|$ is maximum); while the resonance at half wavelength is normal resonance.

To optimize the product

$$\frac{|E\,h_{eff}|^2}{|Z_{ant}+Z_{load}|^2} \approx \frac{|h_{eff}|^2}{|Z_{ant}|^2}|E|^2$$

we are facing the competition of h_{eff} being maximum at $L \approx \lambda$, and $|Z_{ant}|$ being minimum at $L\approx\lambda/2$. Fig. 3.7 is the plot of $|h_{eff}/Z_{ant}|^2$ vs. L/λ based on the numerical computed data from the reference (55); we can see that the changing of Z_{ant} dominates the changing of the product. The coupling of power to the load is maximum at about $L \approx \lambda/2$, $L=0.45\,\lambda$ to be precise for $\Omega=8.5$. Taking the substrate into account,[57] the resonant wavelength is increased from the value for an antenna isolated in vacuum by a factor α^{-1}; from Fig. 3.8, for $\varepsilon_r = 12$, which is the dielectric constant of Si substrate, the correction factor is

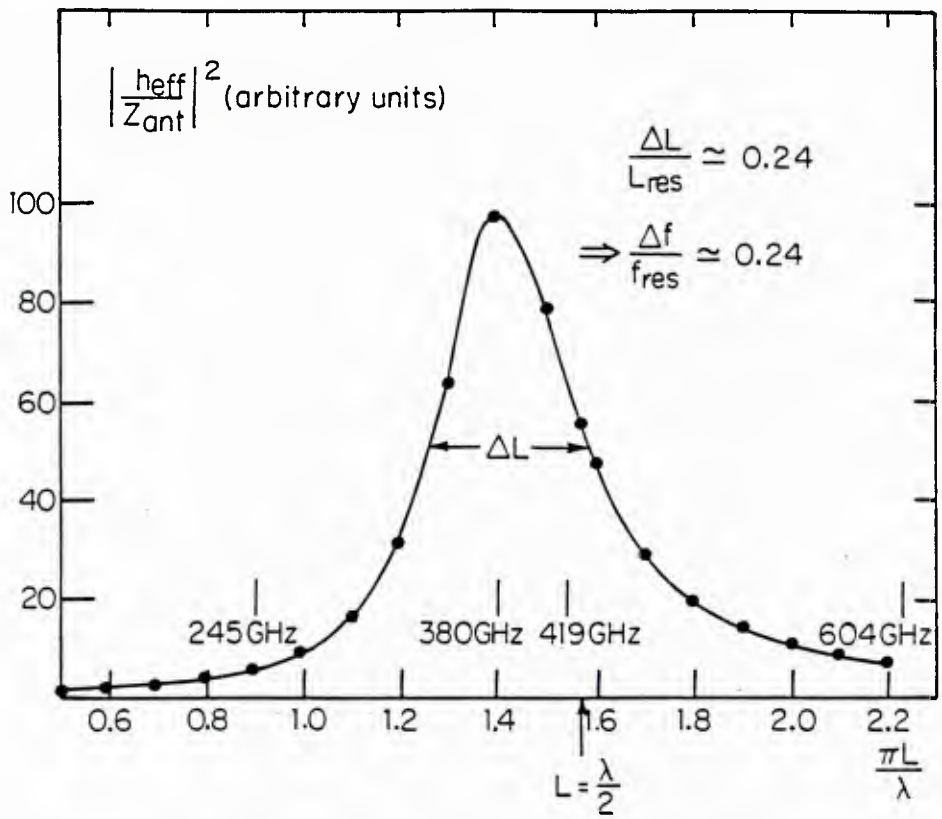

Fig. 3.7 Calculated results of the square of the effective length over the antenna impedance vs. $\pi L/\lambda$, with Ω=8.5. The calculation is based on the data of h_{eff} and Z_{ant} on page 736, "Waves and Antenna", King and Harrison, M.I.T. Press. Cambridge, Massachussets. After taking the dielectric constant of the substrate into account, the antenna resonates at 380 GHz, with a relative linewidth $\Delta f/f_{res} \approx 0.24$.

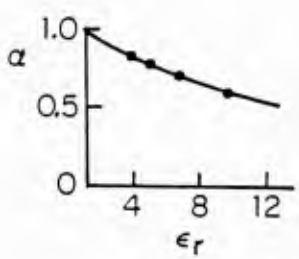

Fig. 3.8 Reduction factor α of resonant frequency vs. the relative dielectric constant of the substrate.

about 2, that means the resonant wavelength would be twice as large as whatever calculated for the antenna isolated in vacuum. Thus the resonant wavelength for our antenna is

$$\lambda_{res} \approx 2\,\frac{L}{0.45} = 2 \times \frac{180\,\mu m}{0.45} \approx 800\,\mu m$$

In other words, the resonant frequency is about $f_{res} \approx 380$ GHz. From Fig. 3.7, the fractional resonance width is about $(\Delta L/L_{res}) \approx 0.24 \approx 1/4$, so the resonant bandwidth is $(\Delta f/f_{res}) \approx 1/4$, or $\Delta f \approx \pm 50$ GHz.

3.4 Noise Reduction

3.4.1 Introduction

From the discussion in section 2.4, we know that due to its small characteristic energy $\hbar I_c/e$, a Josephson junction is subject to all kinds of noise, thermal or electrical. We can classify the noises concerned into two categories:

a) Intrinsic noises, including thermal, shot and quantum noise; these noises are always present at finite temperature, finite voltage and high frequencies. We cannot ignore them in any simulational and theoretical analysis of the experimental result. One of the major goals in this report is to study how these noises interact with a very sensitive nonlinear system. Fortunately, these noises mentioned above have been well studied, and the noise correlation function and power spectrum are known results; we can at least in principle predict the effect caused by these noises.

b) Extrinsic noise, including all the electromagnetic signals, random or non-random, sneaking into the experimental system, affecting the behavior of the Josephson junction studied. Several examples of such noises are: Electromagnetic radiation from a radio or TV station; low frequency electromagnetic fields caused by power lines; mechanical vibration coupled into the system through magnetic fields; the fluctuation of laser power, etc. All

these noises are unwanted noises. Their waveforms tend to be so complicated that a theoretical analysis is impossible. Our environment contains so much of these kinds of extrinsic noise, that they usually dominate the intrinsic noise unless the extrinsic noise is substantially reduced.

There has been a strong indication that there is a large amount of extrinsic noise present in our experimental system. For example, in 1983, Danchi et al.[42] analysed their data taken with and without laser radiation from the same set-up we have been using, but before the noise reduction was done. They found that they had to use noise equivalent to thermal noise at ~10K to make the simulation results fit to the experimental ones. This noise level is far above the thermal noise at the ambient temperature (1.4K), indicating there is some unknown noise in the system. More systematic studies on noise effects on a Josephson junction have been done in the same experimental set up later by the author. This study involved measuring the switching distributions as Fulton and Dunkelberger did[41]. The measurements were done on several Sn-SnO_x-Sn junctions with unfluctuated critical current typically about 1-10μA. The result of one series of measurements is shown in Fig.3.9. The unfluctuated critical current of the junction calculated from the $I_c R$ product is about 7μA; from the estimated value of the capacitance of the junction, C≈0.05pF, which is typical for this kind of junction[49], we have: $\hbar\omega_p/k_B \approx 5K$. Since the cross-over temperature of the escape rate between thermal activation and the MQT tunneling rate takes place at $\hbar\omega_p \geq 7k_BT$, where "=" holds only in the absence of dissipation[23], in the temperature range above 1.5K, we should not expect a strong MQT effect.

As we increase the temperature from 1.57K to 2.83K (the ambient temperature is increased successively from I to A), the peak of the distribution shifts in the direction of lower current. This is not surprising, since the unfluctuated critical current goes down as the temperature goes up, and the bigger noise at higher temperature tends to make the

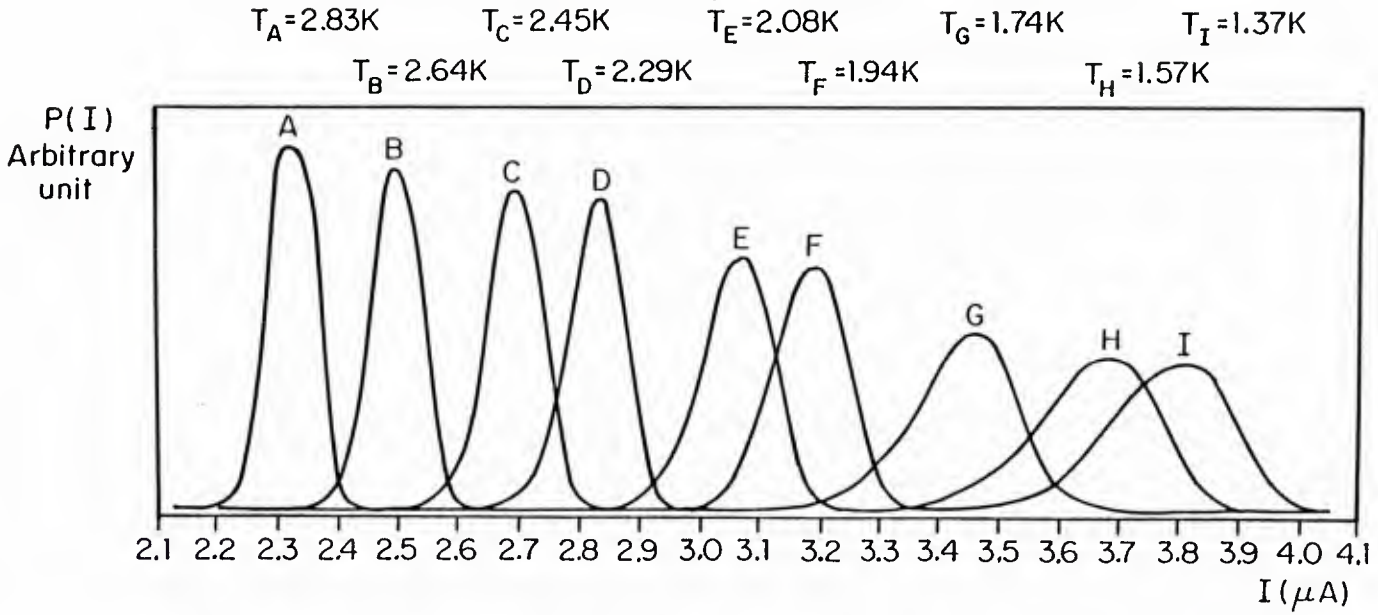

Fig. 3.9

Probabilities of switching distribution measured from a Sn-SnO_x-Sn junction in the temperature range of 1.37K-2.83K. The unfluctuated critical current is estimated to be 7μA from the I_cR_n product. As the temperature increases, from I to A, the measured critical current decreases (the peaks of the distribution shift to the low current end); the width of the distribution decreases too.

system switch to the non-zero voltage state at a smaller current. This combination of effects will decrease the measured critical current, making the whole distribution curve shift to the left. What is strange is that as the temperature goes up, the width of the distribution goes down, which is the opposite of what the thermal activation model predicts (cf. Fig. 2.10b). We are facing the dilemma: there are two parameters characterizing the distribution function, the position of the peak I_c^{exp} and the width of the distribution ΔI_c. If the switching is caused by purely thermal noise (or other noise having the same autocorrelation function as that of thermal noise), I_c^{exp} and ΔI_c will be related to each other in such a way that with one fitting parameter, the ambient temperature T, we can fit the theoretical curve to the experimental one. But in our case, the one fitting parameter thermal activation model will not work because if we choose T such that the theoretical I_c^{exp} fits with the experimental one, then the ΔI_c will not fit; the same thing will happen if we try to fit ΔI_c first.

This dilemma indicates that some kind of noise not characterized by the same correlation function as thermal noise is present in our system, which is hardly surprising. Given the fact that our environment contains so many electromagnetic signals, random or non-random, our system will be inevitably affected by them if we do not take special precaution.

3.4.2 Techniques of noise reduction.

This section is devoted to the problem how to avoid (or minimize) the extrinsic noise. We found that ref.(58) is an excellent guidance book in helping to achieve this goal.

The way a noise source affects a system can be understood in a very simple picture, Fig.3.10:

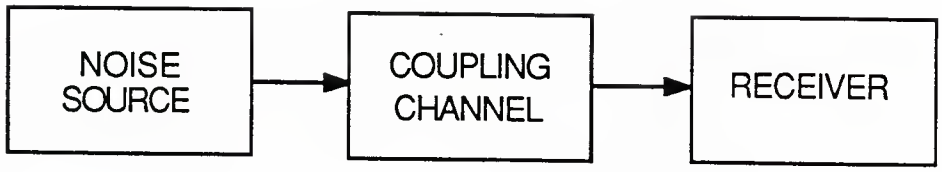

Fig. 3.10

Illustration of noise coupling into an experimental system.

The noise reduction can be achieved in three ways:

1) Remove the noise source-----moving noisy equipment to a place sufficiently far away that the noise source will not affect the system concerned. This is not practical in general. In our case, the signal measuring set-up must be physically close to some noisy equipment such as a CO_2 laser containing an electric discharge and the laser power supply. So we have to try to find a way to break the coupling at a later stage.

2) Shield the set-up completely from external electric and magnetic fields-----This can be done partially without too much difficulty by shielding the cryostat and the instruments. But from later discussion in this section we will see that no material can shield electromagnetic fields completely, unless we use a closed superconducting chamber, (which is impractical in our case since we have to allow FIR laser radiation to be coupled into the junction). Thus there is always some noise present inside the shield.

3) Reducing the pick up by the receiver-----This involves reducing the area of circuit loops; eliminating ground loops; filtering all the dc leads.

Since we can not do very much about the noise sources, the noise reduction work is focused on 2) and 3). These are discussed, in turn, below.

Shielding:

Shielding can be specified in terms of the degree of reduction in electric and/or

magnetic field strength caused by the shield. We define the shielding effectiveness factor S as:

$$S = 20 \log (E_1/E_1') \quad (dB) \qquad (3.2)$$

or

$$S = 20 \log (H_1/H_1') \quad (dB) \qquad (3.3)$$

where $E_1(H_1)$ are the incident fields, and $E_1'(H_1')$ are the transmitted fields as shown in Fig. 3.11.

Shielding effectiveness varies with frequency, geometry of shield, position within the shield where the field is measured, type of field being attenuated, direction of incidence and polarization. For simplicity, we will only discuss the shielding provided by a plane sheet of conducting material. The results of the plane sheet calculations are useful for estimating the shielding effectiveness of other geometries.

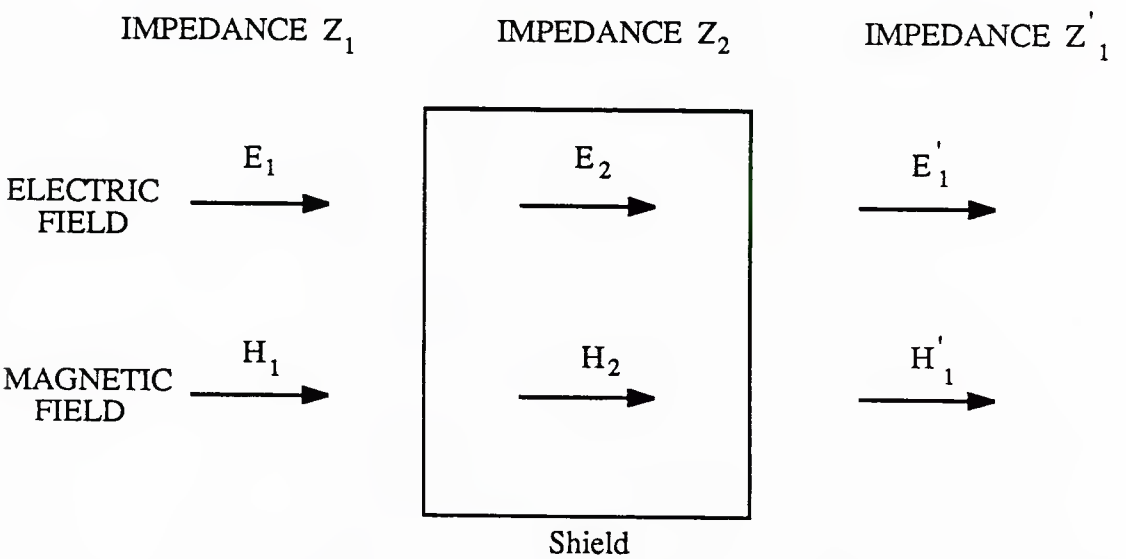

Fig. 3.11

Illustration of transmitted electric and magnetic fields through a plane sheet.

Apparently, two types of loss are encountered by an electromagnetic wave striking a metallic surface. a) The wave is partially reflected from the surface due to the impedance change at the interface; b) the transmitted portion is attenuated as it passes through the medium due to dissipation. The total shielding effectiveness of a sheet is equal to the sum of the absorption loss (A) plus the reflection loss (R) plus a correction factor (B) to account for multiple reflections in thin shields. Total shielding effectiveness can be written as:

$$S = A + R + B \tag{3.4}$$

The multiple reflection can be neglected if the absorption loss A is greater than 10 dB.

i) Absorption loss

When an electromagnetic wave passes through a conducting medium its amplitude decreases exponentially, i.e.

$$E_2 = E_0 e^{-t/\delta} \qquad H_2 = H_0 e^{-t/\delta} \tag{3.5}$$

where E_0 and H_0 are the fields at the boundary, t is the distance within the medium, and E_2 and H_2 are electric and magnetic fields measured at t respectively. The skin depth δ is given by

$$\delta = \sqrt{\frac{2}{\omega\mu\sigma}} \quad \text{meters} \tag{3.6}$$

If we use room-temperature copper as a reference material, we can express δ as

$$\delta = \frac{2.6}{\sqrt{f\mu_r\sigma_r}} \quad \text{inches} \tag{3.7}$$

where f is the frequency of the electromagnetic field in Hz. μ_r and σ_r are permeability and conductivity measured in units of μ and σ of copper. Table 3.1 gives the skin depths of the three most commonly used metals, copper, aluminum and steel.

Table 3.1

Frequency	δ For Copper (in.)	δ For Aluminum (in.)	δ For Steel (in.)
60 Hz	0.335	0.429	0.034
100 Hz	0.260	0.333	0.026
1 kHz	0.082	0.105	0.008
10 kHz	0.026	0.033	0.003
100 kHz	0.008	0.011	0.0008
1 MHz	0.003	0.003	0.0003
10 MHz	0.0008	0.001	0.00008

Table 3.1. Skin Depth of Various Materials. (Henry W. Ott "Noise Reduction Techniques in Electronic Systems". John Wiley & Sons, New York)

The absorption shielding factor A thus can be written as

$$A = 20\left[\frac{t}{\delta}\right]\log_{10}e = 8.69\left[\frac{t}{\delta}\right]\ \text{dB} \qquad (3.8)$$

Combining with (3.7), we have:

$$A = 3.34\, t\,\sqrt{f\,\mu_r\,\sigma_r}\ \text{dB} \qquad (3.9)$$

where t is in units of inches. For a 0.02 in.-thick Cu sheet, at 22 kHz, A=10dB; above this frequency, the absorption loss is already greater than 10 dB, so multiple reflection correction can be neglected for $f \geq 20$ kHz.

ii) Reflection loss.

For the geometry in Fig. 3.11, the transmitted E and H fields are:

$$E_2 = \frac{2Z_2}{Z_1 + Z_2}E_1$$
$$H_2 = \frac{2Z_1}{Z_1 + Z_2}H_1 \qquad (3.10)$$

where Z is the impedance of the electromagnetic wave defined as

$$Z = E / H \tag{3.11}$$

For a plane wave (far field) incident on a medium with (ε, μ, σ)

$$Z = \sqrt{\frac{j\omega\mu}{\sigma + j\omega\varepsilon}} \tag{3.12}$$

For insulators, $\sigma << \omega\varepsilon$.

$$Z = \sqrt{\frac{\mu}{\varepsilon}} \tag{3.13}$$

which reduces to the well-known result Z_o=377Ω in a free space, where

$$\mu = \mu_o = 4\pi\times10^{-7} \text{ H/m}$$

$$\varepsilon = \varepsilon_o = 8.85\times10^{-12} \text{ F/m}$$

For a conducting material, $\sigma >> \omega\varepsilon$; then

$$Z = \sqrt{\frac{j\omega\mu}{\sigma}} = \sqrt{\frac{\omega\mu}{2\sigma}}\,(1+j) \tag{3.14}$$

The amplitude of Z can be written as

$$|Z| = \sqrt{\frac{\omega\mu}{\sigma}} = 3.68\times10^{-7}\sqrt{\frac{\mu_r}{\sigma_r}}\sqrt{f}\ \Omega \tag{3.15}$$

where f is the frequency in Hz, μ_r and σ_r are the relative permeability and conductivity with respect to those of copper. Table 3.2 gives the impedances of the most commonly used metals, copper, aluminum and steel.

Table 3.2

Materials	Z(Ω)
Copper	$3.68\times10^{-7}\times f^{1/2}$
Aluminum	$4.71\times10^{-7}\times f^{1/2}$
Stainless Steel	$2.60\times10^{-6}\times f^{1/2}$

Table 3.2. The impedance values of Cu, Al and Fe.

The transmitted fields, if only subject to the reflection loss at the two interfaces (excluding the absorption loss and the multireflection correction) are:

$$E_1' = \frac{4 Z_1 Z_2}{(Z_1 + Z_2)^2} E_1$$
$$H_1' = \frac{4 Z_1 Z_2}{(Z_1 + Z_2)^2} H_1 \qquad (3.16)$$

In getting this result, we have assumed

$$Z_1 = Z_1'$$

Note that even though the electric and magnetic fields are reflected differently at each boundary, the net effect across both boundaries is the same for both fields. However, since the major reflections for E and H fields takes place at different boundaries, the multiple reflection correction factor B is quite different for each case. For E field, since most of its incident field is reflected at the first boundary, (cf. (3.10)), the multireflection of the remaining transmitted field will not affect the overall shielding significantly regardless of the attenuation. However, for H field, the transmitted field in the medium has the same order of magnitude as the incident field. If the attenuation loss does not reduce this transmitted field substantially, the multiple reflection will enhance the transmission through the whole sheet significantly.

If the shield is metallic and the surrounding area an insulator, then $Z_1 >> Z_2$, and

Eq. (3.16) reduces to

$$E_1' = \frac{4 Z_2}{Z_1} E_1$$
$$H_1' = \frac{4 Z_2}{Z_1} H_1 \qquad (3.17)$$

a) Shielding effectiveness for far-field. ($Z_1 = Z_o = 377\Omega$)

Combining (3.15) with (3.17), the reflection loss for a plane wave can be written

$$R = 20 \log \left| \frac{Z_1}{4 Z_2} \right| = 168 - 10 \log (\mu_r f / \sigma_r) \qquad \text{(dB)} \qquad (3.18)$$

Fig. 3.12 shows the combined shielding effects of absorption and reflection for a 0.020-in. thick copper shield for far-field electromagnetic fields. We can see that the shield is very effective (> 140 dB) for all the frequency range for the far field shielding. However, in the near field case ($r<\lambda/2\pi$) the situation is more complicated.

b) Shielding effectiveness for near-field.

If the field is produced by a short (compared to λ) rod or straight wire antenna, the source impedance is high. The wave impedance near the antenna---predominantly an electric field---is also high. As distance is increased, the E field decreases as $1/r^3$ while the H field decreases as $1/r^2$, the ratio E/H approaches from above to $Z_o=377\Omega$ at around $r=\lambda/2\pi$. While if the field is produced by a current loop antenna, the wave impedance near the antenna is low. As the distance is increased, E decreases as $1/r^2$ while H as $1/r^3$, the ratio E/H approaches Z_o from below at around $r=\lambda/2\pi$. In a laboratory environment, the strongest field is produced by the ac-power line, which generates both E and H field at 60 Hz and its higher harmonics. The corresponding wavelength λ is in the order of 10^4 km; thus all the experimental set-ups are exposed to such near-field perturbation. Since the impedances of the near electric and near magnetic field are quite different, the shielding effectiveness can be quite different for them.

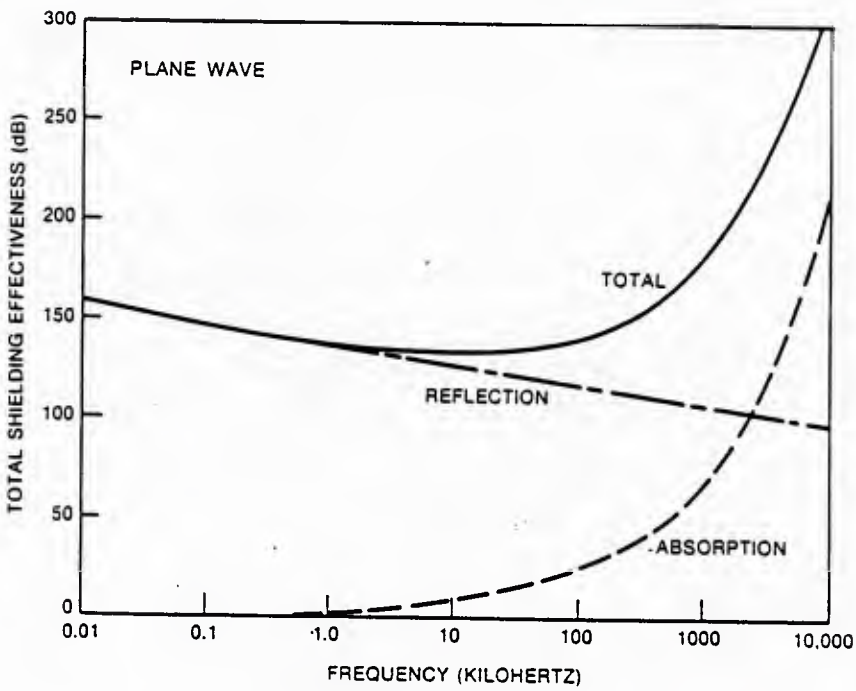

Fig. 3.12

Shielding effectiveness of a 0.02-in. thick copper shield in the far field. (After Ref. 58)

i) Near electric field.

For a near electric field, since its impedance $Z_e > Z_o$, from Eq. (3.10), the reflection loss at the first surface of the shield is bigger than that of a plane wave; thus the total shield effectiveness is greater than for a plane wave. With even a rather thin copper sheet (0.02-in.), we should have no trouble to obtain a 140 dB or better shielding.

Quantitatively, when $r < \lambda/2\pi$, the impedance of the near electric field of a point source is given by

$$Z_e = \frac{1}{2\pi f \varepsilon r} \tag{3.19}$$

if we insert (3.19) into equation (3.18), we obtain the reflection loss given by

$$R_e = 20 \log \frac{1}{8\pi f \varepsilon r |Z_2|} = 20 \log \frac{4.5\times10^9}{f r |Z_2|} \text{ dB} \tag{3.20}$$

With copper, $Z_2 \approx 10^{-7}\ \Omega$; if $r \approx 1$m, then $R_e \approx 180$ dB for f=10 MHz, above which the attenuation loss will dominate.

ii) Near magnetic field.

When $r < \lambda/2\pi$, the impedance of a near magnetic field of a point source is given by

$$Z_H = 2\pi f \mu r \tag{3.21}$$

For low frequencies ($f \sim 10$Hz), Z_H is not much bigger than the impedance of a metal sheet. The reflection loss shielding is not too effective. Combining (3.21) with (3.18), we have the reflection loss for near-magnetic field:

$$R = 20 \log \frac{2\pi f \mu r}{4 |Z_2|} = 20 \log \frac{1.97\times10^{-6} f r}{|Z_2|} \text{ dB} \tag{3.22*}$$

---

* If a negative value is obtained in the solution for R, use R=0 instead and neglect the multiple reflection factor B. The error occurs because the assumption $Z_1 >> Z_2$ is not satisfied.

For a copper shield, if f ≈ 10Hz, and r ≈ 1m, then R ≈ 20 dB, which is not a very effective shield.

In addition to this ineffective reflection loss shielding, the multiple-reflection enhanced transmission will make the shielding of near magnetic field even worse. Since $Z_2 \approx Z_1$, from (3.10), we know that most of the incident magnetic field will penetrate into the shielding media. Although a major part of this field will be reflected by the second surface, as long as the thickness t is small compared to the skin depth δ (which is the case at low frequency, since $\delta \propto \omega^{-1/2}$), this reflected field will again be partially reflected back by the first surface. This process will go on and on until the field is sufficiently attenuated. This multiple reflection will reduce the shielding effectiveness by the correction factor B, which can be calculated to be

$$B = 20 \log (1 - e^{-2t/\delta}) \quad dB \qquad (3.23)$$

One way to decrease this multiple reflection is to use magnetic material such as μ metal. It increases the absorption loss, since the permeability increases more than the conductivity decreases for most magnetic materials. However, even though μ metal is much better than copper for low frequency magnetic shielding, it is not nearly as effective as a copper shield for near electric field or plane wave. Thus we should keep in mind that no matter how much shielding we have, we always have some low frequency magnetic field present in our system. Reducing the effect of such fields has to be done by carefully reducing loop area and grounding, which will be discussed in the following section.

Reducing noise pick up.

Although we always have some low-frequency magnetic field present in our system, by careful wiring and grounding, we can reduce the influence of such field by a substantial amount. The effect of wiring and grounding can be best understood from the testing result[58] shown in Fig.3.13 and Fig. 3.14. The test is done in a configuration that

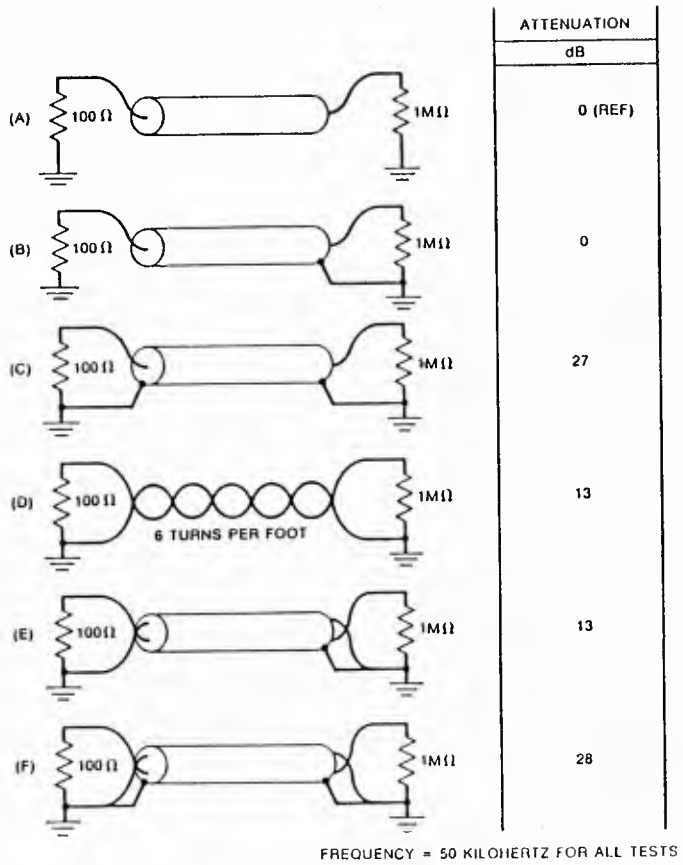

Fig. 3.13 Results of inductive coupling experiment; all circuits are grounded at both ends. (After Ref. 58)

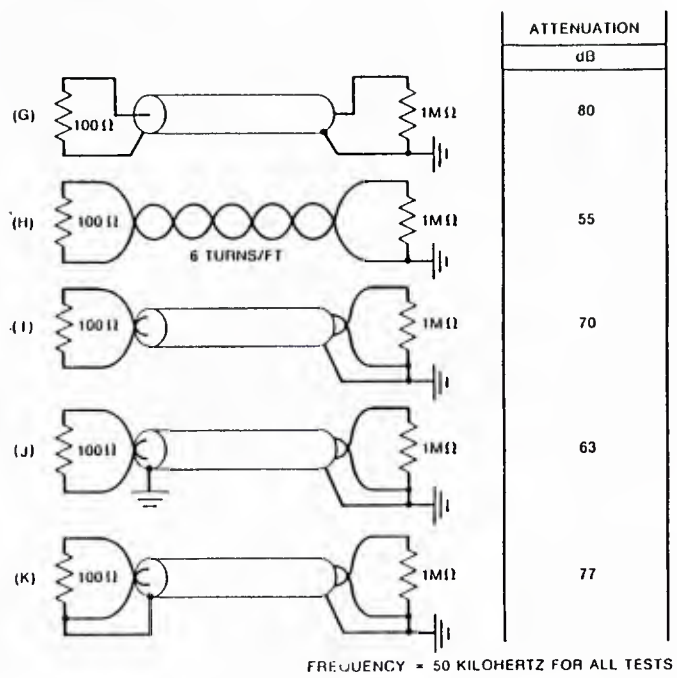

Fig. 3.14 Results of inductive coupling experiment; all circuits are grounded at only one end. (After Ref. 58)

the wire to be tested is inductively coupled to a 50 kHz ac source; the pick-up voltage from the wire is measured across the 1MΩ resistor.

All the configurations in Fig.3.13 have a ground loop, which effectively increases the loop area by a substantial amount. In this case, twisting and shielding wires do not yield much improvement in attenuation. The configurations in Fig.3.14 do not have this problem, and showed a large improvement.

Configuration (I) is the best for low frequency magnetic shielding, i.e. a shielded twisted pair with only one end of the shield grounded is what we want for a low noise set-up. That is because, (I) does not have the drawback as (G) and (K), which either has the shield as a signal wire, (G), or has the shield connected to a signal wire at both ends,(K); so that any noise current flowing through the shield might affect the signal. It is always better to connect the shield and signal conductors together at just one point. That point should be such that the noise current from the shield does not have to flow down the signal conductor to get to the ground. On the other hand, no grounding at all will provide no protection against electric field. The indicated lower attenuation of (I) compared to (G) can be improved by more turns/length (6 turns/ft was used in this test, which is a very coarse twisting).

We chose to ground the amplifier end of the cable shields. The configuration of our experimental set-up is shown in Fig. 3.16. The metallic dewar is floated electrically from the laser table, which is a very noisy ground. As discussed before, this metal dewar should provide very good shielding against far-field electromagnetic fields and near electric field. The major noise inside the dewar is near magnetic field noise. To minimize the pick-up of this noise, all the signal leads are made of twisted pair with ~10 turns/in. The current leads and voltage leads run down through separate metal tubes; this reduces the interference between the current and voltage signal. This is especially useful when we deliberately put some ac or noise signal down through the current leads and measure the

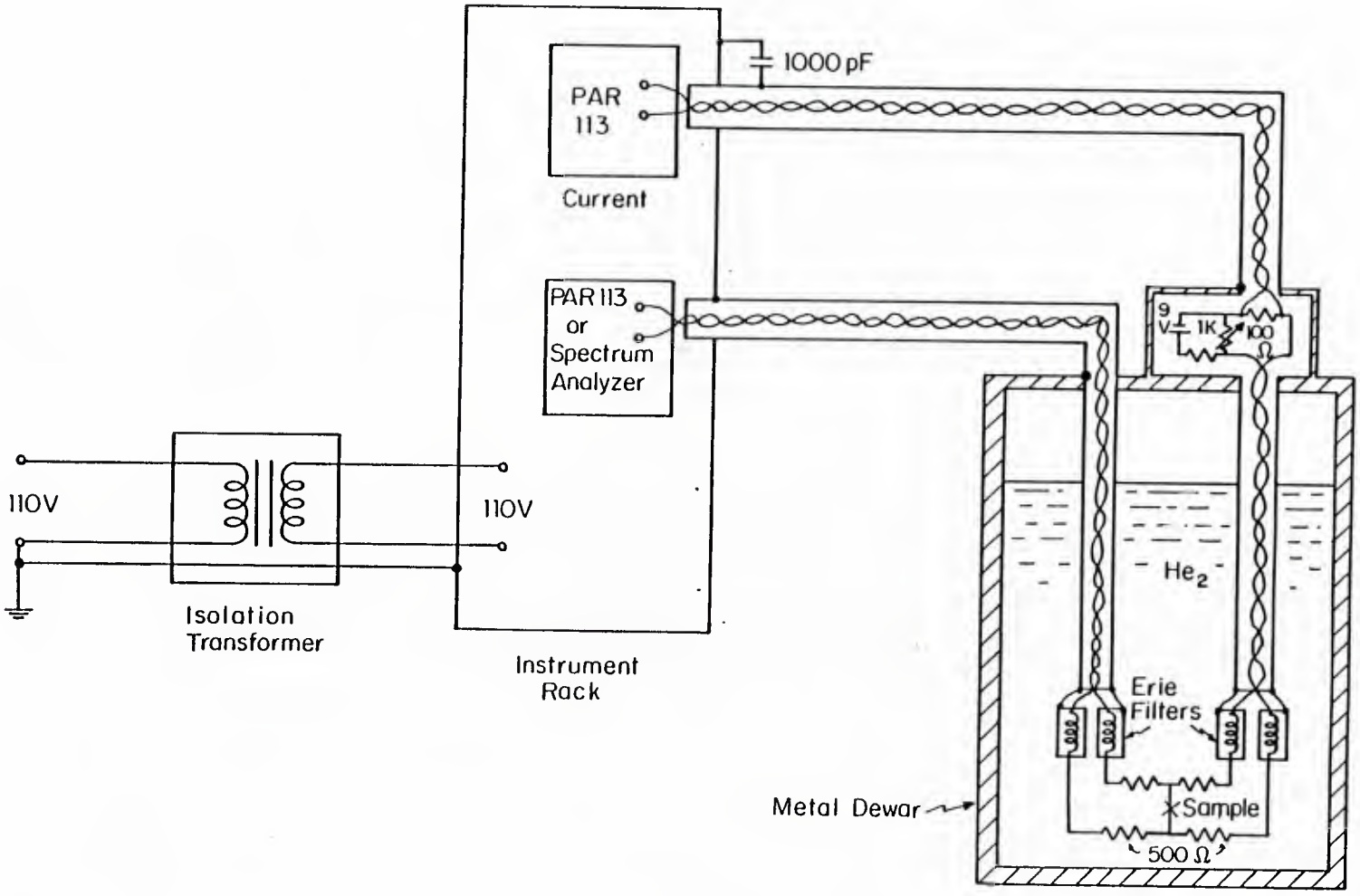

Fig. 3.15

Experimental set-up

voltage response from the junction. The leads are filtered through low temperature π filters (Erie filters) before connecting to the sample; these filters should be sufficient to cut down the noise in the frequency range above 1MHz flowing from the room temperature end of the leads. All the loop areas are minimized.

Outside the dewar, all the leads are shielded twisted pair, with only one end electrically connected to the chassis of the amplifier (PAR 113 or Spectrum Analyzer), which in turn is connected to the ground of the ac power line. (Other grounding points have been tested, such as a waterpipe, which shows no difference from the present configuration). The shield of the current measurement cable is only ac electrically connected to the chassis (through the 1000 pF capacitor). By doing this, we broke the ground loop between the current and the voltage cable shields at low frequencies (at ~1kHz, $1/\omega C \sim 1M\Omega$), but at high frequencies (when f>1GHz, $1/\omega C < 1\Omega$), we effectively have a multipoint ground system to minimize the ground impedance. (As a rule of thumb, a system with a physical dimension greater than one-twentieth of the wavelength concerned should have a multipoint ground.[58]) An isolation transformer is used to break the potential ground loop between the neutral power line and the ground. (As required by the National Electrical Code, the two are connected at the main service entrance, which is perhaps the basement of the building.) Complete disconnection with the power line is impractical in our case, since we have to use some ac-powered apparatus such as an oscilloscope or a X-Y recorder to monitor the experiment.

This configuration proved quite effective in reducing noise pick-up. Even though the whole set-up is not in a screened room (it is in the same room with a noisy laser source plus several mechanical pumps.), the noise pick-up is below the instrumental sensitivity. Fig. 3.16(a) shows the power spectrum taken from a 1kΩ resistor connected in exactly the same way as our sample is supposed to be. From 10 Hz to 100 kHz, there is no observable noise above the instrumental background noise, which is ~-150 dBV (relative

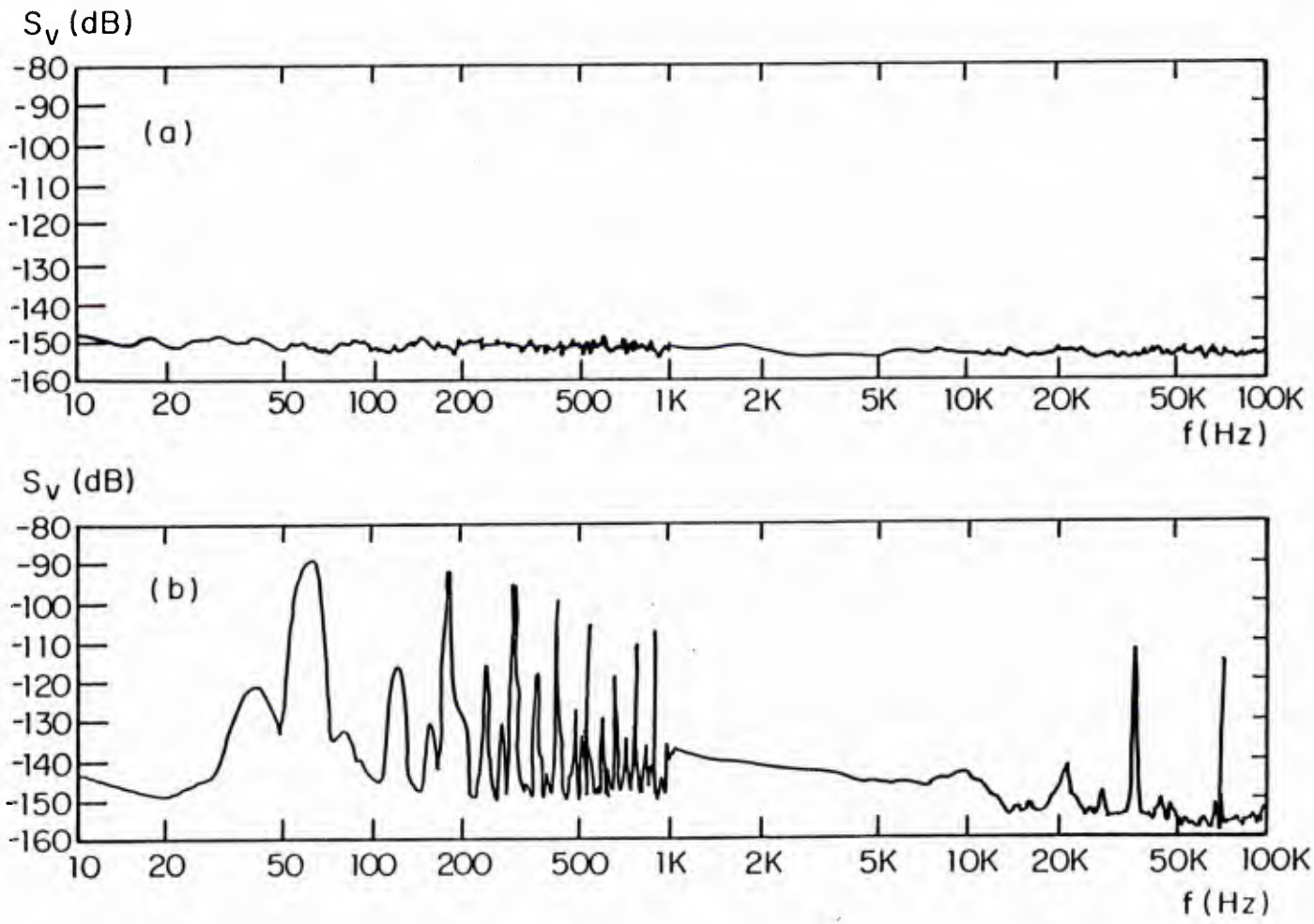

Fig. 3.16 Power spectra measured from a 1kΩ resistor connected at the position of the "sample" in Fig. 3.15. (a) From the present set-up (Fig. 3.15). (b) From the previous set-up, in which no special care was taken to minimize noise pick-up.

to $1V^2/Hz$); even the seemingly ubiqitous 60 Hz noise is not detectable. This is certainly a great improvement from the experimental set-up when we took the data shown in Fig. 3.9. The power spectrum taken from that set-up is shown in Fig. 3.16(b). It shows a large amount of low frequency noise, mainly 60 Hz and its harmonics. It is not surprising to see some behavior not explainable by the thermal activation model, because there are all kinds of low frequency noise in the system, which will inevitably affect the switching behavior of the junction.

As a quick check, we measured the power spectrum from a Josephson junction to see if there is any obvious sign of extraneous noise in the system. Fig. 3.17 shows the power spectrum measured from a SNAP junction at room temperature. The junction is dc biased at 1.75mA. According to Rogers and Buhrman[58], the resistance fluctuations due to the filling and emptying of localized electron states in the tunneling barrier should give rise to a voltage power spectrum composed of several Lorentzian spectra. At room temperature, the superposition of the numerous Lorentzian power spectra forms an essentially 1/f noise spectrum. That is what we have seen in Fig. 3.17. The power spectrum is clean and structureless; it has a precise 1/f envelope, extending over five decades in frequency. The power density at the high-frequency end, -150 dBV, is close to the instrumental sensitivity. Clearly, with the old experimental set-up, (cf. Fig. 3.16(b)), the low-frequency power spectrum would be dominated by the 60 Hz and its harmonics.

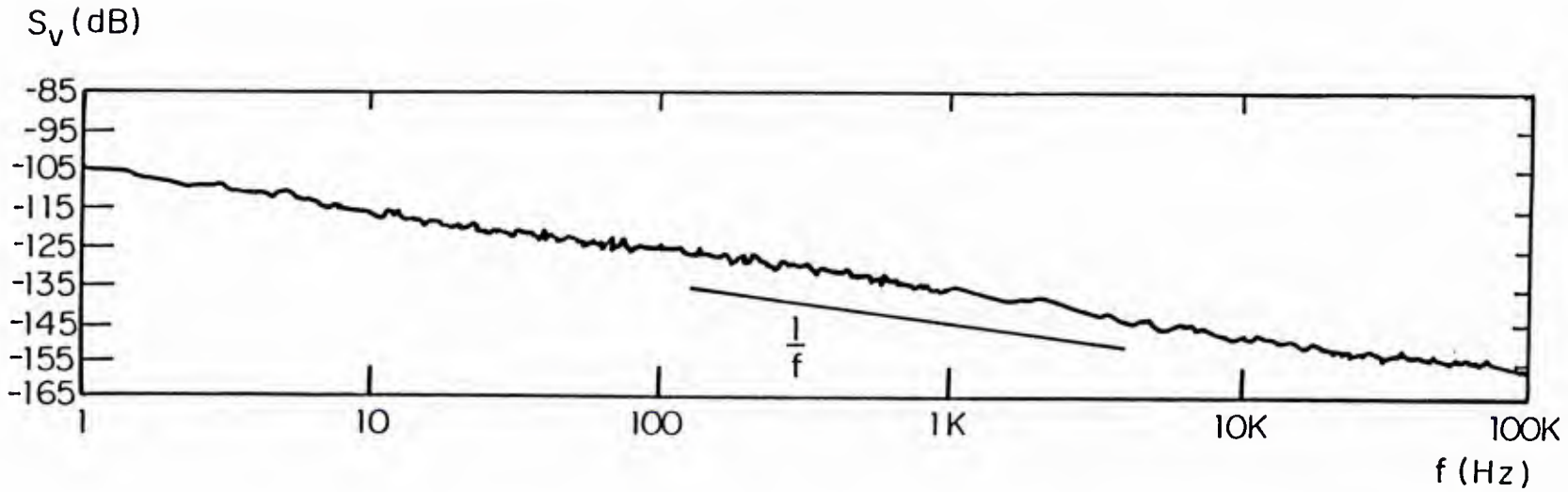

Fig. 3.17

Power spectrum measured from a SNAP junction at room temperature. The junction was biased at 1.75mA. The spectrum shows a clean and structureless 1/f form over five frequency decades.

CHAPTER IV

ANALOG SIMULATIONS

4.1 Introduction

As discussed earlier (in Chapter I), it is impossible to monitor the phase motion of a Josephson junction because of its high frequency nature. To study the response of a Josephson junction beyond some time-averaged characteristics such as the step width vs. laser power, we have to appeal to simulations.

Digital simulations have certain advantages: 1) Being very accurate, all the parameters can be controlled to an accuracy many orders of magnitude beyond the experimental ones. 2) Flexibility. It allows us to insert whatever types of noise we want, such as voltage-dependent shot noise and frequency-dependent zero-point fluctuation. Also, it can accomodate a complicated nonlinear quasiparticle I-V characteristic. 3) All the results are computed and stored digitally, allowing them to be analyzed in detail by computers. However, despite its advantages, digital simulation is seriously limited by the computing speed. Even though the computing power of today's computers is enormous, it takes typically many hours to produce a simulated I-V curve. It is very difficult and tedious to explore a large region in parameter space, which is what we usually have to do because of the large uncertainty in experimental parameters.

Analog simulation can close this gap between the experimental study of a real Josephson junction and digital simulations. An electronic analog has an advantage in demonstrating qualitative behavior quickly over a wide range of parameters and can usually have quantitative results to a precision of a few percent. It is fast enough that we can take I-V curves at the same speed as in an experiment; also it is slow enough ($\sim 10^4$ Hz typically) that we can study the phase motion and frequency spectrum with conventional

instruments.

Based on the RCSJ model, there have been a few electronic Josephson analogs invented.[60-62] We have compared the performances of the two most commonly used ones, the Henry & Prober design[61] and the Magerlein design.[62]

1) Henry & Prober design

It uses a VCO (Voltage-Controlled-Oscillator) to generate a pulse sequence whose frequency ω_{VCO} is proportional to the applied voltage, i.e. $\omega_{VCO} = aV + b$. These pulses are used to control a sample-hold circuit, whose input is from an external sine-wave generator with a frequency ω_{sig}. The output of this sample-hold circuit is a staircase-like sine wave, whose frequency ω is adjusted in such a way that

$$\omega = \omega_{VCO} - \omega_{sig} = aV \tag{4.1}$$

We can define a phase ϕ such that

$$\frac{d\phi}{dt} = \omega \tag{4.2}$$

Thus we have an electronic circuit whose output satisfies the two Josephson relations:

$$I_s = I_c \sin \phi \tag{4.3a}$$

$$\frac{d\phi}{dt} = aV \tag{4.3b}$$

This circuit is quite simple compared to most of the others in Ref.60-62. It gives reasonably good results. The main drawbacks of this circuit are:

i) It is a relatively slow device. If we do not want the staircase too coarse, we have to be limited to

$$\frac{\omega}{\omega_{VCO}} = \frac{\omega_{VCO} - \omega_{sig}}{\omega_{VCO}} \approx 0.01$$

With the commonly used eclectronic components, we can get the circuit working pretty

well at $\omega_{VCO}/2\pi \approx 100$kHz, or $\omega/2\pi \approx 1$kHz; above that we might have difficulty.

ii) The device is not stable. Since it requires an external signal generator, it is very hard to maintain the external signal generator and the VCO in phase because of the drift of electronic devices. In our experience, even after half an hour warm-up, there is still noticeable drift between the two devices.

2) Magerlein design

This analog does not have the problems above. It is a faster device, (10-100 kHz); it does not require an external sine-wave generator, there is no problem of stabilities. In addition, the sinϕ generator generates a waveform much better than a staircase-like sine wave. Given all these advantages compared to the other model, even though the circuit is much more complicated than that of Henry & Prober, we still prefer it. This chapter will discuss the principle of operation and the performance of a Magerlein simulator. We will also compare the simulation results with some experimental ones.

4.2 Analog circuit for Magerlein design simulator.

4.2.1 The principle of operation.

To make a Josephson junction analog, the key part is to generate some current which is a sine function of the integral of the input voltage; i.e. we need to generate

$$I_s = I_c \sin\phi$$
$$\phi = \frac{2e}{\hbar}\int_0^t V\,dt \qquad (4.4)$$

There is no problem to build an integration circuit to generate a voltage which is the integral of the input voltage. But if the input voltage is a dc voltage, this integration will soon reach the limit voltage of the circuit and saturate it. To avoid this problem, we realize that we are not interested in ϕ itself but sinϕ, which is a periodic function of ϕ. Thus we

can generate a voltage proportional to ϕ or $(\pi - \phi)$ in the range $\phi = (-\pi/2, 3\pi/2)$, and extend the voltage periodically beyond this range.

In Magerlein's design, we generate a voltage V_ϕ such that

$$\frac{\pi}{2}\frac{V_\phi}{V_{max}} = \begin{cases} \phi & -\pi/2 < \phi < \pi/2 \\ \pi - \phi & \pi/2 < \phi < 3\pi/2 \end{cases} \qquad (4.5)$$

$$V_{\phi + 2n\pi} = V_\phi$$

where

$$\phi = 2\pi k \int_0^t V \, dt$$

k is a constant determined by the threshold voltage V_{max} and the RC constant of the integrator. V_{max} is some preset voltage; when $| V_\phi |$ exceeds it, the integration circuit will reverse its polarity. By using the trigonometric relation

$$\sin \phi = \sin (\pi - \phi) \qquad (4.6)$$

we have

$$\sin \left[\frac{\pi}{2}\frac{V_\phi}{V_{max}}\right] = \sin \phi \qquad (4.7)$$

Thus if we use a sine converter to generate the sine of $[(\pi/2)\, V_\phi/V_{max}]$ and then convert it into current, we have a current satisfying equation (4.4). This procedure can be understood easily with the illustration of Fig. 4.1.

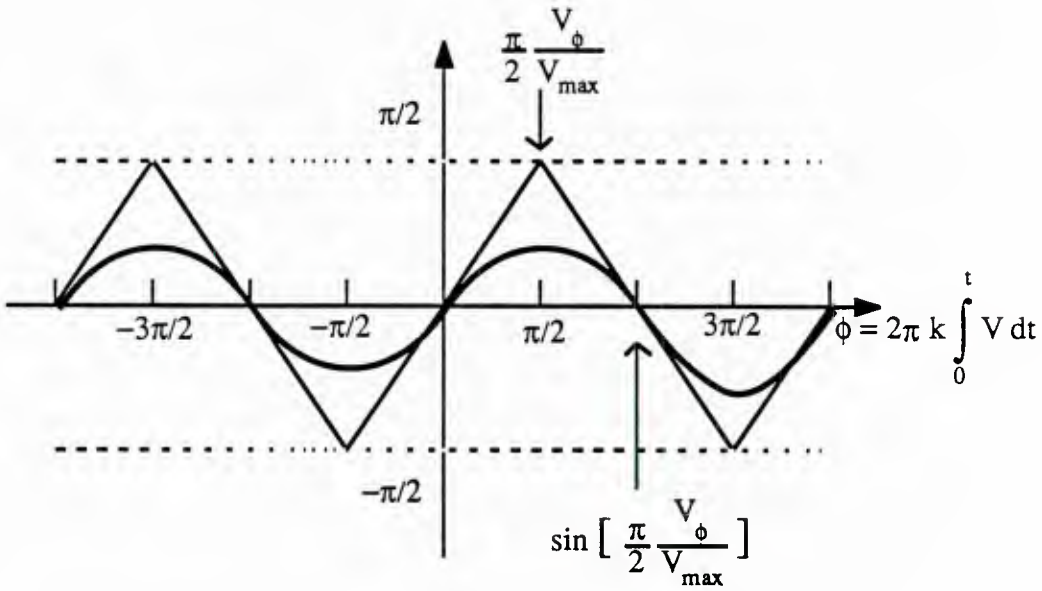

Fig. 4.1

Illustration of the principle of function of Magerlein's simulator.

First we generate a voltage which is a periodic function of ϕ with a period 2π; the function form is a triangle wave. Next, we use a sine converter to convert this triangle wave into a sine wave. Note, when we talk about wave, we mean in ϕ space instead of the time domain; when the input voltage is dc, $\phi \propto t$, and the waveform in the time domain is also sinusoidal. But the result (4.7) is obtained without any assumption on the time dependence of V; it is valid for any time-dependent V.

Fig. 4.2 shows a block diagram of this circuit.

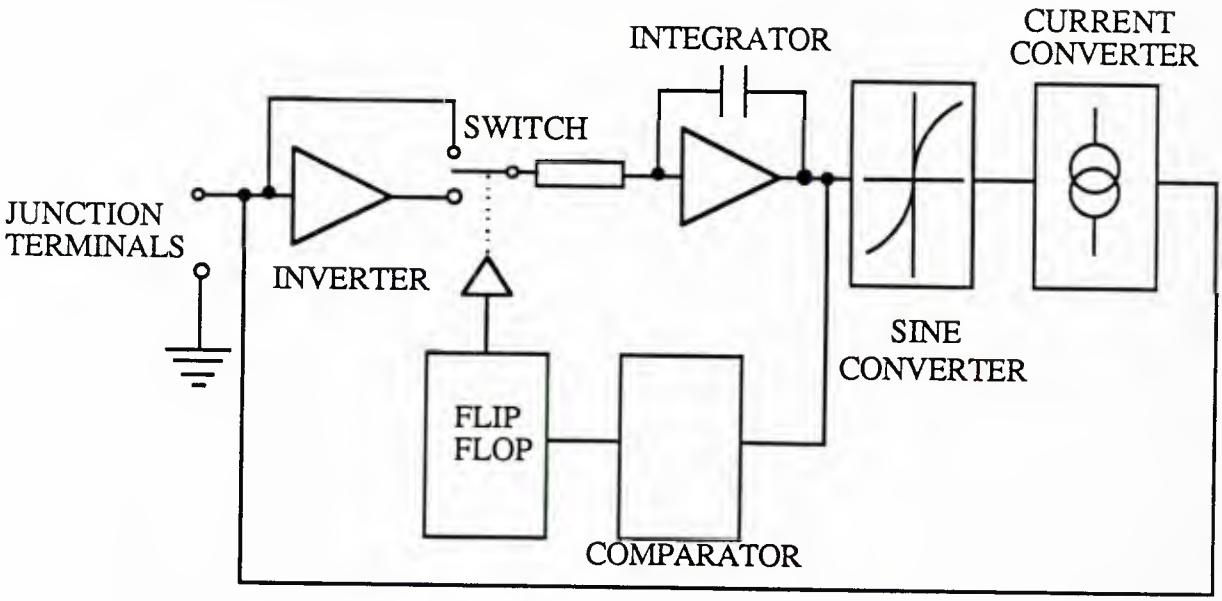

Fig. 4.2

Block diagram of Magerlein's analog simulator.

The input voltage V (or -V, depending on the initial position of the electronic switch) is integrated through the integrator, the output voltage of the integrator is constantly compared with the two limiting voltages ($-V_{max}$, V_{max}) of the window comparator. When the integration voltage goes beyond ($-V_{max}$,V_{max}), the comparator will send a pulse to the flip-flop and change its output state; this will change the switch position and reverse the input polarity of the integrator. Now -V (or V) will be integrated in this half cycle until the limit ($-V_{max}$, V_{max}) is reached. This process generates V_{ϕ}. The next step is using a sine-converter. In our case, this is a differential amplifier with its saturation set at $\approx V_{max}$; the gain of the amplifier reduces at around V_{max} , so that this nonlinear amplifier makes the otherwise sharp cusp of a triangle wave rounded. With proper adjustment, this sine-converter should make a very good sine wave out of a triangle one; the best minimized distortion can be 40 dB below the fundamental, or 1%.

To convert the voltage V_ϕ into a current is a fairly easy thing to do, which can be accomplished with one op-amp.

Fig. 4.3 is the schematic of the circuit we made at Harvard. The components are quite different from Magerlein's original design. That is due to the author's preference for some components plus the convenience of obtaining them. The circuit works as follows:

The input voltage V(t) is fed in through a buffer 356, then inverted in polarity by an inverter. V(t) and -V(t) are then sent into two analog switches composed of 1/2(4066). The two switches are controlled by two signals with opposite logic levels; i.e. one with high level and the other with low level, so that only one switch is conducting at any moment. This alternating switched voltage is integrated by an integrator whose output is fed into a window comparator whose window limit is set to be (-2V, +2V). Whenever the voltage from the integrator exceeds these limits, the comparator will send a negative transient voltage to the J-K flip-flop 74107 and invert its output state. (The normal output state of the comparator is high, which is enforced by the 2K pull-up resistor connected to the output of the comparator.) Thus the previously open switch in 1/2(4066) will be closed now and the previously closed one will be open. This will reverse the input polarity of the integrator which starts integrating the signal with the same amplitude but opposite polarity from the previous one. This process will go on and on. If the input voltage is dc, we will generate a triangle wave whose period is determined by the RC constant of the integrator and the ratio of the input voltage V to V_{max}.

If we do not take special precaution the circuit quite often locks up, especially at high frequency or large ac driving amplitude. To guarantee that the circuit will oscillate, it is necessary to have the speed-up 10 pF capacitor in the window comparator and the pull-down 10K resistor connected to the inverse input terminal of the integrator. The 10 pF capacitor composes a positive feedback loop, which speeds up the transition speed of the comparator. The function of the 10K resistor is such that, when the voltage V_ϕ from the

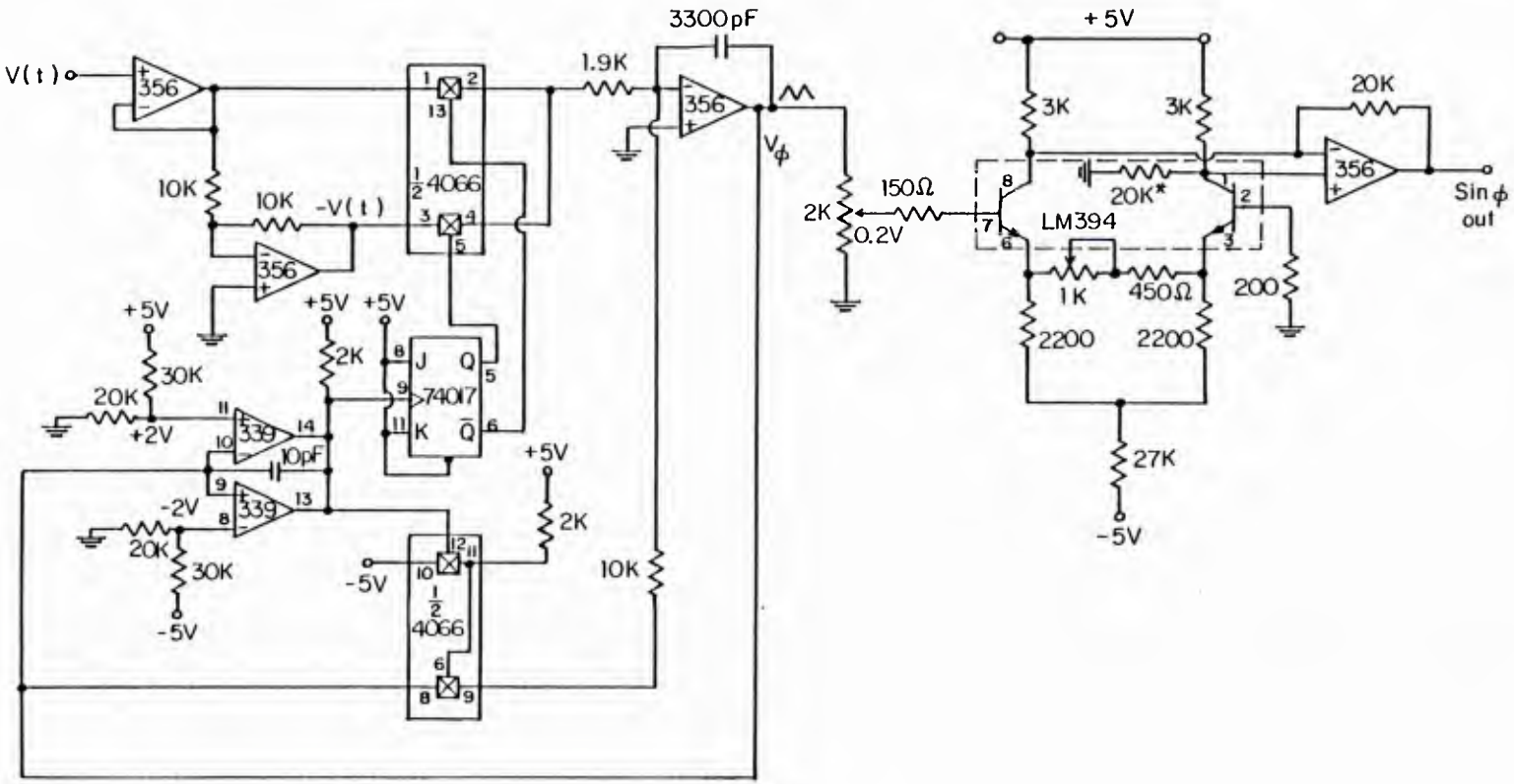

Fig. 4.3

Circuit diagram of sinϕ generator.

integrator exceeds ($-V_{max}$, V_{max}), the switch (terminals 8 & 9 of the 4066) will be closed, and the voltage across the integrator capacitor will be discharged through this 10K resistor, which will bring V_ϕ back into the interval ($-V_{max}$, V_{max}). The output of the comparator then will go back to the normal high position and the comparator is ready for the next transition. This resistor proved to be crucial to the function of the circuit; its value is determined by the trade off of the pull-down effectiveness and the distortion it introduces. The value 10K is found to guarantee the oscillation at all the conditions we have studied, and the distortion on an otherwise perfect triangle wave is barely noticeable. (If the resistor is too large, it will have little pull-down effect; if too small, it will distort the wave form tremendously.) The output of the integrator is the V_ϕ we discussed before, a fraction of which is sent into a variable-gain amplifier. By carefully adjusting the input level controller (2K pot) and the gain controller of the amplifier (1K pot of the amplifier), we can make the amplifier work in such a nonlinear region that the output from a triangle wave input will be very much like a sine wave. The distortion can be as small as 1% (40 dB), which is comparable to some commercial models of sine generator and good enough for most of the Josephson effect studies.

As mentioned before, the limit voltage V_{max} and the RC constant of the integrator determine the oscillation frequency for unit input voltage. For a dc input voltage V, the slope of the integrated voltage V_ϕ is

$$\left| \frac{dV_\phi}{dt} \right| = \frac{V}{RC}$$

It is clear that in the time interval (0, T/4), where T is the period,

$$V_\phi = \frac{V}{RC} t$$

rises to the value:

$$V_{max} = \frac{V}{RC}\frac{T}{4}$$

or
$$f = \frac{V}{4RCV_{max}} = k^{sim} V \qquad (4.10)$$

This has the same form as the Josephson relation

$$f = \frac{1}{2\pi}\frac{d\phi}{dt} = \frac{2eV}{2\pi\hbar} = k^{exp} V \qquad (4.11)$$

(Note: Do not forget the factor (2π) in this formula!)

In the simulator, we chose the values of V_{max} and RC such that shown in Fig.4.3: V_{max}=2V, R=1.9K, C=3300pF, so that:

$$k^{sim} = \frac{20\ kHz}{V} \qquad (4.12)$$

while

$$k^{exp} = 4.83\times10^{14}\ \frac{Hz}{V} \qquad (4.13)$$

Clearly, a real Josephson junction is a much faster oscillator compared to a simulator if we operate at the same voltage. The measured value of k^{sim} differs from the predicted one in (4.12) by a few per cent due to the precision limit of the electronic components such as R and C. This precision of k^{sim} is good enough for most of our purposes as long as we measure ω_p and β_c accurately.

The output of this sinϕ generator is converted into current through the variable resistor *r* (Fig.4.4a), and then connected to a resistor R(V) and a capacitor C in parallel, completing the circuit of the RCSJ analog.

To approximate the nonlinear structure of the quasiparticle I-V characteristic at the gap, we build in a voltage-dependent piece-wise nonlinear resistor. (Fig. 4.4b) It uses a window comparator similar to that in Fig. 4.3; this comparator controls two analog switches. When $|V(t)| \geq V_g$, the switch connecting R_n conducts; while when $|V(t)| < V_g$, the switch connecting R_{leak} conducts. Here V_g is the preset gap voltage, which is

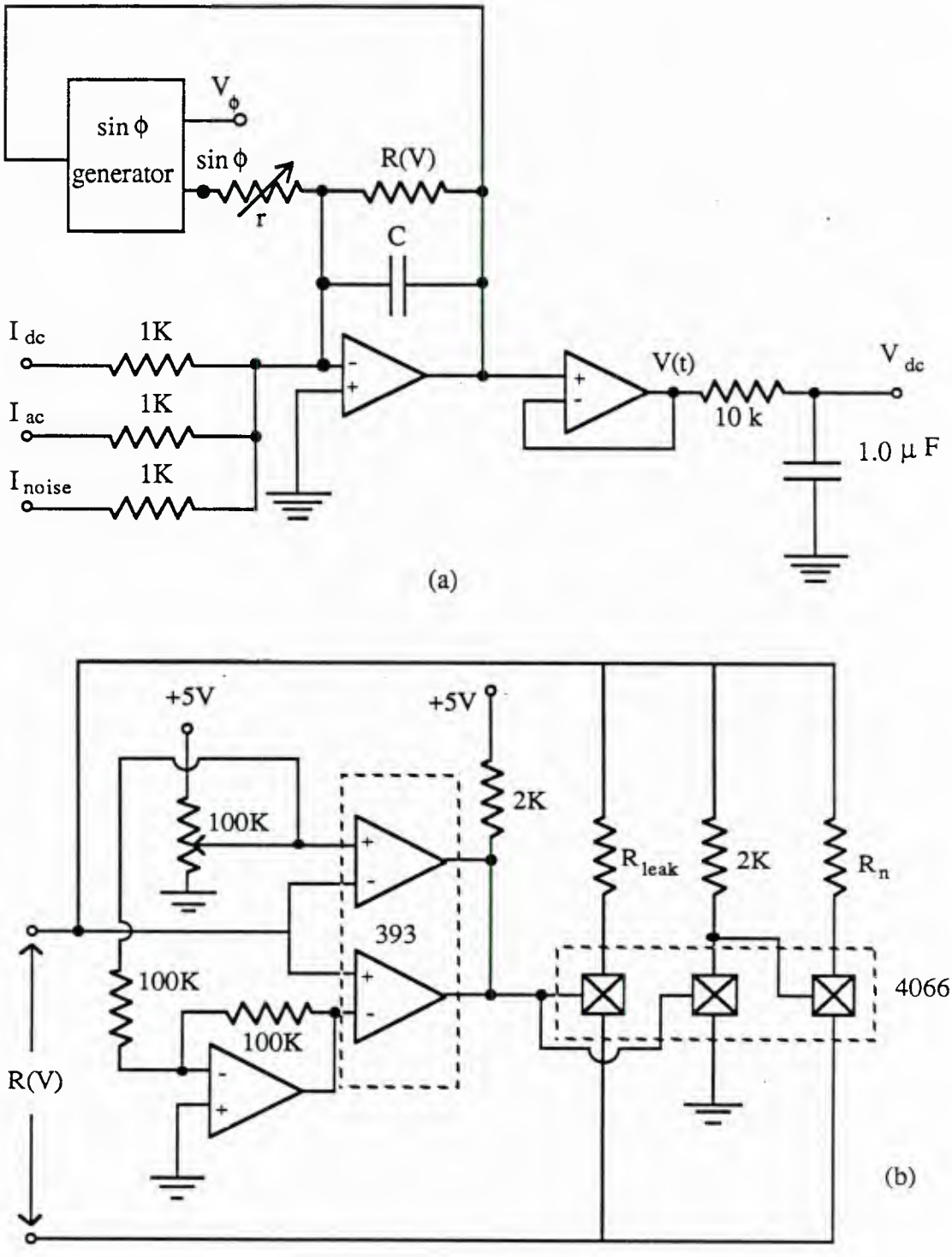

Fig. 4.4

(a) Analog circuit of the RCSJ model. (b) Circuit of the piecewise nonlinear resistor.

determined by later discussions. The analog switch 4066 is a very fast switch; its switching time is less than 1μs. Thus this voltage-dependent resistor is controlled by the instantaneous voltage V(t) instead of some time averaged value of V(t).

This circuit can be very easily generalized to include the famous cosϕ term, which arises from the interference between Cooper pair current and the quasiparticle current. If we include the cosϕ term, the RCSJ model will be

$$\frac{d^2\phi}{d\tau^2} + \frac{1}{\beta_c^{1/2}}\left[1+\varepsilon\cos\phi\right]\frac{d\phi}{d\tau} + \sin\phi = i_{dc} + i_{ac}\sin\left(\frac{\omega_L}{\omega_p}\tau\right) \qquad (4.14)$$

Notice the extra term $\left[\beta_c^{-1/2}\,\varepsilon\cos\phi\,(d\phi/d\tau)\right]$ is just a time derivative of sinϕ, which is very easy to construct. We neglect this term mainly because the present circuit gives very good results, comparable to the experimental ones. In addition, the existence and the sign of the cosϕ term is still lacking definitive experimental evidence. But in the future, it might be interesting to make systematic simulation studies of the cosϕ term effect on a Josephson junction.

4.2.2 Converting experimental values into simulation ones.

It is worth discussing in detail how to convert the experimental parameter values into the simulation ones. It is clear in the dimensionless RCSJ model

$$\frac{d^2\phi}{d\tau^2} + \frac{1}{\beta_c^{1/2}}\frac{d\phi}{d\tau} + \sin\phi = i_{dc} + i_{ac}\sin\left(\frac{\omega_L}{\omega_p}\tau\right) + i_n(\tau) \qquad (4.15)$$

that five dimensionless parameters: ω_L/ω_p, β_c, i_{dc}, i_{ac}, and $\gamma=hI_c/e(I_n^2R/4B)$ totally determine the output of Eq. (4.15). Apparently, if we make a one-to-one mapping: $(\omega_L/\omega_p)^{exp}=(\omega_L/\omega_p)^{sim}$, $\beta_c^{exp}=\beta_c^{sim}$, $i_{dc}^{exp}=i_{dc}^{sim}$, $i_{ac}^{exp}=i_{ac}^{sim}$, and $\gamma^{exp}=\gamma^{sim}$, we have a simulator that completely resembles a real junction.

Notice that $\omega=(\omega_L/\omega_p)$, $i=I/I_c$ are only relative ratios; we can choose the

denominators as some convenient values, and vary the numerators accordingly. We chose in the simulator:

$$I_c^{sim} = 1mA \tag{4.16}$$

and

$$f_p^{sim} = \omega_p^{sim}/2\pi = 10\ kHz \tag{4.17}$$

These two values will determine the capacitor value we should choose. Remember

$$\omega_p^{exp} = \sqrt{\frac{2eI_c^{exp}}{\hbar C^{exp}}} = \sqrt{2\pi k^{exp}\frac{I_c^{exp}}{C^{exp}}}$$

Thus

$$\omega_p^{sim} = \sqrt{2\pi k^{sim}\frac{I_c^{sim}}{C^{sim}}} \tag{4.18}$$

and if we use the values for k^{sim}, I_c^{sim}, and ω_p^{sim} in (4.12), (4.16) and (4.17), we have

$$C^{sim} = 32000\ pF$$

Choosing the value for R is not as flexible as for I_c^{sim} and C^{sim}. Since β_c is an absolute number, we have to choose R^{sim} according to a specific Josephson junction. For the SNAP junctions studied, by using the relation $\beta_c = (\omega_p RC)^2$, we get:

$$\beta_c^{exp} = \begin{cases} 3.4 & \text{use } R_n^{exp} \\ 30 & \text{use } R_{leak}^{exp} \end{cases} \tag{4.19}$$

Thus, to make

$$\beta_c^{sim} = \begin{cases} 3.4 & \text{use } R_n^{sim} \\ 30 & \text{use } R_{leak}^{sim} \end{cases} \tag{4.20}$$

we get

$$R_n^{sim} = 920\ \Omega, \qquad R_{leak}^{sim} = 2.7\ k\Omega$$

by using the values of ω_p^{sim} and C^{sim} chosen above. The gap voltage V_g can be measured in the unit of junction parameter $hf_p/2e=f_p/k$, where k is defined in (4.11). For

SNAP junctions, $V_g = 2.8$ mV, $f_p \approx 400$ GHz, while in all cases $k^{exp} = 4.83\times10^{14}$ Hz/V. Thus

$$V_g^{exp} = 3.38\, f_p^{exp} / k^{exp}$$

If we translate this into simulator units, we have

$$V_g^{sim} = 3.38\, f_p^{sim} / k^{sim} \approx 1.7V$$

The noise source is a white noise generator whose voltage output can be converted into noise current through a source resistor R_s. To make

$$\gamma^{exp} = \frac{\hbar I_c^{exp}}{e k_B T} = \frac{1}{\pi k^{exp}} \frac{I_c^{exp}}{k_B T} \tag{4.22}$$

equal to

$$\gamma^{sim} = \frac{1}{\pi k^{sim}} \frac{I_c^{sim}}{(I_n^2 R^{sim}/4B)} \tag{4.23}$$

(where I_n is the rms noise current in bandwidth B, and R^{sim} is R_n^{sim} or R_{leak}^{sim} depending on whether the operating point is above or below the gap), we have the following relation linking the noise current in simulations with the noise temperature in experiments:

$$T^{exp} = \frac{1}{k_B} \left(\frac{k^{sim}}{k^{exp}}\right) \frac{I_c^{exp}}{I_c^{sim}} \left(I_n^2 R^{sim}/4B \right) \tag{4.24}$$

This tells how much the equivalent noise temperature T^{exp} is in an experiment for given noise current I_n in simulations.

Table 4.1 summarizes the results discussed above, listing the conversion relations between the experimental and the simulational parameters.

Table 4.1

Parameters	Experiment	Simulation
k	$k^{exp} = 2e/h$	$k^{sim} = 1/4R_{in}C_{in}V_{max}$
I_c	I_c^{exp}	I_c^{sim}
C	C^{exp}	C^{sim}
R	R^{exp}	R^{sim}
ω	$\omega_p^{exp} = [(2e/\hbar) (I_c/C)]^{1/2} = [2\pi k^{exp} I^{exp} / C^{exp}]^{1/2}$	$\omega_p^{sim} = [2\pi k^{sim} I_c^{sim} / C^{sim}]^{1/2}$
β_c	$\beta_c^{exp} = (\omega_p^{exp} R^{exp} C^{exp})^2$	$\beta_c^{sim} = (\omega_p^{sim} R^{sim} C^{sim})^2$
V_g	$V_g^{exp} = \alpha (h/2e) f_p^{exp} = \alpha f_p^{exp} / k^{exp}$	$V_g^{sim} = \alpha f_p^{sim} / k^{sim}$
i_{dc}	$i_{dc}^{exp} = I_{dc}^{exp} / I_c^{exp}$	$i_{dc}^{sim} = I_{dc}^{sim} / I_c^{sim}$
i_{ac}	$i_{ac}^{exp} = I_{ac}^{exp} / I_c^{exp}$	$i_{ac}^{sim} = I_{ac}^{sim} / I_c^{sim}$
γ	$\gamma^{exp} = \hbar I_c^{exp} / ek_BT = (1/\pi k^{exp}) I_c^{exp} / k_BT$	$\gamma^{sim} = (1/\pi k^{sim}) I_c^{sim} /(I_n^2 R^{sim}/4B)$
T	$T^{exp} = (1/k_B) (k^{sim} / k^{exp}) (I_c^{exp} / I_c^{sim}) (I_n^2 R^{sim} / 4B)$	

Table 4.1. Converting relations between the experimental parameters and the simulational ones.

4.3 Performance of the simulator

It is interesting to compare the performance of the simulator to predictions from an ideal RCSJ model.

4.3.1 Performance of the simulator in the linear region. ($\Delta\phi<<1$)

1) Frequency response.

In small phase approximation ($\sin\phi \approx \phi$), the RCSJ model reduces to a damped driven harmonic oscillator, whose resonant frequency is ω_p and the full width of resonance at the 3dB point $\Delta\omega$ is given by $\Delta\omega=\beta_c^{-1/2}\omega_p$. Fig. 4.5a shows the frequency response of the simulator at small drive amplitude $i_{ac}<<1$. The horizontal axis is the driving frequency normalized to f_p; the vertical axis is the amplitude of the voltage response V(t). The peak is indeed at the calculated f_p, and the width of resonance $\Delta\omega/\omega_p\approx 1/6$ gives $\beta_c=36$, which is just the value we expected.

2) The resonant frequency vs. dc bias, ω_R - i_{dc}.

With the help of a tilted washboard potential picture, it is clear that when we increase the dc bias current i_{dc}, we not only tilt the overall washboard, but also change the curvature at the bottom of the potential well, thus changing the oscillation frequency ω_R there. Quantitatively:

$$\omega_R = \sqrt{\frac{1}{LC}} = \sqrt{\frac{\hbar I_c \cos\phi}{2eC}} = \sqrt{\frac{\hbar I_c (1-\sin^2\phi)^{1/2}}{2eC}}$$

$$= \omega_p (1-i_{dc}^2)^{1/4} \qquad (4.25)$$

Fig. 4.5b shows the measured resonant frequency vs. dc bias current. The way of measuring ω_R uses the fact that at ω_R, $\omega_R L = 1/\omega_R C$, the impedance of the parallel LC circuit is infinite, and thus all the current flows through the resistor. In this case, there is no phase shift between the current and the voltage. Having this in mind, we use a dual

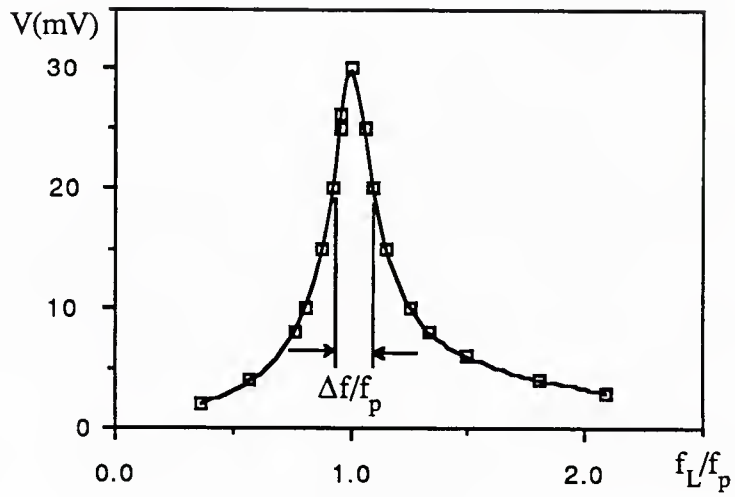

Fig. 4.5a

Voltage response of the simulator to the drive frequency of an ac current with a small amplitude.

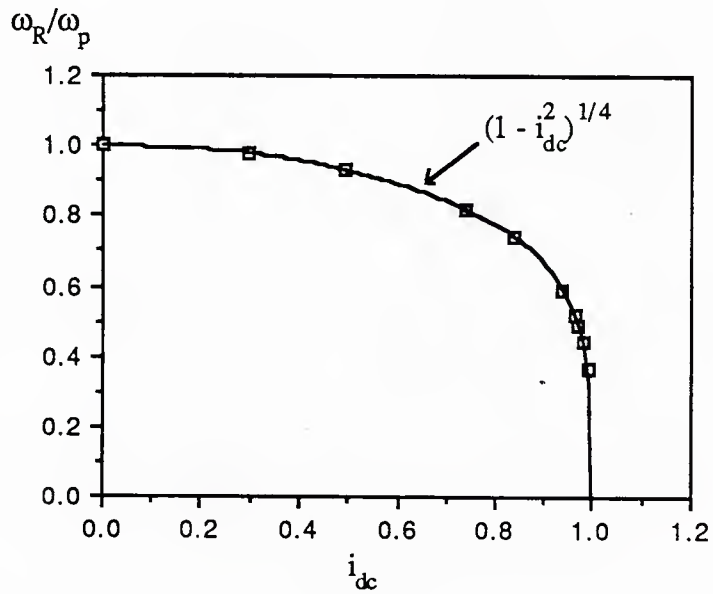

Fig. 4.5b

Resonanant frequency vs. the dc bias current.

trace oscilloscope to monitor both the current and the voltage on the same screen. If we adjust the driving frequency so that there is no phase shift between the two; then this driving frequency will be the resonant frequency ω_R. The determination of the resonant frequency in this way is certainly more accurate than by using maximum amplitude of V(t) as a criterion, since the peak of the response curve (Fig. 4.5a) is rather flat.

The result shown in Fig. 4.5b is quite satisfactory compared to the theoretical curve. Now we know that the circuit works as it is supposed to, at least for small amplitude oscillations, and also we know that our parameter calibration is correct.

4.3.2 Performance of the simulator in the nonlinear region.

Fig. 4.6 and Fig. 4.7 show the performance of the simulator in a nonlinear region ($\sin\phi \neq \phi$). Fig. 4.6 is a systematic checking of the damping effects on the hysteresis of the I-V curves. According to the digital simulation done by Stewart[63], the hysteresis should start when β_c takes a value in the interval (0.5, 1.0). Our result shows that the hysteresis starts at the value $\beta_c \approx 0.64$, which is consistent with Stewart's prediction. (These I-V curves are taken with a linear resistance R instead of piecewise nonlinear one, so there is no ambiguity in β_c).

Fig. 4.7 shows the chaos threshold in the i_{ac}-(ω_L/ω_p) plane. We monitored V(t) with both a spectrum analyzer and a Poincaré section monitor (which is a pulse generator synchronized to the driving frequency, whose output controls the Z-axis (brightness) of an oscilloscope). We define a chaotic state as a state such that the Poincaré section has the pattern of a strange attractor and the power spectrum shows wide band noise. These two criteria are consistent in all our experiments; we have never found that one is statisfied while the other is not. In Fig. 4.7, chaos threshold data taken from a linear resistance simulator and one with the piecewise resistor are compared; the R_n is the same in both cases. The overall features agree with the previous work (cf. Fig.2.5 and Fig. 2.6). The

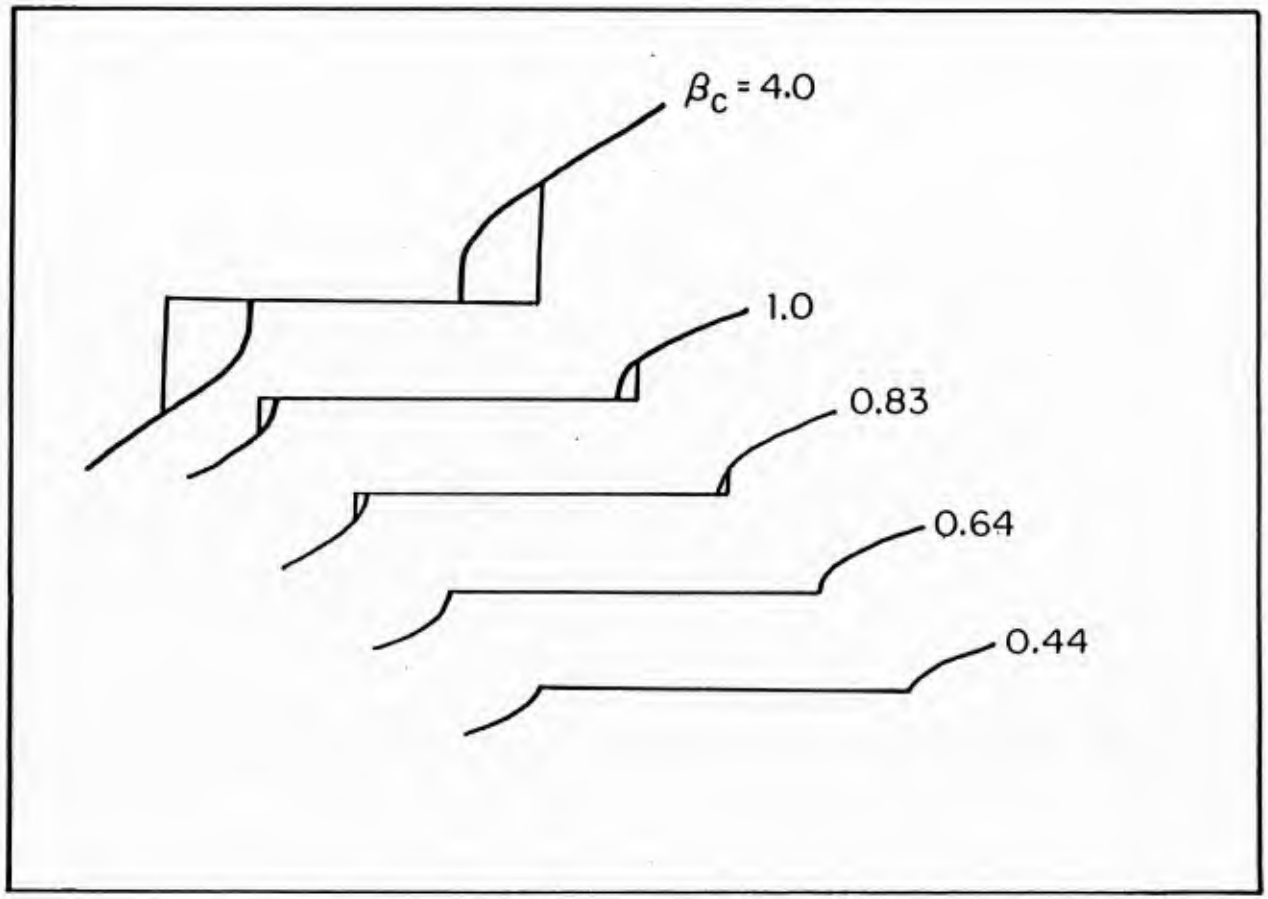

Fig. 4.6

Simulated I-V curves with different damping. Note the hysteresis disappears at β_c=0.64.

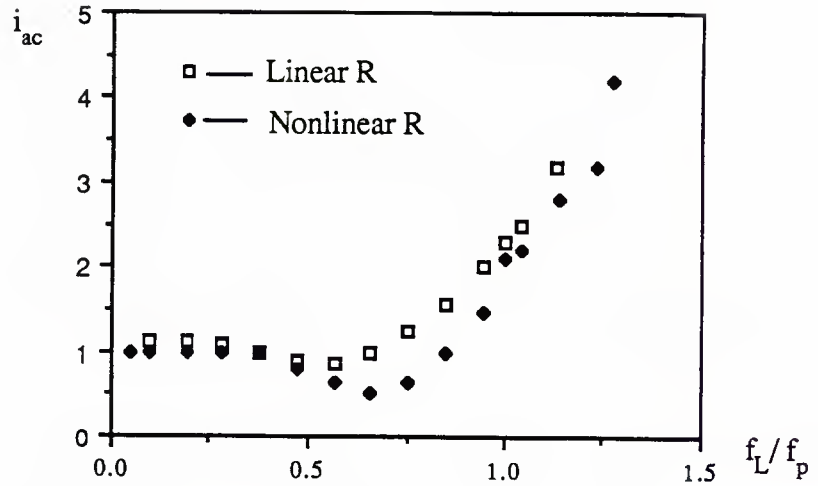

Fig. 4.7

Simulated threshold of transition to chaos in the i_{ac}-f_L/f_p plane. The squares are the data taken with a linear resistance which gives β_c=4; the dots are the ones from a piecewise nonlinear resistance with β_c=4 (using R_n), and β_c=36 (using R_{leak}).

threshold has its minimum at ~2/3 ω_p instead of at ω_p itself. This is not too surprising because we are dealing with a large amplitude drive; when $\sin\phi \neq \phi$, the potential is softer than that of a harmonic oscillator, and the resonant frequency shifts to lower value. At lower frequencies; the threshold seems flattening out at $i_{ac} \approx 1$. This means that, in an adiabatic case, when the driving current amplitude reaches the value of critical current, the system may start moving chaotically. (The motion of the system is not neccessarily chaotic for all the regions in $i_{ac} \geq 1$; there are chaos-free windows above the threshold.) As the driving frequency exceeds ω_p, the threshold level goes up very quickly; in fact, when ω_L/ω_p=1.4, the chaos threshold for i_{ac} already exceeds 5. That is consistent with Kautz's result (2.22); when $\omega_L/\omega_p >> 1$, none of the oscillation modes in (0, ω_p) in the system can be excited (cf. section 2.3.2 of this report); thus chaos will not occur.

4.4 Study of noise effects on a Josephson junction with the simulator.

It has been observed[64] that the critical current of some Sn-SnOx-Sn junctions shows temperature reentrant behavior. That is, when the ambient temperature goes down, the measured critical current I_c^{exp} goes down too, after an initial rise just below T_c. This very abnormal behavior might have its root in some macroscopic quantum mechanics mechanism. But in classical mechanics, we have a possible explanation also: When the ambient temperature goes down, the leakage resistance goes up exponentially for an ideal tunnel junction. This causes a sharp decrease in damping, since $\beta_c \propto R^2$, which could make premature switching more likely to happen, since a ball is easier to be kicked out of a less frictional well. This certainly is a qualitatively correct picture. But quantitatively, it is not clear how strongly this damping effect will affect the switching behavior. We have theories for both very underdamped ($\beta_c >> 1$) and very overdamped ($\beta_c << 1$) cases, but not in between, which is the region in which the junctions of interest fall. With the aid of simulations, we can very easily check the hypothesis that the temperature reentrant behavior is caused by the change of damping.

Fig. 4.8 shows a set of I-V curves taken from the simulator at different noise levels. The noise current is converted into a γ parameter by using the leakage resistance R_{leak}. This is justified, at least for up switching, since the ball was trapped in the potential well before switching, and the corresponding voltage is much smaller than the gap voltage V_g. For the down switching, the use of R_{leak} is justified for most of the cases also, because from the down part of the hysteretic curves shown in Fig. 4.8, the voltage goes down quite far below the gap voltage before it jumps down to the zero-voltage state. This observation is confirmed by monitoring the instantaneous voltage V(t) by an oscilloscope; its value remains all the time below the gap voltage right before the down switching happens.

From Fig. 4.8, we can see that, as we increase noise (decrease γ), the system

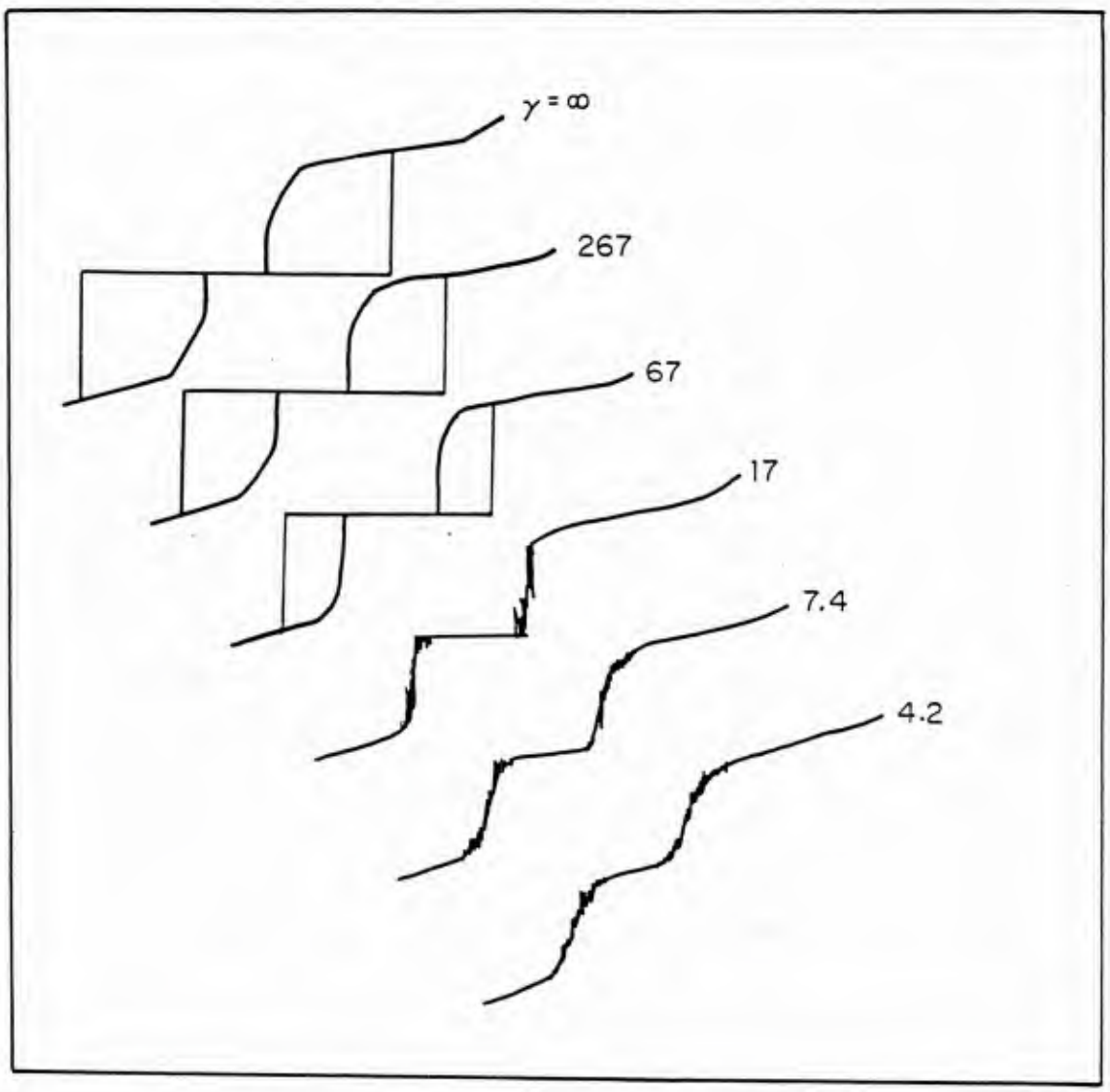

Fig. 4.8

Simulated I-V curves taken at different noise levels with β_c=4 (using R_n), and β_c=36 (using R_{leak}). The factor γ (using R_{leak}) corresponds to the noise level in the SNAP1 junction (I_c=425μA).

switches at lower current values; this switching point is the measured critical current in experiments. Also, the down switching happens at larger current values. Eventually, the up switching and down switching overlap, and the hysteresis disappears. As we increase the noise further, we get a noise-rounded corner like that in Ambegaokar and Halperin's model (cf. Fig. 2.10) instead of a sharp up-switch resulted from a decisive, irreversible premature switching.

Fig. 4.9 shows the noise-reduced critical current I_c vs. the noise factor γ. I_c is taken at the middle point of the distribution, and the data were taken from a large range of β_c, from 0.5 to 400. The circled data are the ones taken on a nonhysteretic I-V curve like the ones in the lower half of Fig.4.8. The critical current in this case is defined as the crossing point of the extrapolation of the linear part of up switching curve and the zero-voltage axis. The smooth curve is an approximate theoretical result derived by Danchi et al. (Eq. (2.32)). The derivation is based on a purely thermal activation model and assumes $\beta_c=\infty$. Surprisingly, we found that as long as the junction is hysteretic, no matter how small the β_c is, the measured critical current fits into the theory very well. But as soon as the hysteresis is gone, the measured critical current is always above the theoretical value for the zero damping case. A possible explanation is that when the noise level is so high that there is no other bistable state the system can jump to (no hysteresis), the ball has to hop well by well. This is very much the same picture as in Ambegaokar and Halperin's theory, in which the damping stops the ball from freely sliding further down. In this case, the noise effect of reducing the measured critical current is a rounded corner, which is much less significant than the noise-induced premature switching to the gap voltage in the underdamped regime. That is why we have bigger measured critical current than a hysteretic case.

One may wonder why our results are so similar to those in the Ambegaokar and Halperin case, $\beta_c=0$, while in our case, $\beta_c\approx$1-100; the damping is not infinite even in the

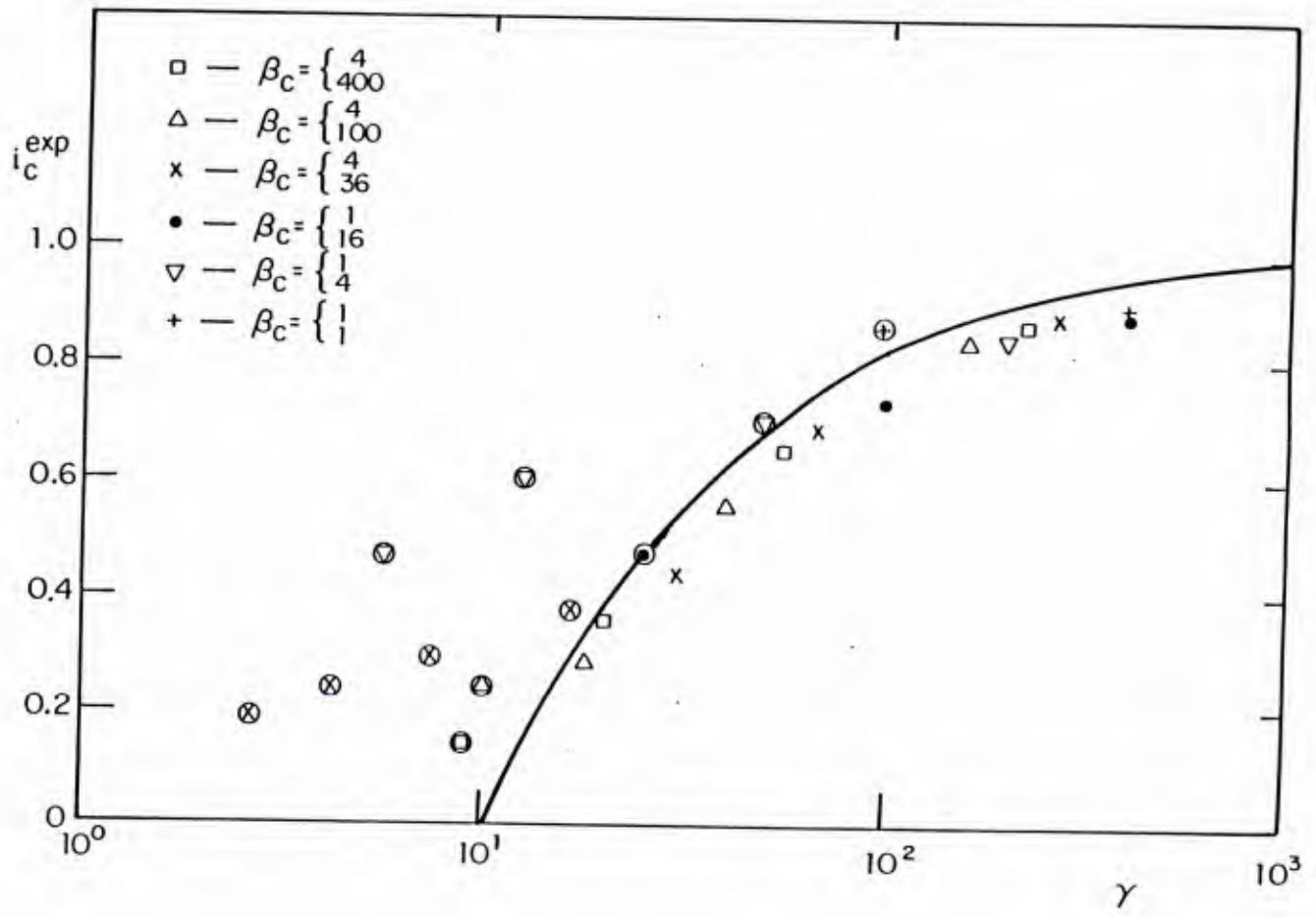

Fig. 4.9 Measured critical current from the simulated I-V curves vs. γ with different damping. The circled data are taken from nonhysteretic I-V curves. The solid curve is from the approximate formula (2.32) derived in the $\beta_c=\infty$ limit.

nonhysteretic cases.

The answer may lie in the famous fluctuation-dissipation theorem, which states that the damping R and the fluctuation I_n are related in such a way, that

$$I_n^2 R \propto k_B T \qquad (4.27)$$

In our simulations, we can vary I_n and R independently; we do not have to keep their product constant. This is somehow artificial compared to an experiment in a real physical system. But if we assume that (4.27) is valid in our simulations and interpret R as some damping factor not necessarily equal to the resistance value, then we can say that if we increase the noise current I_n, we either increase the equivalent noise temperature with the damping unchanged; or equivalently, we decrease the R value (increase the damping) to keep the equivalent noise temperature constant. The first viewpoint is a more helpful picture in the hysteretic case, since damping has no effect, while the second viewpoint is a more helpful picture in the nonhysteretic case, since in the small γ limit in Fig. 2.10, the variation of γ does not cause significant change in I-V curves, while change of damping may cause a very noticeable effect.

From Fig. 4.9 we should be able to conclude that as long as the junction is hysteretic, the critical current is solely determined by γ and independent of β_c. Fig. 4.10 shows the measured simulated critical current vs. β_c with γ kept constant. Again, the circled data points are the ones taken from nonhysteretic I-V curves. From this figure, we can see more explicitly that the measured critical current is independent of β_c as long as the I-V curve remains hysteretic. The data in Fig. 4.9 and Fig. 4.10 indicate that although the damping effect on noise-induced switching seems a very plausible explanation for temperature reentrant behavior, it is not applicable to the data of Akoh et al.[64] In their measurement, the temperature reentrant behavior occurs only for the hysteretic curves. There are some non-RCSJ-like, probably macroscopic quantum phenomena, implied by those data.

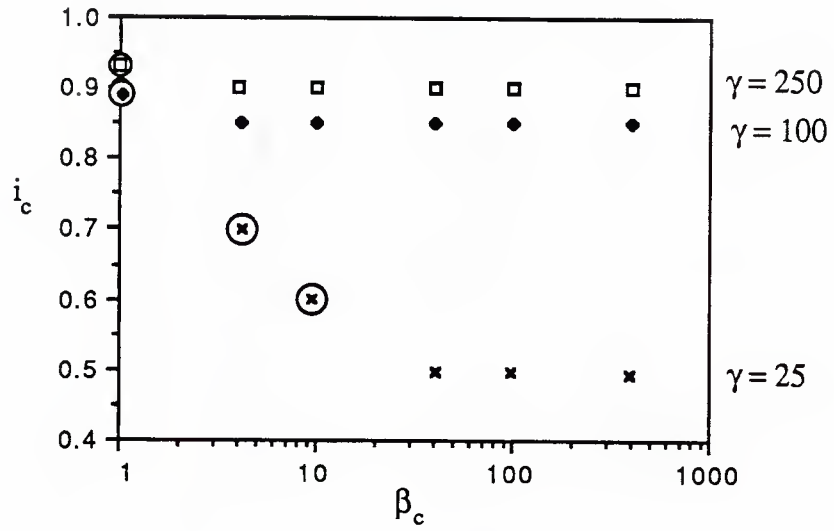

Fig. 4.10

Measured critical current vs. β_c at different γ values. The values of β_c are calculated from R_{leak}. The circled data are taken from nonhysteretic I-V curves.

However, from Fig. 4.10 we can see that when the junction becomes nonhysteretic, the critical current is indeed dependent on β_c. P.A.Lee[36] generalized Ambegaokar and Halperin's $\beta_c=0$ theory to the case $0<\beta_c<<1$. However, to our knowledge, there is no theory about this problem covering the whole range of β_c. From purely empirical studies, we have found that in the nonhysteretic regime, the measured critical current has the following logarithmic dependence on γ and β_c, with $B/A \approx 3/2$.

$$i_c = A \ln \gamma - B \ln \beta_c + C \qquad (4.28)$$

Fig. 4.11 shows the plot of i_c vs. $\log(\gamma / \beta_c^{3/2})$, where the values of β_c are calculated by using R_{leak}. The straight line is

$$i_c = 0.069 \ln \left[5\times10^3 \left(\frac{\gamma}{\beta_c^{3/2}}\right)\right] \qquad (4.29)$$

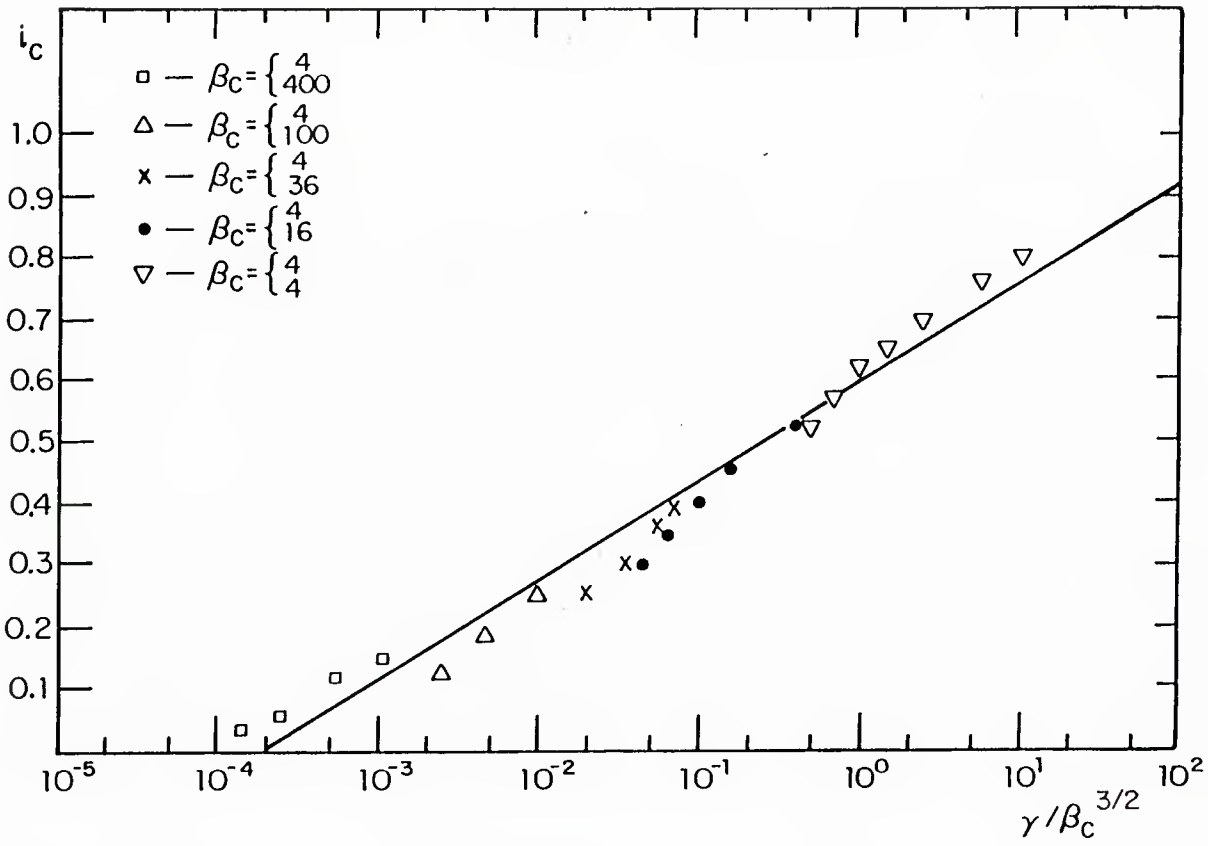

Fig. 4.11

Measured critical current from the simulated I-V curves vs. $\log(\gamma/\beta_c^{3/2})$. All the data are taken from nonhysteretic I-V curves. The straight line is $i_c=0.069\ \ln(5\times10^3\ \gamma/\beta_c^{3/2})$.

This straight line fits the data very well over an amazing large range of $\gamma / \beta_c^{3/2}$ (five decades). We have no theoretical explanation for this empirical result. Hopefully, it can be found in future work.

CHAPTER V

DATA ANALYSIS

5.1 Introduction

We have studied the responses of several SNAP junctions to far-infrared laser radiation at 245, 419 and 604 GHz. It was later found out that the plasma frequencies f_p of these junctions are about 400 GHz. So at a driving frequency of 419 GHz, which resonates with the Josephson junction system, we should expect the system to show some strong nonlinear dynamic effects, such as chaos and high sensitivity to perturbations. Indeed, we saw some quite unusual behaviors of these junctions when they are irradiated at 419 GHz ($f_L/f_p \approx 1$). For example, regions of meandering voltage may appear on an otherwise well-defined and flat step. At such chaotic parts of the I-V curves, there is an extremely high level of low frequency noise, corresponding to a thermal noise temperature of $\sim 10^{12}$ K at frequencies around 100 Hz. Negative resistance regions are also observed. At some laser power levels, the I-V curves show some subharmonic steps (1/2 or 2/3) in the absence of an adjacent integer step (the 1st step). None of these phenomena have been seen in the lower current density junctions studied in this frequency range.[29,49] The lower plasma frequencies of those junctions make the frequency ratio $f_L / f_p \geq 2$. (For Junction P89 in ref. 49, which is the most studied junction in that report, $f_p \approx 100$ GHz, so even at 245 GHz, $f_L / f_p \approx 2.5$) From the state diagram in Fig. 2.5 and the argument in section 2.3.2, we know that chaos is very unlikely to happen at this drive/plasma frequency ratio.

At 604 GHz, for the SNAP junctions, $f_L / f_p \approx 1.5$. From Fig. 4.7, we know that the chaos threshold is very high ($i_{ac} \geq 5$) in that case. In our experiment, we did not see any of the chaotic behavior mentioned above. But serious deviations of the measured step widths from the simulated ones have been observed[67]. That is probably due to the

instabilities caused by being close to chaotic regions.

At f_L = 245 GHz, which corresponds to $f_L / f_p \approx 0.6$, this frequency ratio is in the parameter region where chaos should be most likely observed (cf. Fig. 4.7). In fact, at this frequency we did see in general that the I-V curves appeared to be very noisy, but we did not see any meandering steps or subharmonic steps. This less chaotic behavior might be explained by the fact that the dipole antenna resonates at 400 GHz (cf. Fig. 3.7), so the coupled laser radiation power at 245 GHz is insufficient to drive the system into a very nonlinear region.

Finding out the parameters of the junctions is a very crucial step in analyzing the experimental data by simulations. It turns out to be quite tricky for a junction with this small size (a few square μm), especially if we want to determine the parameters within a few per cent. We will discuss in detail how to achieve this goal. Then we will focus on a narrow parameter region to study in detail the nonlinear dynamics behind the apparent chaotic behavior on the dc I-V curves, especially the interaction of a random noise source with a nonlinear system. The results are very interesting both for understanding the nature of randomness in a highly nonlinear system and building practical Josephson devices.

5.2 Survey of the experimental results

We have studied four SNAP junctions made on a single wafer in the same process. We have studied two of them in great detail; they are labled as SNAP1 and SNAP2 henceforth.

SNAP1 has the following parameters: Its area is about $5\mu m^2$; at 4.2K, I_c = 425μA; $V_g = 2\Delta/e$ = 2.8mV, R_n = 3.3Ω, $R_{leak} \approx 3R_n \approx 10\Omega$, and C = 0.23 ± 0.03 pF. The subgap leakage-resistance was measured by magnetic depression of the critical current. The capacitance value is roughly estimated from the SQUID resonance measurements on larger junctions made on the same chip, and finely adjusted by the best

simulation fits. From these parameters, we estimate that the plasma frequency f_p = 390±20GHz, and the McCumber number β_c = 3.3±0.4, for voltage above the gap (using R_n) and β_c = 28±3 below the gap (using R_{leak}).

Since the junction impedance is quite low compared to that of the antenna (>100Ω), and at 419 GHz neither of the conditions (2.10) is satisfied ($\omega L \approx 1/\omega C \approx 2\Omega$, $R \approx 3\Omega$), the junction is effectively ac current biased. Accordingly, we should expect to see some associated nonlinear effects, such as subharmonic steps and chaos.

Some of the I-V curves of an irradiated junction taken at certain laser power levels are shown in Fig. 5.1; the radiation frequency is 419 GHz. In Fig. 5.1, the ac current amplitude i_{ac} is assumed to be proportional to the square root of the laser power measured independently by a pyroelectric detector; the proportionality factor is determined by simulation fits. As we increase the laser power from the bottom trace (i_{ac} = 0.92), the 2/3 subharmonic step appears right below the 2nd step, with the 1st step missing. When we increase the laser power to i_{ac} = 1.49, both the 2/3 and the 2nd steps become very noisy, then they are totally destroyed at i_{ac} = 1.53. There is a little piece of negative resistance at the right edge of the 2nd step at i_{ac}=1.53. These I-V curves have several unusual features compared to those of better-behaved voltage-biased junctions.[49]

1) Presence of a subharmonic step in the absence of the adjacent integer steps. Presence of subharmonic steps indicates that we are in an ac current bias regime, while the absence of the adjacent integer step tells us that the system is in a highly nonlinear region where a more complex pattern of phase locking including subharmonic phase locking [$d\phi/dt=(n/m)\omega$] is favored over the simpler pattern (m=1).

2) Noisy steps. Although noisy I-V curves are sometimes seen in the junctions of ref.49, most of those noisy parts occurred between the steps of the I-V curves, especially at the edges of the steps. This is not too surprising since the dynamic resistance takes very large values at the edges of steps. Thus any current noise will be amplified there, causing

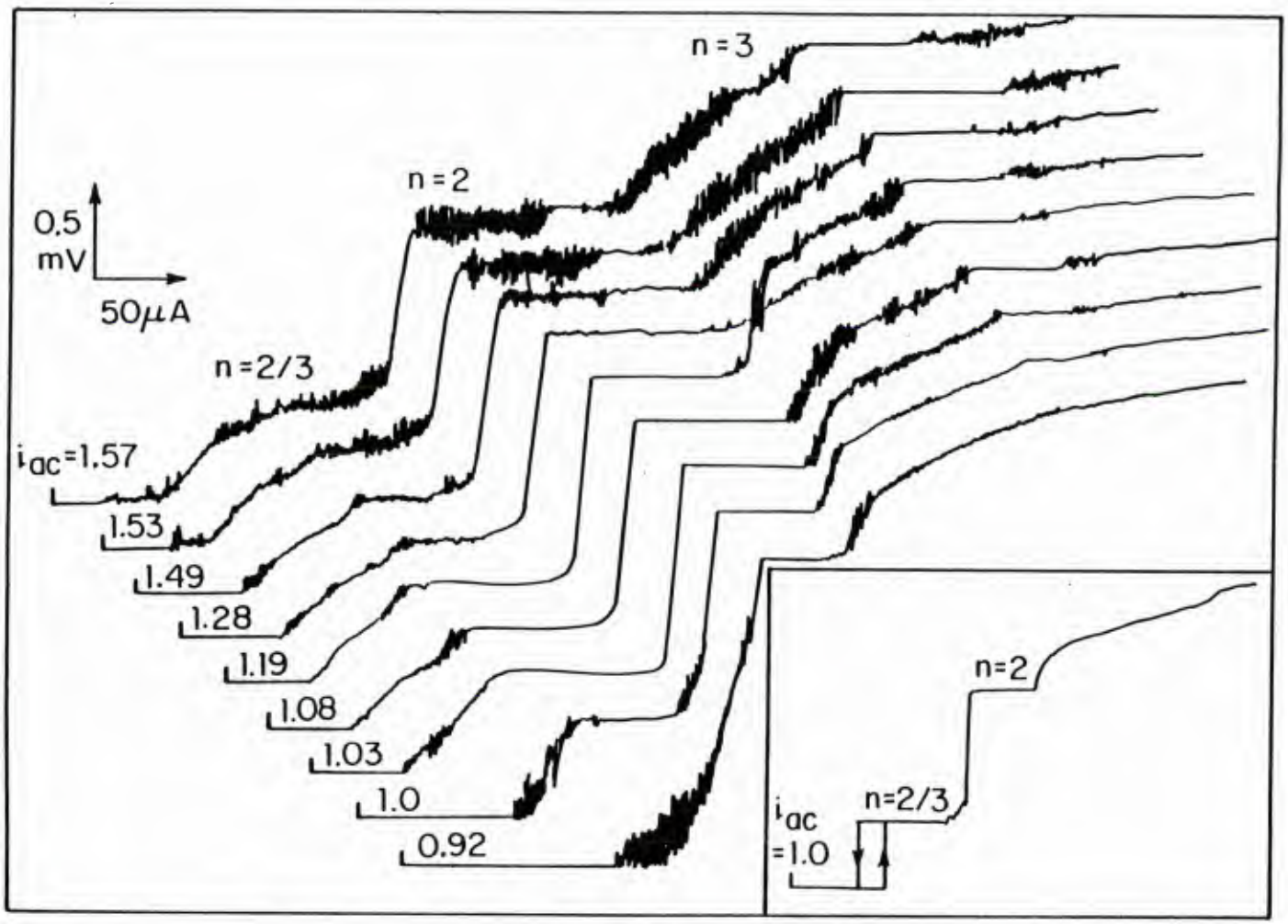

Fig. 5.1 I-V curves of the SNAP1 junction irradiated with 419 GHz radiation. The curve in the box is the simulated I-V curve for i_{ac}=1.0. Both the experimental and the simulated I-V curves show the 2/3 step.

the system to be very sensitive to external perturbations such as laser power fluctuations and noise triggering. But in our case, whole steps (2/3 and 2nd steps in Fig. 5.1) are destroyed, and replaced by a step-like but very noisy part, instead of a smooth tilted free-running I-V curve. This behavior certainly cannot be explained by external fluctuations alone. The most likely explanations are either: (a) the system went into chaos in these noisy regions becoming phase-unlocked, or (b) these steps are so unstable that in the presence of unavoidable fluctuations (thermal noise, for example), the phase locking of the whole step is destroyed.

3) A negative resistance region. This is a smooth part of some of the I-V curves. In Fig. 5.1, it appears at the right edge of the 2nd step for the curve with $i_{ac} = 1.53$. It is reproducible for both up and down sweeps. There can be many explanations for negative resistance. In our case, from the simulation study of some other I-V curves discussed later, one possible explanation is that in the negative resistance region, the system is jumping back and forth between two states, due to noise triggering. If the lower voltage state becomes more stable relative to the higher voltage state as the current increases, the system tends to spend more time in the lower voltage state at higher current. Thus the time-averaged voltage goes down as the current goes up. If the fluctuating voltage is mainly at high frequency, it will be averaged out by our measuring instruments, yielding a smooth curve with a negative slope. In the few reports of experimental studies of chaos in Josephson junctions,[15,17] it seems to be a common phenomenon that a negative resistance is closely associated with chaos.

Fig. 5.2 shows an even stronger evidence of chaos: at $i_{ac} = 2.0$, the I-V curve showed a large 1st step, which did not appear at all for any of the laser power levels in Fig.5.1. The junction is phase-locked to the 1st Josephson step at the two edges of the step giving a well-defined flat step, but it wanders off from the step in the center. This meandering voltage region in the step certainly can not be explained by the fluctuation of

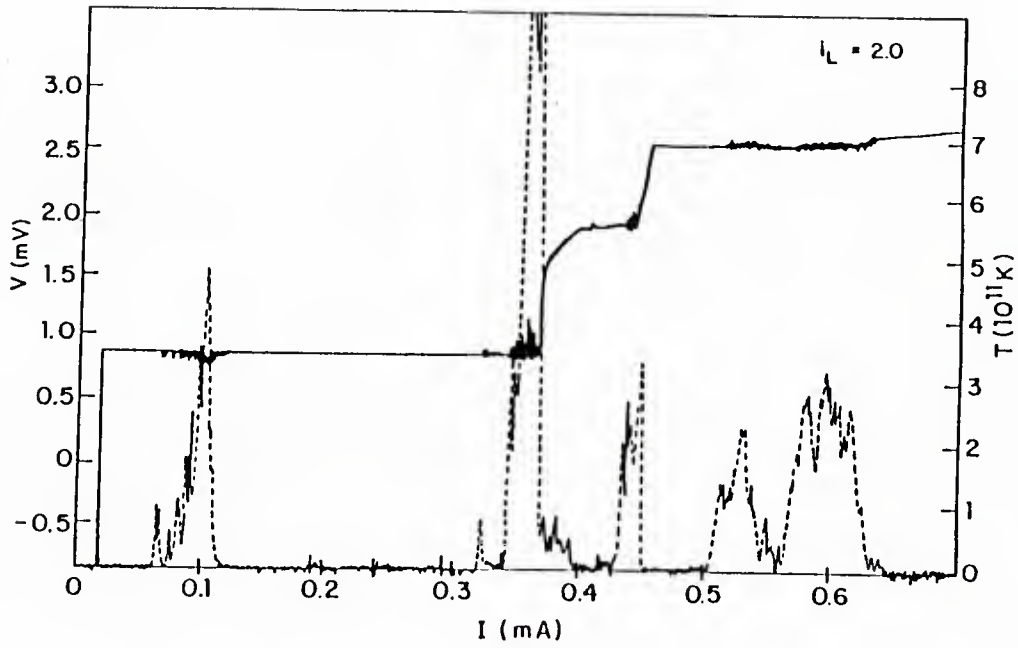

Fig. 5.2

I-V curve of the SNAP1 junction taken at i_{ac}=2.0. The big flat step is the 1st step; a region of meandering voltage is clearly seen far away from the step edge. The dashed line is the measured effective noise temperature at 100Hz defined in (5.1).

the laser power alone, since this would only induce voltage fluctuations at the edges of steps, where I-V curves are most sensitive to laser power. In that case, the edges of the step should be destroyed first, before the center.

The dashed curve in Fig. 5.2 is the noise power density measured at low frequency (100 Hz) by using a PAR 124 lock-in as a bandpass amplifier. The noise density is converted into an equivalent thermal noise temperature defined as

$$T_n = \frac{V_{rms}^2}{4 k_B R_n B} \qquad (5.1)$$

with B the bandwidth in Hz; the peak noise level is typically in the order of 10^{12} K at this low frequency. Low frequency power spectrum measurements reveal that most of this extremely high level of noise is below 100 kHz. The spectrum at such low frequencies is usually some very complicated form with a roughly power law envelope $1/f^{\alpha}$, $\alpha \approx$ 1-4. We failed to understand these spectra. The main reason is because this frequency range is so low compared to the driving frequency (10^{-9} of f_L) that it is impossible to study such a low frequency spectrum in either digital or analog simulations. Besides, the linewidth Δf_L of the far-infrared laser is typically 10MHz, so $\Delta f_L/f_L \approx 10^{-5}$. In the time regime, that means the laser can be viewed as sending out a series of wave packets, each one having a duration of $\tau \approx 1/\Delta f_L \approx 10^{-7}$sec or 10^5 periods, but each wave packet being totally incoherent from the others. What we see in an experiment in the time scale of t is the averaged effect caused by a number t/τ of such incoherent wave-packets. So for a frequency such that $f << \Delta f_L \sim 10^7$Hz, the frequency spectrum will be an extremely complicated averaged result caused by $\Delta f_L/f$ incoherent wave packets. This fact makes the study of the frequency spectrum at low frequency (< 100 kHz) rather fruitless to attempt. In fact, we have tried to study the frequency response of the driven junction to some signals deliberately put into the system (white noise or sinusoidal signal, with typical frequencies ranging below 100 kHz); the resulting power spectra were too complicated to

understand in any evident way. We also tried to modulate the laser amplitude with a frequency f_m, (f_m < 100 kHz) so that the laser radiation has two frequency components, $f_L + f_m$, and $f_L - f_m$ in addition to f_L. At the period-doubling bifurcation point, there should be $(f_L+f_m)/2$ and $(f_L-f_m)/2$ frequencies in the system as well as $f_L/2$. By using the nonlinear Josephson junction as a rectifier to demodulate the frequencies, we might be able to see the period doubling of the modulation frequency to $f_m/2$.[65] This interesting test failed, perhaps because $f_m << \Delta f_L$.

Instead of the low frequency power spectrum, we concentrate on some specific features on the dc I-V curves which all the incoherent wave packets will produce so that the averaged features are not different from the ones produced by a single wave packet. One such feature is shown in the I-V curve with i_{ac} = 1.0 in Fig. 5.1. The combination of the 2/3 step and the 2nd step is a feature independent of the initial conditions chosen for ϕ and $d\phi/dt$; in other words, two incoherent wavepacks (equivalent to two different sets of initial conditions) will both produce this feature. In fact, this feature only depends on the junction parameters, ω_p, β_c, and the external parameters i_{ac}, f_L. It was later found that the appearance of this feature is very sensitive to f_L/f_p, so it can serve as a "fingerprint" to help to find out what parameter range in f_p the junction belongs to.

SNAP2 has a different fingerprint from that of SNAP1, even though they were made on the same wafer. SNAP 2 was designed to have the same area as that of SNAP 1, but for such a small junction this can only be confirmed to within 20% by SEM photo because the top surface geometry does not accurately reflect the real junction area. The junction has the following parameters: At 4.2 K, $2\Delta/e$ = 2.8 mV, I_c = 520 μA, R_n = 2.7 Ω, $R_{leak} \approx 8$ Ω. If this junction had exactly the same current density and barrier dielectric properties as SNAP1, we could just simply scale the capacitance to the critical current and obtain C=(520/425)×0.23=0.28pF. Since for a flat sandwich type of junction (uniform tunnel barrier), both the parameters $\omega_p = (2eI_c/\hbar C)^{1/2}$ and $\beta_c = (\omega_p RC)^2$ are only

functions of the current density and the dielectric properties of the insulating barrier and are independent of the cross sectional area of the junction (if we ignore fringing effect), these two junctions should have similar ω_p and β_c values. Since these two parameters totally determine the behavior of the Josephson junction, we should expect these junctions to have the same response to radiation even if they might have different areas. The only difference should be the absolute step widths, since the step widths scale with the critical current of each individual junction which is area dependent.

However, this is not what we have seen. Although SNAP2 also showed chaotic behavior for a large range of laser power, it exhibits quite a distinctive difference in its irradiated dc I-V characteristics. In Fig. 5.3a, we can see that instead of having the 2/3 and the 2nd steps, the I-V curves of SNAP2 showed the 1/2 and the 2nd Josephson steps. We could not find the 2/3 step at any laser power level studied. All we could see is a little bump at the left edge of the 1/2 step at certain levels of laser power shown in Fig. 5.3a; the top of that bump is roughly at the voltage value where the 2/3 step would appear. These different features on the I-V curves certainly indicate that the parameters ω_p and β_c for the two junctions can not be exactly the same. This is hardly surprising since the critical current density is a very sensitive function of the barrier thickness. If we change the barrier thickness by 8Å, the current density will change[66] by a factor of 10, so a subatomic thickness difference can cause significant change in the current density, and hence ω_p and β_c. For a sputtered amorphous Si layer, such a variation in thickness is hardly unlikely.

In contrast to the high sensitivity to f_L/f_p in an ac current-biased junction, in an ac voltage-biased junction, the only parameter that determines the step width is $\alpha = eV_{ac}/hf_L$; the two parameters ω_p and β_c do not play any roles in determining the response of the Josephson junction, such as the appearance of certain steps. Even for an ac current-biased junction, as long as the driving frequency is not too close to the plasma resonance frequency, the behavior of the junction will not be too sensitive to f_L/f_p. In our case, from

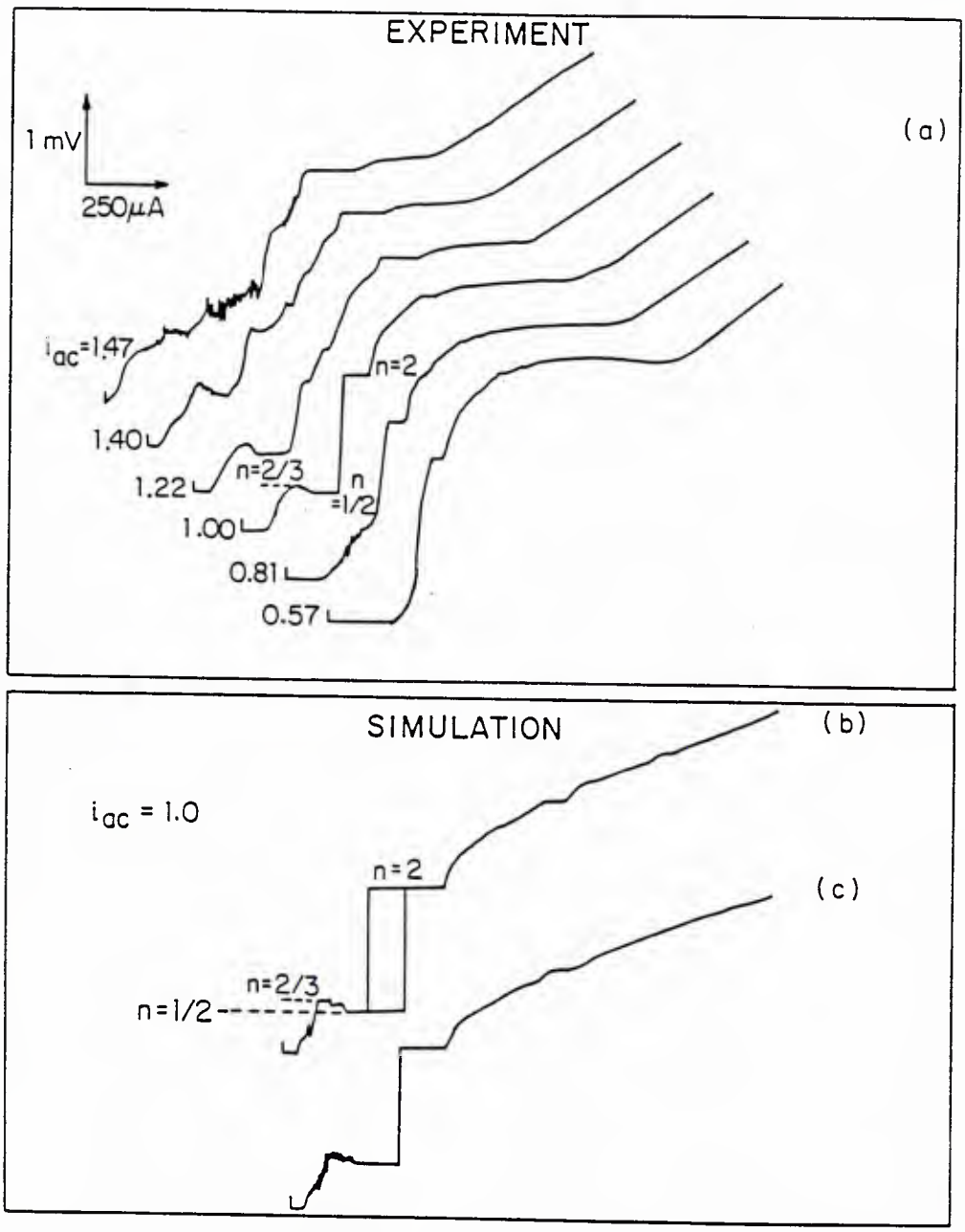

Fig. 5.3 (a) I-V curves of the SNAP2 junction irradiated with 419 GHz radiation. The distinctive feature of the I-V curve with i_{ac}=1.0 is the appearance of the 1/2 step with a little bump on the left edge. (b) Simulated I-V curve with f_L/f_p=0.97 and i_{ac}=1.0. (c) The same as (b) except adding a 20K white Gaussian noise. Note the strong resemblence to the experimental curve, i_{ac}=1.0, in (a).

the estimated capacitance value, we know that the drive is near the resonance, so a small difference in f_L/f_p can cause significantly different behavior.

5.3 Analysis of I-V characteristics.

By using the analog simulator described in Chapter IV, we scanned f_L/f_p and i_{ac}, making I-V curves for comparison with experiment. At $f_L/f_p = 0.97$ and $\beta_c = 24$ below the gap (and 2.8 above the gap) we found that the I-V curves showed the 1/2 and the 2nd steps in the ac current range between $i_{ac} = 0.85$ to $i_{ac} = 1.20$. The simulated curve with i_{ac}=1.0 is shown in Fig. 5.3b. As the dc current is increased from zero, the junction jumps out from the zero voltage step and phase locks to the 2/3 step for a short range of dc current, then for higher dc current the junction goes down to a lower voltage state on the 1/2 step. The Poincaré section map and the power spectrum show that there is no other phase-locking region in the transition range from the 2/3 to the 1/2 step; the system has gone through either chaotic or quasiperiodic states.

5.3.1 The Importance of Added Noise

The noticeable discrepancies between the simulation in Fig. 5.3b and the corresponding experimental curve for $i_{ac} = 1.0$ in Fig. 5.3a, namely, an actual step at n=2/3 and hysteresis between the n=1/2 and n=2 steps, are typical for noise free simulations. We should expect these discrepancies to be removed by the addition of noise to the simulation.

The little piece of the 2/3 step is destroyed by a noise current equivalent to a white noise of 5K defined by Eq. (4.24), but the hysteresis takes much more noise to be removed. We found that we need to put 20K of noise into the simulation to barely suppress the hysteresis. If we add more than 20K of noise, the left corner of the 2nd step will become noisy, indicating that some noise-triggered down switching is happening. Then if we take a long enough averaging time, the noisy corner will be replaced by a

smooth rounded corner, which is not we saw in the experiment. (For example, the curve with $i_{ac} = 1.0$ in Fig. 5.3a has a very sharp corner at the left edge of the 2nd step.) Thus we pick the simulated curve with 20K of noise to compare with the experimental ones.

From the argument given in section 2.4, this 20K of noise is equivalent to 20/3≈6.7K of noise in the real experiment due to the large difference in the number of averaging cycles in the simulation and experiment. Keep in mind that we are working at far-infrared frequency range where both the photon energy $\hbar\omega$ and the induced step voltage level eV are comparable to the thermal energy $k_B T$. We have to use the complete form of noise formula including both shot noise at finite voltage steps and the quantum fluctuationas at high frequencies. From ref. (46), the power spectrum of the current noise is

$$S(V, \omega, T) = \frac{e}{2\pi}\left[I_{qp}(V+\hbar\omega/e)\coth(x/2) + I_{qp}(V-\hbar\omega/e)\coth(y/2)\right] \qquad (5.2)$$

$$x = \frac{eV+\hbar\omega}{k_B T}, \qquad y = \frac{eV-\hbar\omega}{k_B T}$$

The integration of $S(V, \omega, T)$ over the bandwidth $(0, \infty)$ gives the square of the noise current

$$\langle \delta I^2 \rangle = \int S(V, \omega, T)\, d\omega$$

For the piecewise nonlinear resistance model, if

$$| V \pm \hbar\omega/e | < V_g$$

which is the case the current discussion addresses, then

$$I_{qp}(V \pm \hbar\omega/e) = \frac{V \pm \hbar\omega/e}{R_{leak}}$$

and (5.2) reduces to

$$S(V, \omega, T) = \frac{k_B T}{2\pi R_{leak}}\left[x\coth(\frac{x}{2}) + y\coth(\frac{y}{2})\right] \qquad (5.3)$$

It is difficult to build an analog noise source which has such a complicated voltage and frequency dependence. What we can do is to replace this frequency and voltage dependent noise source by a white noise source with an effective noise temperature T_{eff}, whose power density equals $S(V_{dc}, \omega_o, T)$, where V_{dc} is the average voltage at the part of the I-V curve concerned, and the fixed frequency value ω_o is chosen to be that at which the noise affects the system most. Then

$$T_{eff} = \frac{T}{4}\left[x_o \coth\left(\frac{x_o}{2}\right) + y_o \coth\left(\frac{y_o}{2}\right) \right] \qquad (5.4)$$

$$x_o = \frac{eV_{dc} + \hbar\omega_o}{k_B T}, \quad y_o = \frac{eV_{dc} - \hbar\omega_o}{k_B T}$$

This result will reduce to simpler forms in three limits:

1) Thermal noise limit.

$$|x_o| << 1, \quad |y_o| << 1$$

then $$T_{eff} = T \qquad (5.4a)$$

2) Shot noise limit.

$$x_o >> 1, \quad y_o >> 1$$

then $$T_{eff} = T \times [x_o + y_o]/4 = eV_{dc}/2k_B \qquad (5.4b)$$

3) Zero point fluctuation limit (blue noise).

$$\hbar\omega_o > eV_{dc}, \quad |x_o| >> 1, \quad |y_o| >> 1$$

then $$T_{eff} = T \times [x_o - y_o]/4 = \hbar\omega_o/2k_B \qquad (5.4c)$$

To study the noise effect on the 1/2 step, it is reasonable to assume V_{dc} in (5.4) as the voltage at the 1/2 step. But the determination of the frequency ω_o needs more investigation. Naturally, we would guess that the noise at the plasma resonance frequency ω_p would affect the system most. If we replace ω_o by $\omega_p = 2\pi \times 400\text{GHz}$ in (5.4), we will have

$$T_{eff} \approx \hbar\omega_p / 2k_B T \approx 9.6\,\text{K}$$

This will correspond to $T^* \approx 3T_{eff} \approx 29K$ of noise in the simulation, which is higher than the value ($T^* \approx 20K$) we actually found to be neccessary in the simulation. That is unreasonable, because this T* should be the minimum noise in the experimental system. Any extraneous noise, such as the 300K room temperature blackbody radiation going through the window, can only make the actual noise in the system higher than this T*.

Trying to solve this puzzle, we have investigated at what frequency the noise power affects the system most. We did this by replacing the white noise current by a sinusoidal current whose amplitude i'_{ac} and frequency ω could be varied. By increasing the amplitude of this ac current, we can decrease the hysteresis shown in Fig. 5.3b. We define a threshold value i^T, at which the hysteresis just disappears. In Fig. 5.4, we plot i^T vs. the frequency ω of that perturbing current. The result is rather surprising and interesting. Instead of at ω_p, the threshold i^T has its minimum value around $\omega_p/3$, and increases very sharply when $\omega > \omega_p/2$. This means the noise at the frequency around $\omega_p/3$ is most effective in removing the hysteresis, while the noise above $\omega_p/2$ has little effect. The curve in Fig. 5.4 is quite similar to the chaos threshold curve in Fig. 4.7, even though the thresholds are defined in quite different ways. The frequency for minimum i_{ac} of seeing chaos is about $(2/3)\omega_p$, while in this case the frequency corresponding to the minimum i^T is $(1/3)\omega_p$. Notice we are studying the voltage at the 1/2 step, where the oscillation frequency is $(1/2)f_L \approx (1/2)f_p$; that might explain the factor-of-two difference. Whether this 1/3 factor in both cases is purely a coincidence or has some general scaling nature behind it remains to be answered.

Now if we assume $\omega_o=(1/3)\omega_p$ in (5.4), for T=4.2K, we get the effective noise temperature

$$T_{eff} = 5.5\,K$$

which is only 1K below the value deduced from simulations. This is not bad at all considering all the simplifications we made in (5.4) to obtain this value. A small amount of

extraneous noise could account for the small remaining discrepancy.

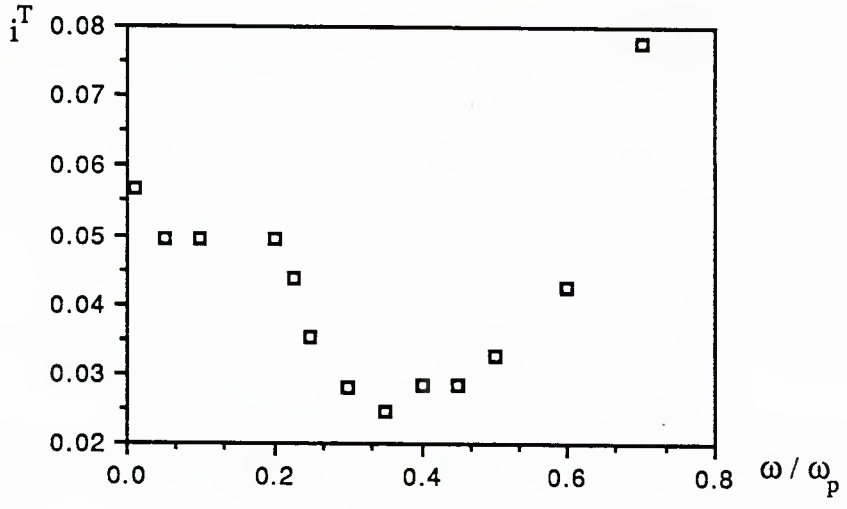

Fig. 5.4

Threshold of current amplitude of perturbation required to remove the hysteresis of the I-V curve in Fig. 5.3(b) as a function of frequency.

The agreement between the data and the simulated I-V curve with the appropriate T* (Fig.5.3c) is impressively good. The phase lock of the little piece of the 2/3 step is totally destroyed while leaving the 1/2 step almost unchanged. This little piece of the destroyed 2/3 step forms the small bump at the left edge of the 1/2 step, resembling that seen in the experimental I-V curve. The fact that the simulated I-V curve is noisier than the experimental ones is another consequence of the fact that we average over relatively fewer cycles (10^4) in the simulations. By contrast, in the experiment, all except extremely low-frequency fluctuations are averaged out over 10^{12} drive cycles.

5.3.2 Determination of ω_p

As we increase the frequency ratio f_L/f_p from 0.97 in the simulation, the little piece

of the 2/3 step in Fig. 5.3b becomes bigger and bigger while the lower 1/2 step becomes smaller and smaller. At the value $f_L/f_p = 1.03$, the 1/2 step is totally gone and replaced by either the 2/3 step or some noisy phase-unlocked motion. As we increase f_L/f_p further, the 2/3 step extends further and further to the right. Fig. 5.1b shows the simulated I-V curve with f_L/f_p=1.07, and i_{ac}=1.0. It has the distinctive feature of the 2/3 + 2nd steps, the "fingerprint" of the SNAP1 junction.

We have studied quantitatively in what parameter ranges those fingerprints might appear. First, we found that the appearance of these features are not too sensitive to β_c. We can change β_c by 50% or more but keep the "fingerprint" unchanged. So we chose a β_c value of 3.4 and 28 by using R_n and R_{leak}, respectively, which is close to the estimated experimental one. Then we scanned the two parameters f_L/f_p and i_{ac} in a noiseless simulation. Since the unique feature of each junction is the successive appearance of 2/3 + 2nd steps or 1/2 + 2nd steps, we focused on the regions in f_L/f_p-i_{ac} plane, in which the 1/2 or 2/3 plus 2nd step appears on the dc I-V curves. Taking advantage of the slowness of the simulator, we can monitor the time evolution of the phase ϕ, as we sweep the dc bias current. It is very easy to distinguish a phase-locked step from a phase-unlocked running state by monitoring the Poincaré section of the ϕ–ϕ map. Thus we define a step such that in a noticeable dc current range (the minimum resolution is roughly 1% of the critical current I_c), the phase motion is periodic with the same period in the entire range. In Fig. 5.5, we plot a state diagram in f_L/f_p-i_{ac} plane. The horizontally shaded area is the region where we can see only the 2/3 + 2nd steps, the vertically shaded area is that for the 1/2 + 2nd steps, while the doubly shaded area within the contour is that for the combination of the 2/3+1/2+2nd steps, which is what we believe to be the fingerprint of the SNAP2 junction. Even with the loose criterion on step size stated above, this contour includes a narrow range in f_L/f_p, namely, $0.87 < f_L/f_p < 1.02$ but a rather large range in i_{ac}, $0.8 < i_{ac} < 1.25$. But we know in the experimental data, the maximum size of the 2/3 step for SNAP1 and

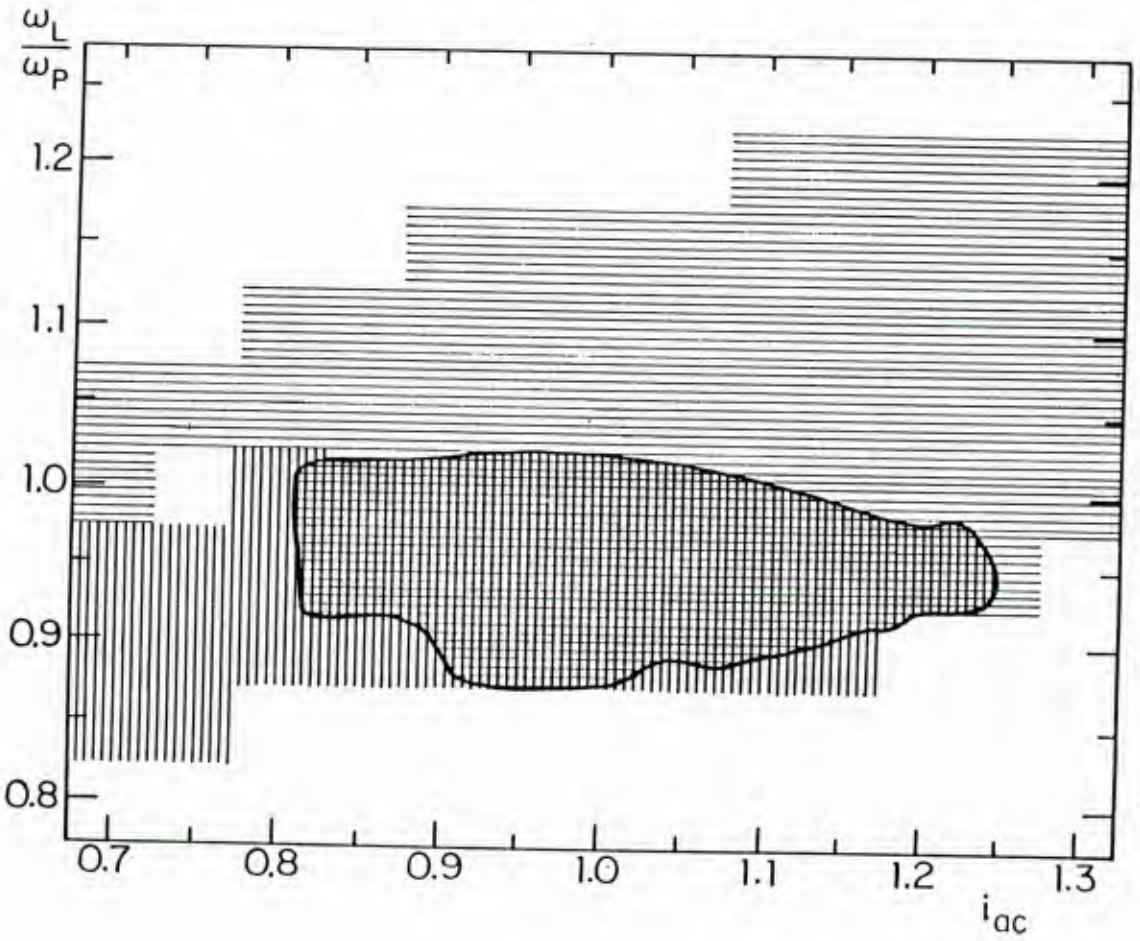

Fig. 5.5 Approximate state diagram in i_{ac}- ω_L/ω_p plane. The horizontally shaded area is the region where we can see the 2/3+2nd steps, the vertically shaded area is that for the 1/2+2nd steps, the doubly shaded area is that for the 2/3+1/2+2nd steps, and the blank area is the region where we can see none of the above sequences of features seen in the experimental I-V curves.

the 1/2 step for SNAP2 is about 30% of I_c. By applying this more restrictive criterion plus other features of the I-V curves taken at other laser power levels, we can narrow down the range in i_{ac} substantially and determine the f_L/f_p ratio for SNAP2 to be 0.97±0.04. By contrast, for SNAP1, f_L/f_p=1.07±0.04.

To further verify the assumption drawn from the simulations that the qualitatively different behaviors of the two junctions are indeed caused by the difference in their critical current densities, we applied a magnetic field to reduce controllably the critical current density of SNAP2, which has been assumed to be higher than that of SNAP1. Fig. 5.6 shows a series of I-V curves taken at the laser power level corresponding to i_{ac}≈1.0. The measured critical current is decreased successively from the top to the bottom trace. Assuming the frequency ratio f_L/f_p = 0.97 for the curve on the top, we scaled the ratio for the other curves as $f_L/f_p = [\ 520 / I_c(\mu A)\ ]^{1/2} \times 0.97$. As f_L/f_p increases from 0.97, we can see that the 1/2 step shrinks, and then totally disappears at f_L/f_p=1.03. At I_c = 430μA, corresponding to f_L/f_p=1.07, which is what we believe the ratio for SNAP1, the I-V curve has the fully extended 2/3 step right below the 2nd step, just like the I-V curve of SNAP1. In fact, all the quantitative features of this I-V curve such as the width of the Josephson steps are essentially the same as those of SNAP1. (See Fig. 5.1(a), the curve with i_{ac}=1.0 and the inset for comparison.) Since the ratio f_L/f_p = 1.07 corresponds to I_c = 430 μA, which is the same as SNAP1, we can conclude that the area difference between the two junctions is less than a few per cent, as might be expected from their similar fabrication. This experimental evidence definitely proves that a 10% difference in the plasma frequency is indeed the cause of the qualitatively different behaviors of the two similar junctions driven at the same FIR frequency.

5.3.3 Calibration of i_{ac}

In order to calibrate the experimental i_{ac} accurately, we compared a set of I-V curves taken at different laser power levels ranging from 1 to 50 (measured in an arbitrary

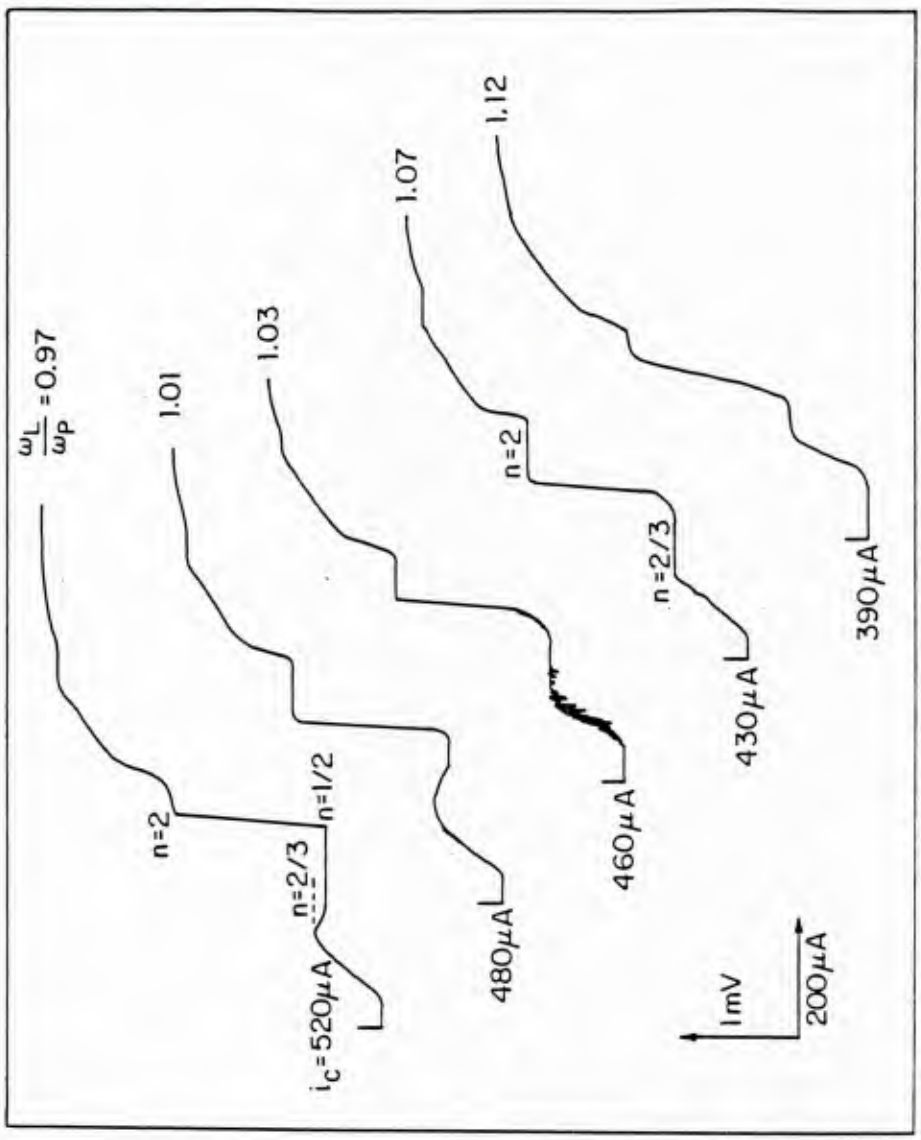

Fig. 5.6 Experimental I-V curves of the SNAP2 junction irradiated at 419 GHz. All the I-V curves are taken at about the same level of laser power corresponding to i_{ac}=1.0. From the top to the bottom, the critical current is magnetically suppressed successively; thus the ratio ω_L/ω_p is increased successively. Note close similarity between the curve at ω_L/ω_p=1.07 and that in Fig. 5.1 for i_{ac}=1.0.

unit) with a set of simulated I-V curves taken at different i_{ac} scaled with the square root of the relative laser power levels. We determined the proportionality factor between i_{ac} and the square root of the laser power by the best fit of all the I-V curves between the two sets. It turns out that if we choose the proportionality factor to make the absolute i_{ac} values those shown in Fig. 5.3a, then all the fits between the two sets of I-V curves are excellent in terms of the qualitative features of the I-V curves. For example, in Fig. 5.7(a), the experimental I-V curve is taken with the highest laser power level available from our laser source, which is 13.9 times higher than that of the one with i_{ac} = 1.0 in Fig. 5.3a; hence i_{ac} is higher by $(13.9)^{1/2}\approx 3.73$. On the experimental I-V curve, the 1st Josephson step is again missing; also there is a negative resistance region at the left corner of the 2nd step. The simulated I-V curve with i_{ac} = 3.73, shown also in Fig.5.7, exhibits similar features. Without added noise (Fig. 5.7b), the state first phase locks onto the 2nd step; as we increase the dc current, it jumps down to the 1st step for a short range of the dc current and then comes back to the 2nd step. Again, we should expect that this sharp structure of phase locking will be removed by some noise. Fig. 5.7c shows a simulated I-V curve with a 40K white noise added on the same bias conditions as in Fig. 5.7b. The phase locking of the little piece of the 2nd and of the 1st step is destroyed by this noise; the resulting rounded corner (in Fig.5.7c)resembles the negative resistance region in the experimental I-V curve. The choice of 40K noise is somewhat arbitrary here, since there is no such a sharp criterion as in Fig. 5.3, where we chose the noise value such that the hysteresis just disappears, which is the case in the experiment. But for the bias conditions in Fig. 5.7, if we add more noise than 40K, even up to 100K, the I-V curves just become more noisy; if we average for a longer time, the resulting smooth curve will have a more rounded corner, but nothing qualitative happens such as the disappearance of the hysteresis in Fig. 5.3. Thus it is hard to identify a specific noise value that best reprocuces the experimental result. But 40±10K seems to be the minimum noise we need to put in todestroy the phase

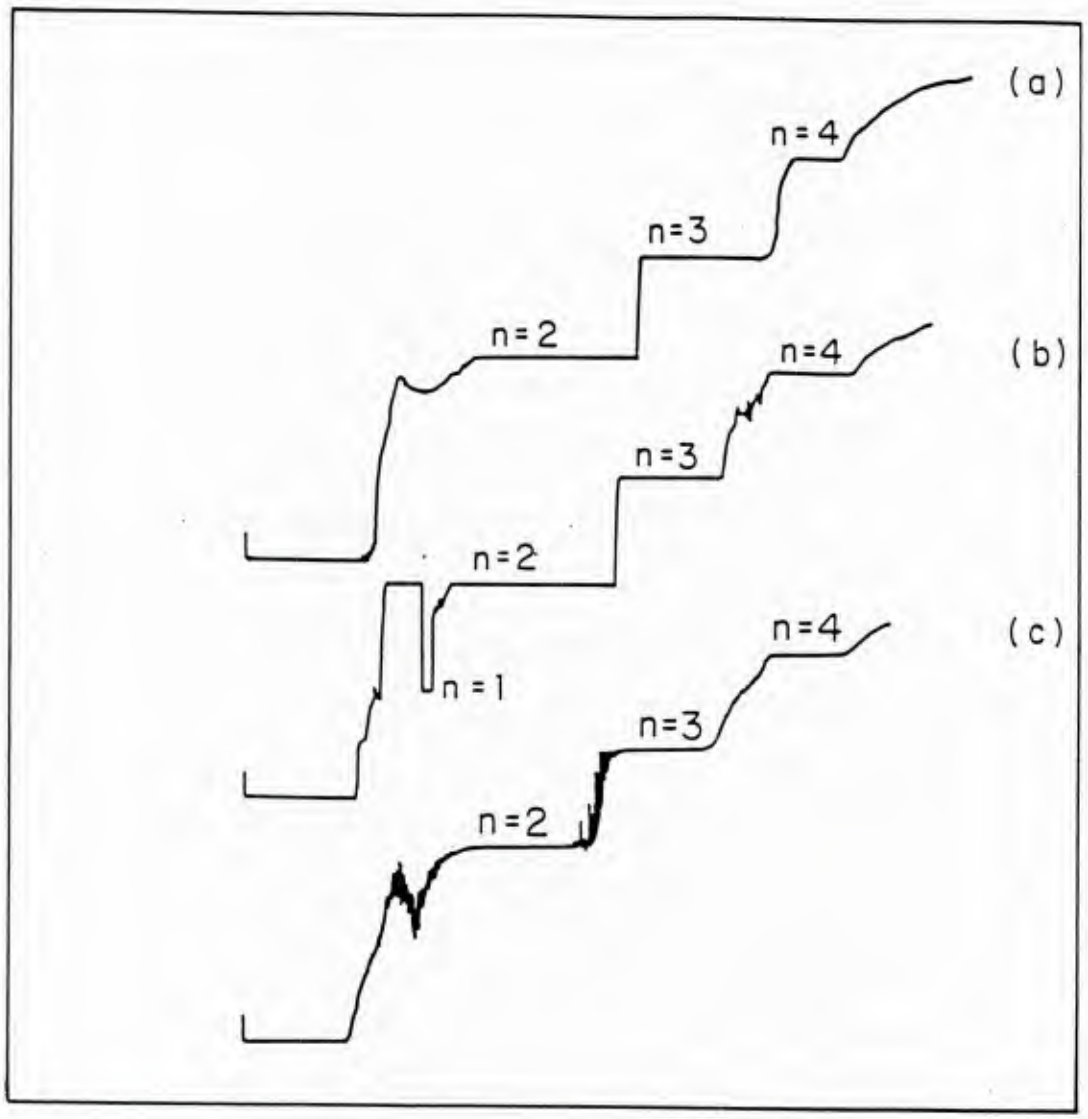

Fig. 5.7

(a) Experimental I-V curve of the SNAP2 junction with a laser power 13.9 times higher than that of one with i_{ac}=1.0 in Fig. 5.3(a). (b) Simulated I-V curve with ω_L/ω_p=0.97 and i_{ac}=3.73. (c) Same as (b) except adding 40K white Gaussian noise.

locking. This higher noise temperature (compared to that in Fig. 5.3) is presumably due to the fact that we are operating at a much higher voltage state (2nd step instead of 1/2 step), so the shot noise is much bigger. We did not make any measurement like that of Fig. 5.4 to identify the frequency ω_0, at which noise affects the system most. The main reason is the umbiguity of defining the threshold i^T. For simiplicity, we just use the ω_0=0 limit of Eq. (5.4), which reduces to the shot noise limit (5.4b) for the voltage at the second step ($x_0 = y_0 \approx 5$). Thus we have

$$T_{eff} \approx 10.3 \text{ K}$$

that gives $T^* \approx 30$K, which is some 30% lower than our result.

Besides the ambiguity in choosing T* discussed above, we have another difficulty to limit a rigorous comparison between the experiment and the simulation. In obtaining the noise calibration formula (4.24), we assumed that the resistance R is linear, and we have been using R_{leak} for R. This assumption is justified when we are considering the 1/2 step; its dc voltage is about 1/6 of the gap voltage, so the system at this step spends all the time below the gap. In contrast, at the 2nd step, the dc voltage is 2/3 of the gap, and due to the strong drive (i_{ac}=3.7), the oscillation amplitude in V(t) is quite large, so the system spends quite a large portion (30-40%) of its time above the gap. Thus we can not just use R_{leak} for R. Qualitatively, we should expect the effective resistance value R should be some kind of combination of R_{leak} and R_n, and $R_n < R < R_{leak}$, so the equivalent noise temperature for given noise current is lower than predicted in (4.24) using R_{leak}.

Fig. 5.8 shows another way of determining the laser induced ac current i_{ac}. The crosses show the measured zeroth step width of SNAP1 vs. the square root of the laser power, while the circles are the zeroth step width in a simulation vs. the ac current with $f_L/f_p = 1.07$. By assuming the degree of reduction of the zeroth step width corresponds to the same i_{ac} in both experiment and simulation, we can thus determine the proportionality factor. We can see from Fig. 5.8 that the fit is consistent over a wide range of i_{ac}. In fact,

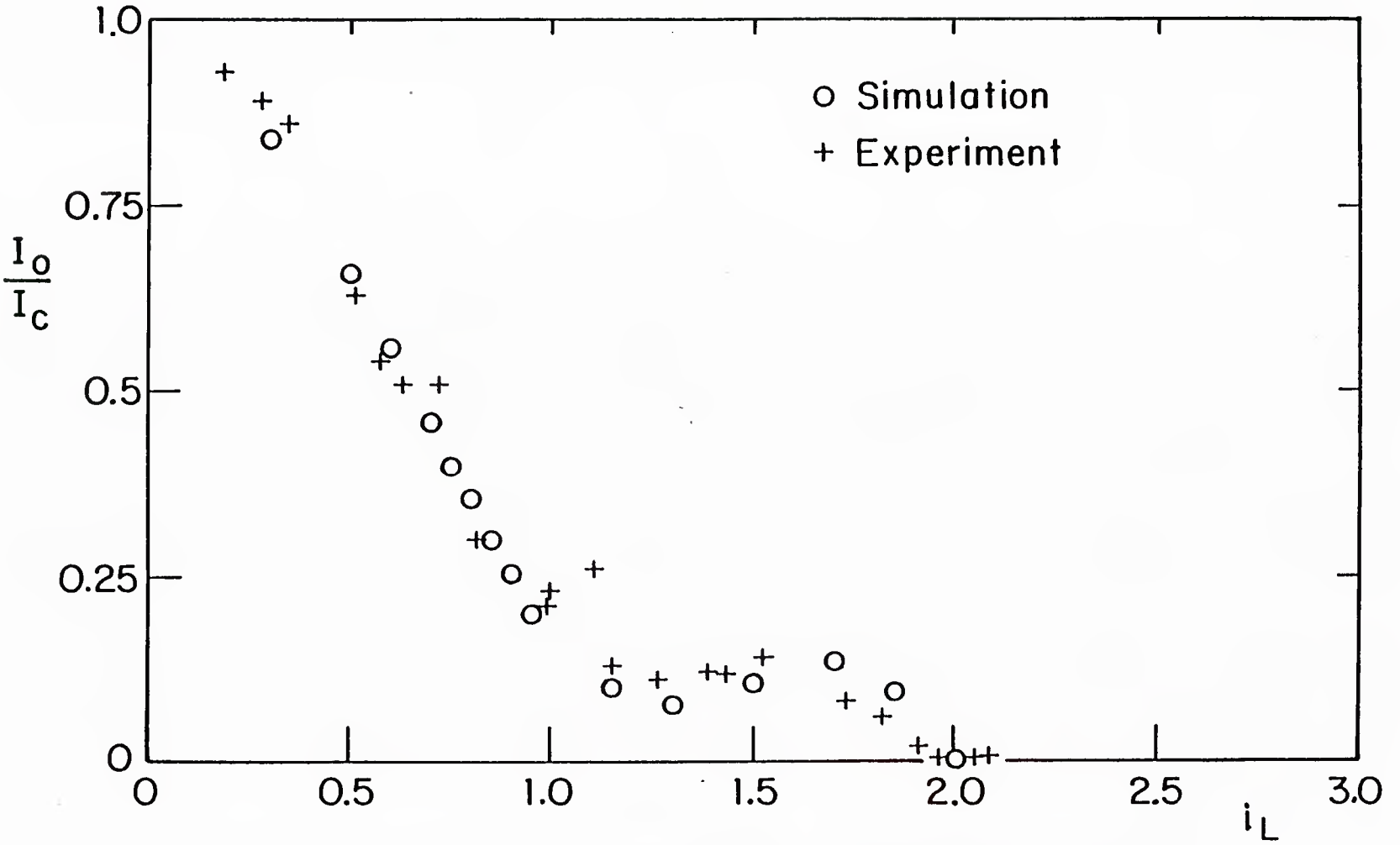

Fig. 5.8 The zeroth Josephson step width vs. i_{ac}(=i_L in the figure) The crosses are the experimental data from the SNAP1 junction and the circles are the simulational ones with f_L/f_p=1.07. Both show a flat knee between i_{ac}=1.0 and i_{ac}=1.5, which is where the 2/3 step appears.

this is the usual way of determining $\alpha=eV_{ac}/\hbar\omega_L$ in all the previous studies,[48,49] where an ac voltage biased RCSJ model is assumed. But this method of fitting has its limitations for a current-biased RCSJ model in a highly nonlinear region. As discussed before, noiseless simulations will not reproduce the experimental results very well, and due to the complicated dependence of T_{eff} on V_{dc} and ω_o in (5.4), the appropriate effective noise temperature T_{eff} varies from part to part as we move along the I-V curve. The only partial exception is the zeroth step, where we can assume the shot noise to be small and at least roughly constant as we change the dc bias current, so we could put a fixed appropriate T_{eff} in the simulation to simulate the experiment. The optimal simulation of the steps at nonzero voltage would need a more complicated noise form.

5.3.4 Experiments at 604 GHz and 245 GHz

We have also studied the response of the junctions to laser radiation at 604 and 245 GHz, where the drive frequencies are not as close to the plasma resonance frequency as at 419 GHz. At 604 GHz, $f_L/f_p \approx 1.5$, chaos is very unlikely to happen (cf. Fig. 4.7). We did not see any chaotic behavior exhibited by any of the four SNAP junctions. But at this value of f_L/f_p, the parameters of the junctions are close enough to the chaotic region that there are very serious deviations between the experimental results and the noiseless simulation. Fig. 5.9 shows step width data taken from another junction, SNAP3, by Danchi et al.[67] It has the parameters: $2\Delta/e = 2.8$ mV, $I_c = 215\ \mu$A, $R_n=7.2\Omega$. Its plasma frequency is $f_p = 390 \pm 20$ GHz. This value is obtained by the study of its reponse to 419 GHz radiation, its fingerprint corresponds to $f_L/f_p=1.07\pm0.05$. The crosses in Fig. 5.9 are the data taken at 1.4K, the dots are those at 4.2K. The circles are the simulated step width in a noiseless digital simulation[67]. The dashed lines are the step widths calculated from Bessel functions, which are derived for an ac voltage-biased junction. The agreement between the simulation and the data at 4.2K is reasonably good for the zeroth and the 2nd steps, but very poor for the 1st step. This indicates that noise and current-bias have more

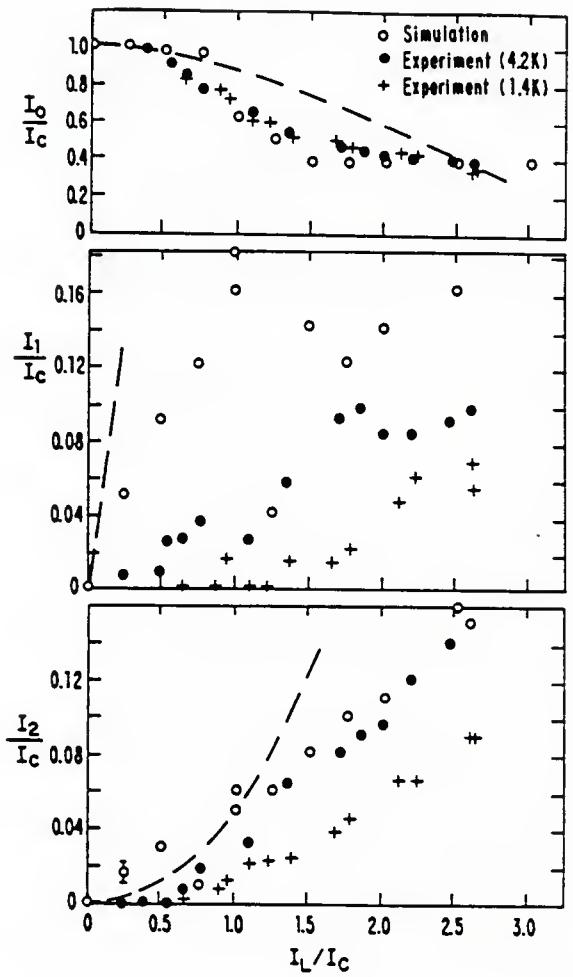

Fig. 5.9

Step width vs. i_{ac} (I_L/I_c in the figure). The crosses are the data taken at 1.4K, the dots are the ones at 4.2K, the circles are the results from noiseless simulations. The dashed lines are the results calculated from Bessel functions. (After Ref. 67)

effect on some steps than on others. In this case, the noiseless simulation shows that the 1st step is hysteretic, a region which is usually more sensitive to noise than the nonhysteretic one, because the noise-induced switching can significantly reduce the step size, while in the nonhysteretic case, the noise reduces the width only through rounding the corners, which is a much less profound effect.

At 245 GHz, $f_L / f_p \approx 0.6$, which should be the easiest region in which to see chaos. We did see chaotic behavior from the junctions we have studied (SNAP1 and SNAP2). In fact, it was the very reproducible noisy steps seen at 245 GHz from SNAP1 that first made us suspect that we were studying a junction in a chaotic regime. But due to the off-resonance of the dipole antenna at this frequency (see Fig. 3.7), and the rich chaotic phenomena observed at 419 GHz, we did not devote much effort to studying the quantitative behavior of the junctions at 245 GHz, and no data are reproduced here.

5.4 Effect of noise in a fractal basin boundary regime.

From the discussions in the previous section, we know that an intrinsically random noise source has very profound effects on a Josephson junction. It is essential to include an appropriate amount of noise in any simulational attempt to reproduce the experimental results. We also notice that noise has different effects on different parts of I-V curves. At certain parts, noise has very noticeable effects, such as washing out hysteresis and destroying an otherwise phase-locked step. At other parts, however, noise has little noticeable effect. This section addresses the effects of noise in a highly nonlinear but not intrinsically chaotic region (the basin boundary of attraction is fractal) compared to an intrinsically chaotic region.

Fig. 5.10 shows a series of phase orbits taken in a noiseless simulation at f_L/f_p=1.07, i_{ac} = 1.50 and at different values of i_{dc}. It is suggested that the reader refer back to Fig. 5.1 to look at the experimental I-V curve with i_{ac} = 1.49. The system starts phase-locked on the zeroth step for small i_{dc}, then becomes phase-unlocked as i_{dc} increases to $i_{dc}\approx$0.14 (I_c=425μA), forming a noisy ramp. Fig. 5.10 a)-f) shows a series of successive simulated phase orbits taken as i_{dc} increases. The bright spots in the pictures are the Poincaré sections, *n* bright spots correspond to period *n* bifurcation. As i_{dc} increases, we can see that the system went into chaos through a period-doubling bifurcation sequence. At i_{dc} = 0.15, the Poincaré section exhibits a strange attractor. Even in the absence of noise, the motion of the system is random.

The I-V curve in Fig.5.1 with i_{ac} = 1.0 shows a similarly noisy ramp as that of the one with i_{ac} = 1.5, but the noiseless simulated I-V curve with i_{ac} = 1.0 shown in the inset does not show any chaotic behavior in the region between the zeroth and the 2/3 steps. Instead, the I-V curve is hysteretic in that region. This indicates that the system is bistable in the dc bias range $0.13 < i_{dc} < 0.18$. The state in which the system will end depends on the initial conditions, specifically in which basin of attraction the system

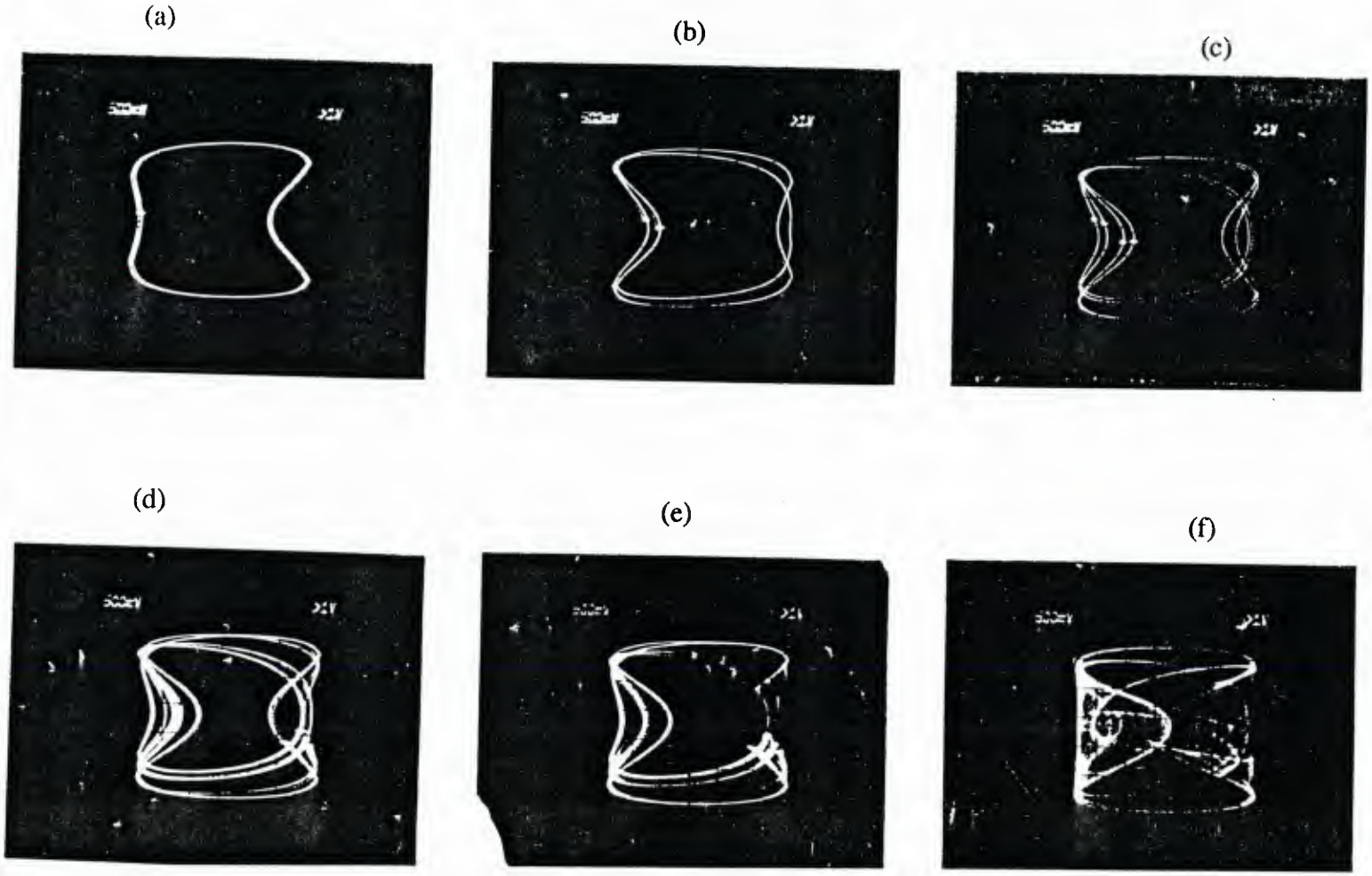

Fig. 5.10 Phase orbits and Poincaré sections (bright spots) from noiseless analog simulation with i_{ac}=1.5 and f_L/f_p=1.07. As i_{dc} changes from 0 to 0.15, the system goes into chaos through a period-doubling bifurcation. The values of i_{dc} are: (a) 0, (b) 0.06, (c) 0.09, (d) 0.10, (e) 0.11, (f) 0.15.

started. Fig. 5.11 shows digitally computed basins of attraction. Under the bias conditions $i_{ac} = 1.0$, $i_{dc} = 0.15$, there are two attractors: the zeroth step and the 2/3 step, or one solution with a period of one drive cycle, the other one with a period of 3 drive cycles.

Fig. 5.11 divides the phase space region [$-\pi < \phi < \pi$, $-\pi < \phi < \pi$] into a 200×200 grid. The RCSJ equation (with $i_n = 0$) was solved for each initial condition on the grid and, after an initial transient, the system converges on one of the two phase-locked solutions. If the system converged on the first, corresponding to a zeroth-step solution (V_{dc}=0), a black square was plotted; if the system converged on the second, corresponding to $V_{dc} = (2/3)\ (hf_L/2e)$, the 2/3 step, a white square was plotted. Thus, the black and white regions in Fig. 5.11 compose the two basins of attraction. The basin boundary has a very complicated fractal structure, indicating the high sensitivity of the system to the exact initial conditions. It is intuitively plausible that this high sensitivity to the initial conditions corresponds to a high sensitivity to noise when noise is added in the simulation, because noise can be treated in some aspects as a certain amount of uncertainty in the initial conditions.

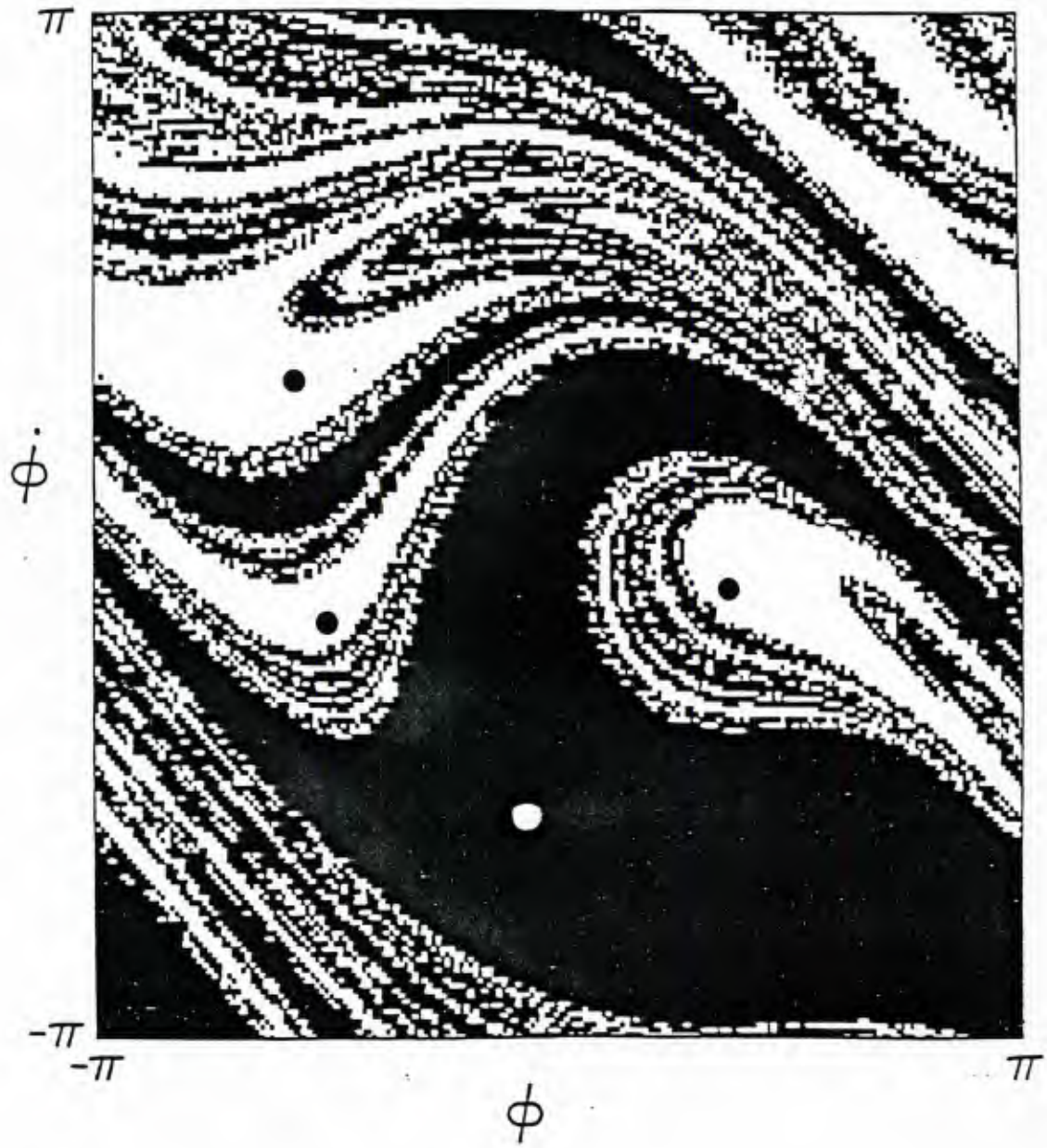

Fig. 5.11 Basins of attraction for i_{ac}=1.0 and i_{dc}=0.15. The white region is the basin of the 2/3 step solution, corresponding to the three-point Poincaré section indicated by the centers of the black circles. The black region is the basin of the zeroth-step solution, with one-point Poincaré section (white circle). No noise is included.

Grebogi et al.[68] derived a formula relating the noise sensitivity to the fractal structure of the basin boundaries. Consider the simple two-dimensional phase space diagram, schematically depicted in Fig. 5.12. There are two possible final states ("attractors") denoted A and B. Initial conditions on one side of the boundary, Σ, eventually asymptote to B, while those on the other side of Σ eventually go to A. The region to the left (right) of Σ is the " basin of attraction" for attractor A (or B) and Σ is the "basin boundary".

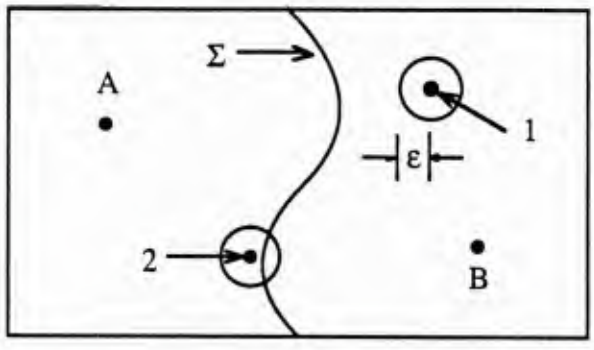

Fig. 5.12

A region of phase space divided by the basin boundary Σ into basins of attraction for the two attractors A and B. *1* and *2* represent two initial conditions with uncertainty ε.

If the initial conditions are uncertain by an amount ε, then, (cf. Fig. 5.12) for those initial conditions within ε of the boundary, we can not say a priori to which attractor the orbit eventually tends. For example, in Fig. 5.12, *1* and *2* represent two initial conditions with an uncertainty ε. The orbit generated by initial condition *1* is attracted to attractor B. Initial condition *2*, however, is uncertain in the sense that the orbit generated by *2* maybe attracted either to A or B. In particular, consider the fraction *f* of the volume of the uncertain phase space over the whole phase space. For the case shown in Fig. 5.12,

we clearly have $f \sim \varepsilon$. However, if the basin boundary is fractal, the scaling can be quite different.

It is very useful to introduce the concept of dimension of a fractal dimension d.[69] It can be defined equivalently in several ways. Grebogi et al. used the capacity definition of dimension:

$$d = \lim_{\delta \to o} \frac{\ln N(\delta)}{\ln (1/\delta)} \tag{5.5}$$

where $N(\delta)$ is the minimum number of D dimensional cubes of side δ needed to cover the basin boundary. In a extreme case, where the boundary is a smooth curve, then

$$N(\delta) \sim \delta^{D-1} \tag{5.6}$$

thus

$$d = D - 1 \tag{5.7}$$

But in general, $d > D\text{-}1$. The larger d is, the larger fraction of the space is occupied by boundaries, and the more complicated the fractal structure is. Quantitatively, the total number of cubes of side δ in the whole space is

$$N_{tot} \sim \delta^{-D} \tag{5.8}$$

Combining with (5.5), we have the fraction of the space composed by boundaries given by

$$f \sim \frac{N(\delta)}{N_{tot}(\delta)} \sim \delta^{D-d} \tag{5.9}$$

If we choose the side of the cube δ being the uncertainty in the initial conditions ε, then

$$f \sim \varepsilon^{D-d} \tag{5.10}$$

What (5.10) indicates is that the fraction of the uncertain region in phase space is scaled to the initial uncertainty ε through a power law. In the case $d \approx D$, in which the whole phase space is occupied by boundaries, f can be a finite value no matter how small the uncertainty in the initial conditions is. Clearly, a high fraction f corresponds to high noise

sensitivity; thus the noise sensitivity is related to the dimension of the basin boundary d in such a way that higher d causes higher noise sensitivity. This conclusion is strongly supported by the experimental data shown in Fig. 5.13.

Fig. 5.13(d) is the dimension of the basin boundary (from digital simulations) vs. dc bias current. Its peak takes place at $i_{dc} \approx 0.16$, and the peak value is quite close to 2. The curve in Fig.5.13(e) is the noise output from SNAP1 measured on a PAR124 lock-in amplifier in the ac voltmeter mode at 10 kHz with a 10% bandwidth. From Fig. 5.13 (d) and (e), it is clear that the variation in the experimental noise output in the region studied corresponds qualitatively to the variation of the calculated fractal basin boundary dimension with i_{dc}, as expected on the basis of the above argument, given thermal and shot noise (or extraneous noise) inputs in the experimental system. No values of d are shown in Fig. 5.13(d) for $i_{dc} > 0.3$, since no sensitive dependence on initial conditions (i.e. no fractal basin boundary) was observed in the simulations. The two other noise peaks displayed in Fig. 5.13(e) (at $i_{dc} \sim 0.45$ and ~ 0.62) are associated either with intrinsic chaos or noise amplification due to high dynamic resistance of the I-V curve.

Our basin-boundary study thus provides a mechanism to explain the high experimental noise values in the non-intrinsically chaotic regions. To obtain the phase-space motion of the system and a measure of the concomitant noise, we reverted to digital simulations. Noise was first introduced in the calculations as a white Johnson noise source. Every simulation was begun with the system at a very high noise temperature (T~1000K) and then gradually "annealed" until the desired temperature range was reached; this annealing process is added to make the simulation results independent of the initial conditions chosen. After we waited for some additional cycles to discard initial transients, the Poincaré section and the power spectrum of the solution were calculated over at least 3200 cycles, with a time step of one-thousandth of a drive cycle.

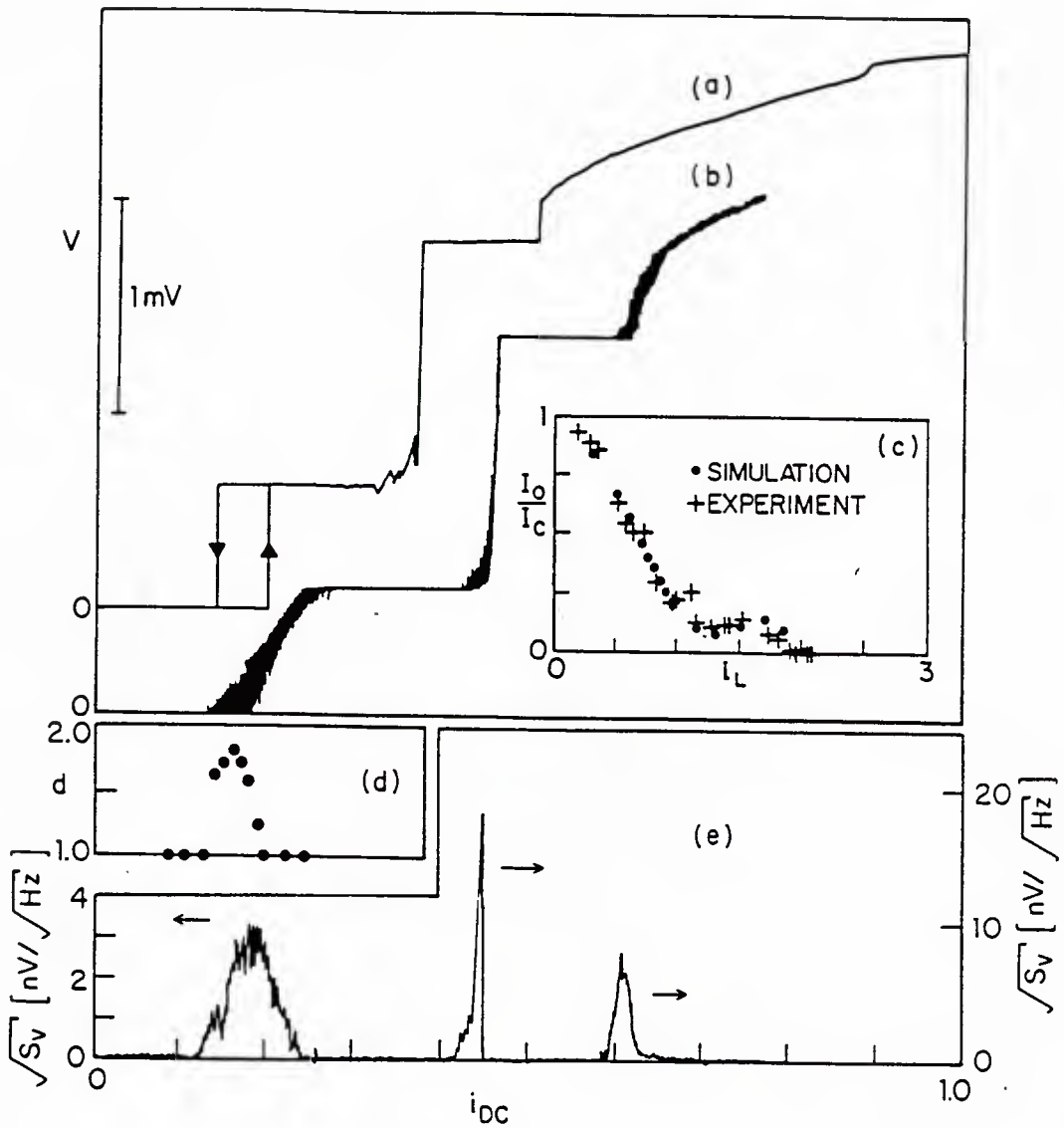

Fig. 5.13

The measured noise density and the calculated dimension of basin boundary vs. dc bias current. (a) Simulated and (b) experimental I-V curves. (c) Dependence of the critical current on the laser drive. (d) Computed basin boundary dimension and (e) experimental noise power measurements at 10 kHz as a function of dc bias. Curves (a) and (b) and plots (d) and (e) are all for i_{ac}=1.0 and share the same horizontal scale.

The Poincaré section of Fig. 5.14(a) shows the behavior in a fractal basin boundary regime. If only a small amount of noise (T=1K) is added to the system, the motion is still essentially periodic and qualitatively similar to the case with no added noise, depicted in Fig.5.11 by black circles; the orbit is still well within the basin of attraction of the 2/3 step. If we add more noise, the nature of the orbit becomes very different, as shown in Fig. 5.14(b). The resulting Poincaré section is stretched out anisotropically, reproducibly filling in a complicated region of phase space. It is very similar to the Poincaré section for an intrinsically chaotic regime, displayed in Fig. 5.14(c) and (d), which shows an extended strange attractor even in the absence of noise (Fig. 5.14(c)). Adding 50K of noise does not change the Poincaré section qualitatively in this case. One may conclude that noise does not have profound effects on intrinsic chaos. Also, from the similarity between Fig. 5.14 (b) and (d), we may draw a conclusion that it is difficult if not impossible to distinguish noise-induced chaos from intrinsic chaos in an experiment. In general, we found a great similarity in all the Poincaré sections calculated for experimentally noisy regimes (both intrinsically and non-intrinsically chaotic regions) as long as the effect of noise (T>5K) was included, providing a plausible explanation for the comparable noise values observed experimentally in all the noisy regions.

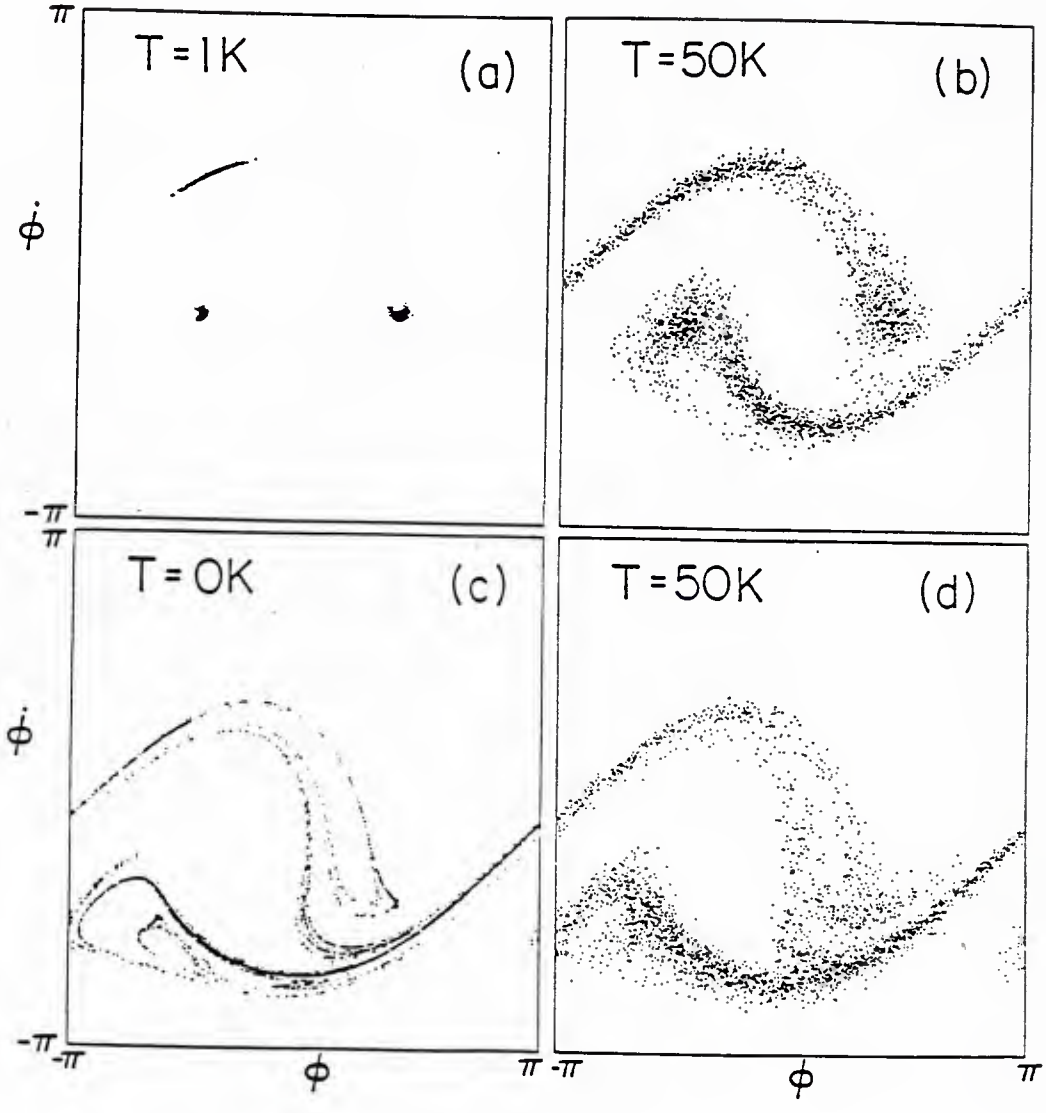

Fig. 5.14

Effect of added noise on the Poincaré sections for the system:

(a), (b) in fractal basin boundary regime at i_{dc}=0.18 and i_{ac}=1.0, and (c), (d) in an "intrinsic" chaotic regime at i_{dc}=0.15 and i_{ac}=1.5.

5.5 Power spectrum of noise-induced intermittency.

The power spectrum of the solutions in the fractal basin boundary regime show noise-induced intermittency leading to large low-frequency noise. This is shown in Fig.5.15, where the spectrum is approximately 1/f for at least two frequency decades over a wide noise temperature range. (The peak at $f_L/3$ reflects the residual effect of the period-three phase lock.) Such behavior is not uncommon in the parameter region investigated here. The occurrence of switching and excess low frequency noise has a rather well-defined threshold noise temperature for a simulation of given length. The Poincaré section for 5K is still localized within the basin of attraction of the 2/3 step solution but comes very close to the boundary. A small increase in the added noise pushed the orbit out into the basin boundary. This causes sudden changes in the Poincaré section as shown in Fig. 5.14(b), which begins to resemble a strange attractor. And correspondingly, the power spectrum of the solution develops excess low-frequency noise. The situation is qualitatively similar to an interior crisis[68] occuring in intrinsic chaotic systems, in the neighborhood of which an intrinsic approximately 1/f power spectrum was found[70].

If shot noise is included in the calculations, similar results are obtained. However, the 1/f power spectrum now holds down to T=0, since the magnitude of the added noise bottoms out at a finite value, corresponding to a Johnson noise temperature of the order of 5K at the 2/3 step. So experimentally, it will not make much difference if we cool down from 4.2K to 1.4K; the noise-induced chaos will occur at both temperatures. In fact, the experimental data taken at 4.2K and 1.4K are quite similar in terms of noisy I-V curves and noise power density.

However, the power spectra measured from our analog simulations under similar bias conditions as that of the digital simulations are in general Lorentzian. One of them is shown in Fig. 5.16. The junction is biased at $i_{dc} = 0.17$, $i_{ac} = 1.0$, and $f_L/f_p = 1.07$. The amplitude of the noise current corresponds to 50K thermal noise for the SNAP1 junction.

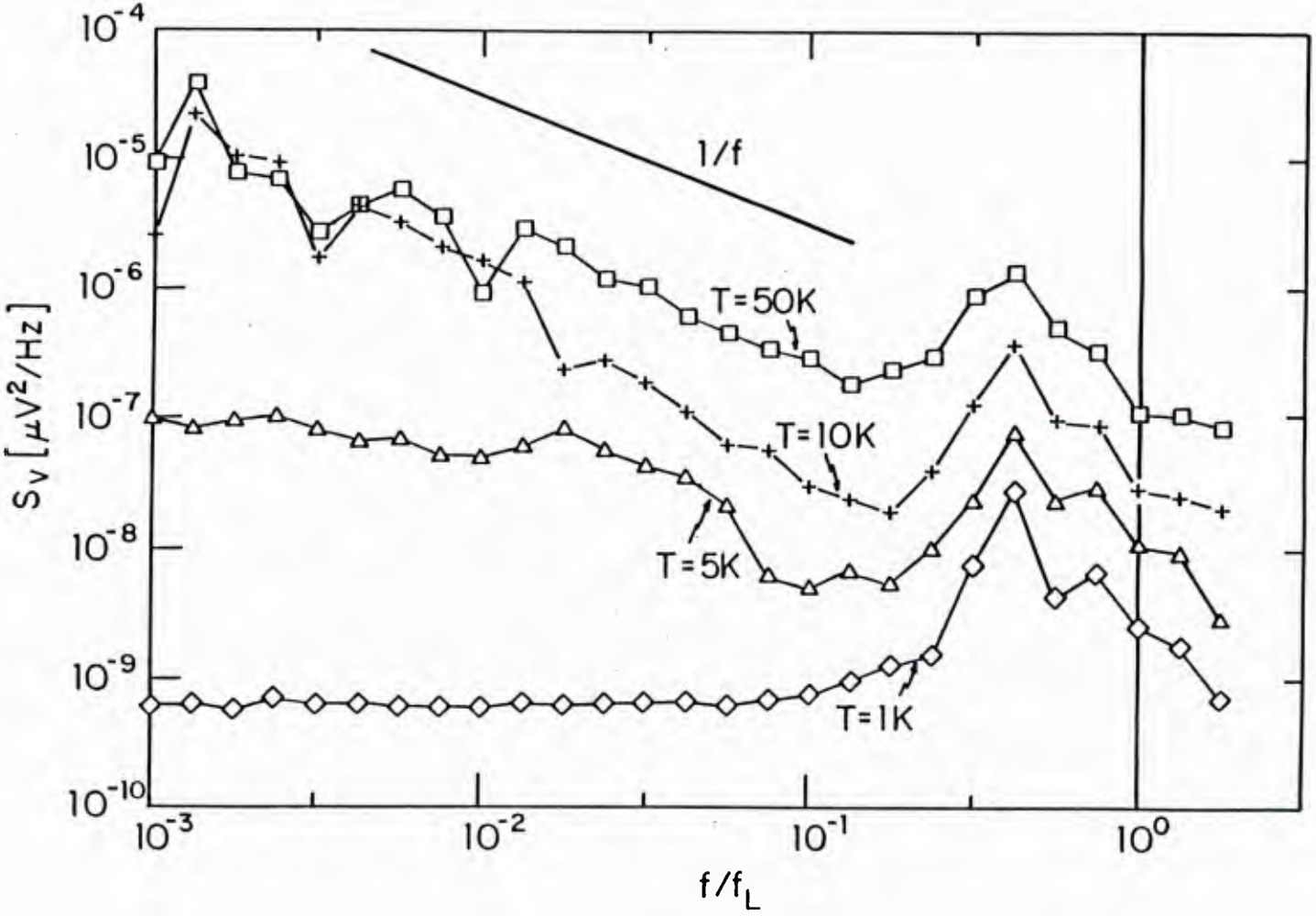

Fig. 5.15 Effect of added noise on the power spectra calculated from the digital simulations. Parameters are i_{dc}=0.18 and i_{ac}=1.0.

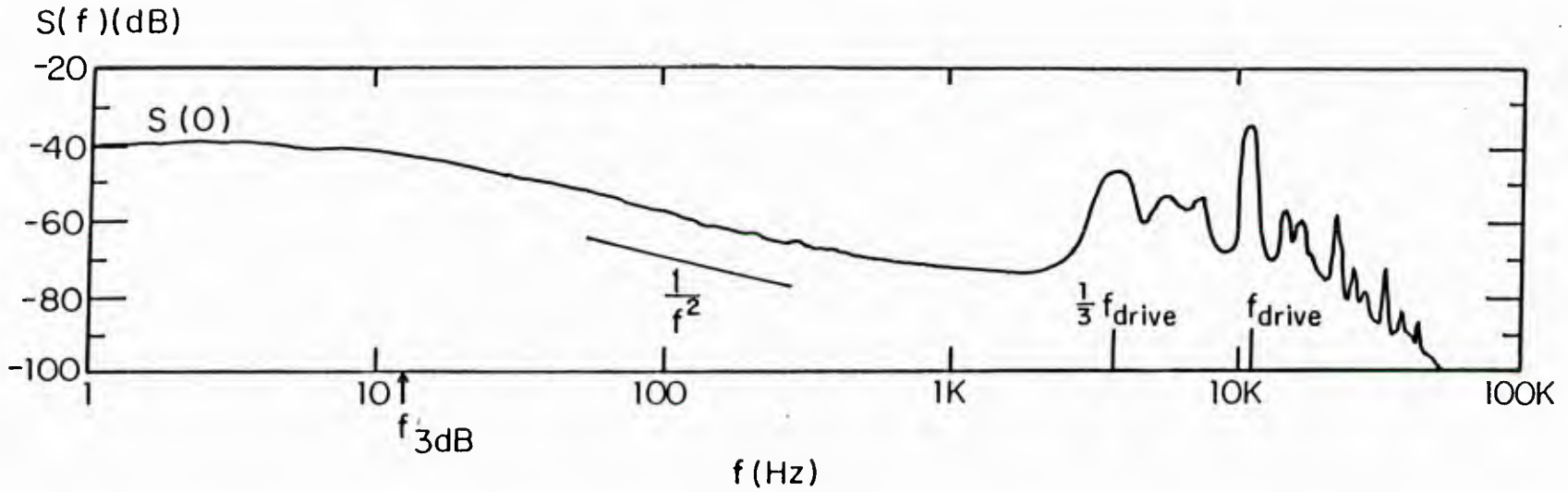

Fig. 5.16

Measured power spectrum from the analog simulation. The junction is biased at i_{dc}=0.17, i_{ac}=1.0, and f_L/f_p=1.07. The noise level corresponds to 50K thermal noise for the SNAP1 junction. The marked S(0) and f_{3dB} are defined as: S(0) = S(f=0), and $S(f_{3dB})=S(0)/2$.

From Fig. 5.16, we can see that the spectrum flattens out at the low frequency end (<10Hz), rolls off as $1/f^2$ in the intermediate frequency range (10Hz<f<1kHz), and rises again at high frequency, where it has peaks at $f_{drive}/3$ and f_{drive} and its harmonics. If we increase the amplitude of the noise current while keeping the other bias conditions unchanged, the onset frequency of the rolling-off (marked f_{3dB} in Fig. 5.16) will increase, while the spectral density at zero frequency [marked S(0) in Fig. 5.16] will in general decrease.

Machlup[71] derived a formula for the power spectrum of a random telegraph signal:

$$S(f) = 4\, V_{dc}^2 \frac{\tau^2}{(\tau_0 + \tau_1)} \frac{1}{1 + 4\pi^2 f^2 \tau^2} \qquad (5.11)$$

where S(f) is the mean-square voltage fluctuation per unit frequency, and V_{dc} is the voltage of the "on" state *1* (the voltage of the "off" state *0* is assumed to be zero), τ_0 and τ_1 are the mean lifetimes of the state *0* and *1* respectively, and

$$\frac{1}{\tau} = \frac{1}{\tau_0} + \frac{1}{\tau_1} \qquad (5.12)$$

Although it was derived in the assumption that both *0* and *1* are only dc states, (5.11) is certainly applicable to the power spectrum associated with a random switching between two ac Josephson steps as long as the frequency range concerned is far below the drive frequency. From Fig. 5.16 we can see that at the frequency region close to the drive, the spectrum is "skirted" by the 1/3 subharmonic of the drive frequency, and the resulting spectrum is substantially enhanced above the Lorentzian one.

Since the noise-induced switching between the two states is triggered by a noise current with a Gaussian distribution, we should expect the lifetimes τ_0 and τ_1 to take the form:

$$\tau_0 = \tau_{00} e^{\Delta E_0 / kT}$$
$$\tau_1 = \tau_{10} e^{\Delta E_1 / kT} \qquad (5.13)$$

where ΔE is the energy barrier which has to be overcome for the system to switch from one attractor to another, so ΔE determines the global stability[72] of the attractor concerned under finite perturbation. From the measured Lorentzian power spectrum at different noise levels, we should be able to measure the energy barriers ΔE_0 and ΔE_1 as well as the prefactors τ_{00} and τ_{10}.

For a Lorentzian spectrum, two quantities: S(0) and f_{3dB} contain all the information of the spectrum, where S(0) is the spectral density at the zero frequency and $f_{3dB}=1/2\pi\tau$ is the 3dB frequency at which $S(f_{3dB}) = S(0)/2$. Combining (5.11) and (5.12), we get relations between τ_0 and τ_1 and the measured quantities S(0) and f_{3dB}:

$$\tau_{0\pm} = \frac{1}{4\pi f_{3dB} C} [\, 1 \pm \sqrt{1-4C} \,]$$
$$\tau_{1\pm} = \frac{1}{4\pi f_{3dB} C} [\, 1 \mp \sqrt{1-4C} \,] \qquad (5.14)$$

where

$$C = \frac{\pi}{2} \frac{S(0)}{V_{dc}^2} f_{3dB} = \frac{\langle \delta V^2 \rangle}{V_{dc}^2} \qquad (5.15)$$

The second equation in (5.15) comes from the fact: For a Lorentzian spectrum (5.11), the mean-square voltage fluctuation is given by:

$$\langle \delta V^2 \rangle = \int_0^\infty S(f)\, df = V_{dc}^2 \frac{\pi}{2} S(0)\, f_{3dB} \qquad (5.16)$$

For a random telegraph signal which spends fraction f of time on state *1* and $(1-f)$ of time on state *0*, we have a simple result:

$$C = \frac{\langle \delta V^2 \rangle}{V_{dc}^2} = f(1-f) \qquad (5.17)$$

Apparently,

$$C_{max} = \frac{1}{4}$$

In this case, f =1/2, the system spends equal time on both states, so $\tau_0 = \tau_1$. For some power spectra taken at high levels of noise current, the calculated value of C from (5.15) is larger than 1/4, which makes Eq. (5.14) meaningless. This result comes from the fact that at high noise levels, f_{3dB} is so high that the onset of the rolling-off frequency is not far enough below the driving frequency and its subharmonics (cf. Fig. 5.16), to allow a clean separation of the Lorentzian; thus all the predictions above failed in this case.

Fig. 5.17 shows the normalized mean-square fluctuation $\langle \delta V^2 \rangle / V_{dc}^2$ deduced from the measured quantities S(0) and f_{3dB} through (5.15) vs. 1/T, where T is the effective noise temperature for the SNAP1 junction converted from the noise current in the simulation through Eq. (4.24). In the range of low noise levels $10 \le T \le 50$K ($0.02 \le 1/T \le 0.1 K^{-1}$), the amplitude of the fluctuating voltage goes to zero, indicating that the system spends most of its time in one attractor. On the other hand, at higher noise levels $50 \le T \le 200$K ($0.005 \le 1/T \le 0.02 K^{-1}$), the normalized mean-square fluctuation appoaches the theoretical maximum value, 0.25. This indicates that when strong noise triggered the system to switch back and forth between the two attractors frequently, the system spends rather even relative duty cycles on the two attractors. At very high noise levels, T>200K ($1/T < 0.005 K^{-1}$), the normalized mean-square fluctuation exceeds 0.25, indicating serious deviations of the power spectra from an ideal Lorentzian one occur due to the proximity of f_{3dB} to the subharmonic of the drive frequency [$f_{3dB} > 0.05(f_{drive}/3)$].

The lifetimes τ_0 and τ_1 deduced from the measured S(0) and f_{3dB} through (5.14) as functions of noise level 1/T are shown in Fig. 5.18, in which the dc and ac bias

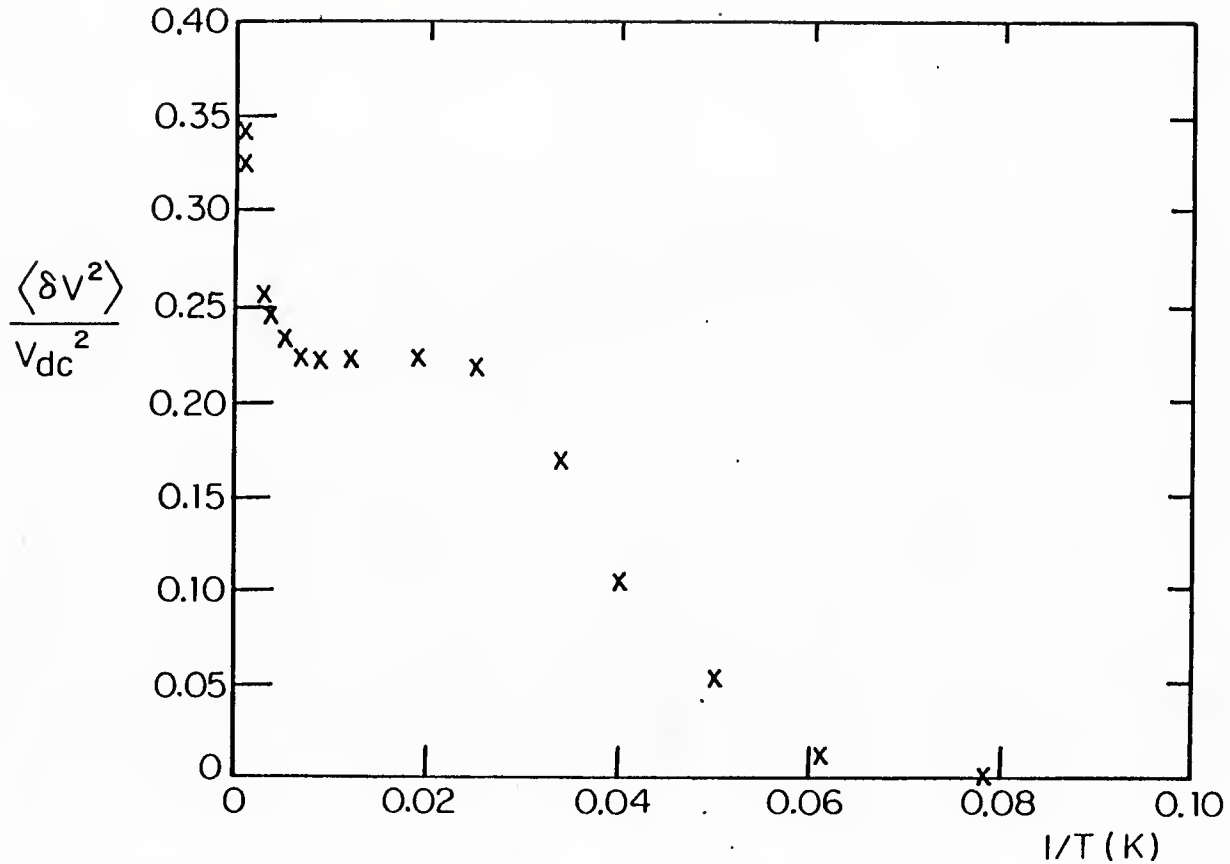

Fig. 5.17 Normalized mean-square fluctuation deduced from the measured quantities S(0) and f_{3dB} through (5.15) vs. the noise level. The dc and ac bias conditions are the same as those in Fig. 5.16.

conditions are the same as that in Fig. 5.16. All the data shown were taken from the power spectra with $f_{3dB} < 0.01(f_{drive}/3)$. This criterion guarantees that the low-frequency power spectra have at least one frequency decade of well-defined $1/f^2$ rolling-off; thus all the values of C calculated from (5.15) are smaller than 0.25.

The data in Fig. 5.18 showed an apparent linear dependence of $\log\tau_{\pm}$ on 1/T, especially at the small noise current end. There are some deviations between the data and the linear line at the high noise current end $1/T \leq 0.02$, which arise from the fact that the prefactors τ_{00} and τ_{10} in Eq. (5.13) can be only assumed constants in the low noise limit $\Delta E/kT >> 1$. When the noise level is comparable to the energy barrier, due to the frequent switching, τ_{00} and τ_{10}, which equal to the inverse product of the populations at the bottom of the potential wells times the attempt frequencies, will be functions of the noise level; thus $(\log\tau)$ will not vary linearly with (1/T) anymore. This is evidenced by the fact that in Fig. 5.18, the data of τ_+, which corresponds to a higher energy barrier (steeper slope of $\log\tau_+$ vs. 1/T than that of τ_-), deviates from the straight line at a higher noise level than that of τ_-.

The two sets of data in Fig. 5.18 are τ_+ and τ_- calculated from (5.14), they correspond to the lifetimes τ_0 and τ_1 of the two states, the 0th step and the 2/3 step. But from the measurement of power spectrum alone, we are not able to tell whether τ_+ or τ_- corresponds to τ_0, since if we reverse τ_0 and τ_1, the resulting power spectrum will be the same. However, by monitoring the time dependent voltage with an oscilloscope, we know that the system spends more time on the 0th step, thus we know that τ_+ (larger one) corresponds to τ_0, while τ_- corresponds to τ_1.

From the straight line which fits the data at the low noise end, we can calculate the energy barrier ΔE defined in (5.13):

$$\Delta E_0/k_B = 143K, \quad \Delta E_1/k_B = 43K$$

As a comparison, the Josephson coupling energy (the energy barrier in a dc case) for the

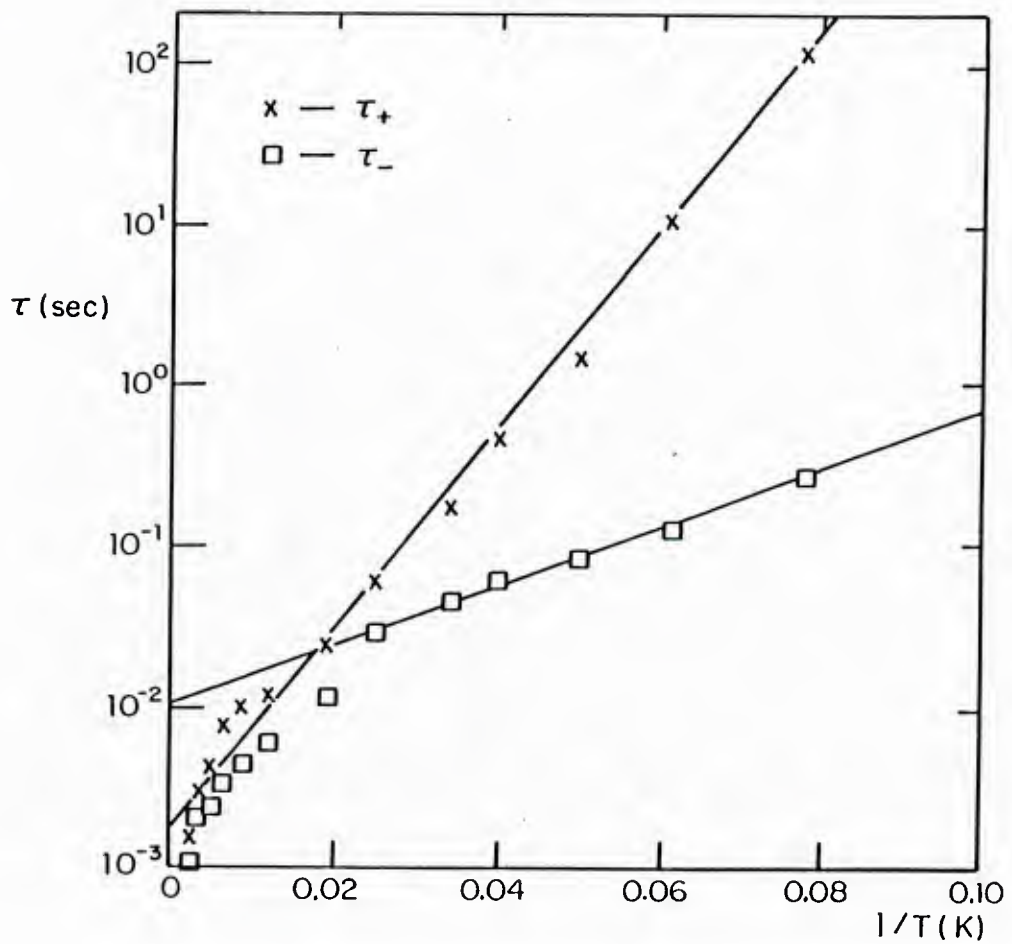

Fig. 5.18

Logarithmic plot of lifetimes deduced from the measured S(0) and f_{3dB} through (5.14) as functions of the noise temperature.

SNAP1 junction is 10^4K. The prefactors τ_{00} and τ_{10} in (5.13) are:

$$\tau_{00} = 1.5 \text{ msec.}, \quad \tau_{10} = 9.0 \text{ msec.}$$

The power spectra measured at other dc bias points than the one of Fig. 5.18 also showed the Lorentzian form. The corresponding lifetimes also have a clear exponential dependence on 1/T in the form of Eq. (5.13).

All these Lorentzian power spectra imply that the noise-induced intermittency between the 0th and 2/3 steps is a hopping process, in which the switching time is much shorter than the lifetimes τ_0 and τ_1 of the two states. The hopping process is very well characterized by a thermal activation model, based on the existence of an energy barrier between two stable states. Due to the bombardment of noise, the system occasionally hops over the barrier and gives rise to the fluctuating voltage of a random telegraph signal. This is not consistent with the 1/f power spectrum calculated from the digital simulation. The 1/f spectrum suggests that there is a long-lived intermediate state between the two states, 0th and 2/3 step. This intermediate state is perhaps a transient-chaotic state[72]. On the other hand, it may be relevant that the 1/f dependence was found in a frequency range closer to f_{drive} than that found reliable in the analog data.

5.6 Concluding remarks

In conclusion, we found that a Josephson junction exhibits rich chaotic phenomena when it is driven at or below its plasma resonance frequency. At this frequency, the qualitative features on I-V curves can be so sensitive to the drive/plasma frequency ratio f_L/f_p, that a few per cent change in f_L/f_p is enough to produce a clearly recognizable difference on I-V curves. This extreme sensitivity provides us a way of determining the experimental parameters f_L/f_p and i_{ac} much more accurately than estimates based on a very uncertain capacitance value. With the best chosen parameters and an appropriate amount of noise, we can reproduce the experimental results beautifully both in the qualitative features of the I-V curves such as the appearance of certain subharmonic

steps, and the quantitative features such as the width of the zeroth step. Aided by simulations, we found at certain noisy parts of I-V curves, the basin boundary has a very complicated fractal structure; its dimension d is closely related to the noise sensitivity, maximum d corresponds to a maximum noise power density measured in the experiment. The power spectra associated with the noise-induced switching are in general Lorentzian, with the lifetimes on each state being well characterized by a thermal activation model. The simulation also showed that noise-induced chaos is practically undistinguishable from intrinsic chaos in terms of the phase orbit.

CHAPTER VI

CONCLUSIONS

6.1 Summary and conclusions

We have demonstrated in experiments that a Josephson junction exhibits rich chaotic phenomena when it is driven at or below its plasma resonance frequency. This experiment is the first of its kind in the far-infrared frequency range, where the radiation frequency is close to the superconducting gap frequency, and it shows some unique features at this frequency range.

a) In addition to the nonlinear Josephson current-phase relation, there is an extra nonlinearity associated with the gap structure of the quasiparticle I-V characteristic. The effect of this nonlinearity becomes important in the far-infrared frequency range, where the ac Josephson steps are close to the gap voltage.

b) The levels of shot noise associated with the finite voltage steps and the zero point fluctuations at this frequency range are comparable to or larger than the thermal noise of the ambient temperature. This non-thermal noise needs to be to be taken into account when we study the effect of noise on a driven Josephson junction in a highly nonlinear regime.

We have studied the above features by a combination of experimental and simulational work.

a) In our simulations, we approximate the complicated nonlinear structure of the quasiparticle I-V characteristic by a piecewise nonlinear resistance, which turns out to work surprisingly well. By choosing the right values of other parameters (f_L/f_p, for example) in our simulations, we could reproduce the experimental results very well both in those qualitative features such as the appearance of certain subharmonic steps, and the quantitative features such as the variation of the step width vs. laser power. The good

agreement between the simulations based on such a simple nonlinear resistance and the experimental results from a much more complicated nonlinear resistance indicates that if the radiation frequency is comparable to the gap frequency, the spacing between the ac Josephson steps is so large compared to the nonlinear region at the gap that the detailed nonlinear structure at the gap is not important as long as the piecewise resistance resembles the quasiparticle I-V characteristic far away from the gap.

b) In the noiseless simulations, we often found that the simulated I-V curve shows hysteresis which can be removed by adding some noise in the simulations. We found that it is necessary to insert a noise current with an effective noise temperature higher than that of the ambient temperature in the experiment even after taking into account the large disparity of the number of averaging cycles between the experiment and the simulation. This higher noise level can be largely accounted for by the shot noise associated with the high voltage level of the ac Josephson steps at far-infrared frequencies and the zero point fluctuations at the same frequency range if we use a complete noise power spectrum including the shot noise and the quantum fluctuations.

One of our main discoveries is that when the radiation frequency f_L is close to the Josephson plasma resonance frequency f_p, the response of the junction to the radiation is so sensitive to the drive/plasma frequency ratio f_L/f_p that a 10% change in f_L/f_p, say, from f_L/f_p=0.97 to f_L/f_p=1.07, will make the I-V curves of the irradiated junction qualitatively different from each other. For example, one shows the 2/3 step (f_L/f_p=0.97), and the other shows the 1/2 step (f_L/f_p=1.07). These qualitative features of the I-V curves can serve as a "fingerprint" for each junction since certain features only appear for a very narrow parameter range. By reproducing these fingerprints in simulations, we can determine the parameters (especially f_p) of the junctions to a higher precision than the estimates based on some precision-limited parameters such as the capacitance. A precise determination of the experimental parameters is very crucial for our studies of nonlinear dynamic effects

exhibited by the junctions; since at this high frequency (200-600GHz), we cannot measure directly the phase motion, all we can measure is some long-time averaged quantities such as the dc I-V curves and low frequency power spectrum. The only way we can understand those observed chaotic phenomena is to study the phase motion of the system in a much slower simulation. The qualitity of such studies apparently depends heavily on how precisely we can model the real Josephson junction system in our simulations.

Aided by simulations, we found that apparently similar noisy I-V curves can be due to quite different mechanisms. Some of them are due to intrinsic chaos; the simulation showed that the phase motion of the system is chaotic even in the absence of noise. But some of them are due to the noise-induced intermittent switching between several co-existent attractors. For example, under the particular bias conditions: f_L/f_p=1.07, i_{ac}=1.0, the I-V curve has a hysteretic loop between the 0th and 2/3 steps; the digital simulation studies reveal that in that loop the basin boundary of attraction is fractal. The dimension d of this fractal boundary varies with the dc bias current, and d is close to 2 at a certain range of dc bias current, meaning that much of the phase space is composed of the basin boundary. Any random noise input makes the system wander between the two attractors, giving rise to a high noise output. The coincidence of the maximum d and the peak of the measured noise density has been observed.

The studies of the power spectrum at the above bias conditions reveal a different story: The power spectra with noise-triggered switching are in general Lorentzian, meaning the switching is a hopping process; the system randomly hopps from one state to another with mean lifetims τ_0 and τ_1 on each state. The linear dependence of logτ on 1/T indicates that there is an energy barrier separating the two bistable states. The system has to hop over this energy barrier to switch from one state to another. The energy barriers ΔE_0 and ΔE_1, measured from the state *0* and *1* respectively, determine the lifetimes of the system at *0* and *1* under finite perturbations. These energy barriers are functions of the

bias conditions. It is possible that it is the variation of the energy barriers with the dc bias current, rather than the variation of the fractal dimension, that is responsible for the peak of the measured noise density in the experiment.

6.2 Future work

It would be incomplete to end this report without mentioning potential future work in related fields:

The study of Josephson junction arrays has been very active in the past few years because of their potential applications. However, despite the large amount of work done in this field[73], many questions remain to be answered. For example, an array with N identical junctions spaced much closer than the radiation wavelengths should be equivalent to a single junction whose plasma frequency ω_p and McCumber parameter β_c are the same as those of a single junction in the array; thus this junction array should behave the same way as that of the single junction except the voltage scale is N times bigger. Particularly, if the parameters of a single junction in the array are in a chaotic regime, we should expect the whole array to behave chaotically in the same way. In trying to verify these speculations in experiments, we can gain some futher understanding of the nature of a driven nonlinear system.

Our studies of the chaotic behaviors of Josephson junctions driven at far-infrared frequencies have been limited to a few frequencies. This is mainly because the radiation source (optically-pumped-laser) is not a continously tunable source, and our antenna is a narrow-band resonance device.

The bow-tie antenna[74] is a broadband coupling antenna. Its impedance is purely resistive and independent of frequency. Also, its coupling efficiency is supposed to be 6dB[74] better than that of a dipole antenna at resonance. It has been reported[75] that a bow-tie antenna was used to couple a SIS mixer to far-infrared radiation at 116-466 GHz.

However, no direct comparison has been made between the performance of the bow-tie antenna with other types of antenna at such high frequencies. Our own experience with the bow-tie antenna seems to show that it is not as efficient in coupling radiation as a half-wave dipole antenna at its resonant frequency. For example, the I-V curve we measured from a Sn-Pb junction attached to a bow-tie antenna irradiated by 604 GHz radiation exhibited up to the 6th ac Josephson step, while similar junctions attached to a dipole antenna in ref. 49 showed up to 7th step. We can not say for sure from this result that the bow-tie antenna is less efficient than the dipole antenna because there are other factors determining the coupling as well. One of the reasons for this lesser coupling might be a larger capacitive shunting of a bigger cross sectional area of our junctions compared to that of ref. 49. Although these junctions were fabricated in a similar process, the areas can differ from junction to junction by a factor of five (cf. Table 4.2 in ref. 49).

The log-periodic antenna[76] is a broadband coupling antenna like the bow-tie antenna but has its main radiation lobe perpendicular to its plane. In contrast, the main lobe of the bow-tie antenna is about 30 degrees from the normal of the antenna plane which makes an optimized coupling difficult. It has been suggested[77] that the log-periodic antenna is a better candidate for far-infrared coupling than the bow-tie antenna.

A tunable local oscillator would be an ideal radiation source to study Josephson effects. Among the many candidates based on Josephson oscillation, two seem to be particularly promising.

a) Josephson junction arrays. Compared to a single junction, Josephson junction arrays have advantages: i) larger dynamic range and thus larger radiation power; ii) higher impedance, thus a better impedance match to free space; iii) more coherent radiation, i.e. narrower linewidth of radiation. However, in order to obtain a coherent radiation, the dimension of the array has to be a small fraction of the wavelength. This puts a serious limitation on the number of junctions, especially at far-infrared frequencies, where the

wavelength is less than a few millimeters. One way to solve this problem is to place the junctions in the array one wavelength from each other[78]. However, this arrangement will seriously limit the tunability of the radiation frequency, making the junction array at best a multi-frequency generator instead of a continuously tunable oscillator.

b) Flux-flow oscillator. By applying a magnetic field on a long one-dimensional dc-biased Josephson junction, the inverse Lorentz force exerted on the fluxes will force them to flow to one direction. The influence of this flux flow on an adjacent junction is like a radiation field, thus inducing a set of ac Josephson steps as well as the photon-assisted-tunneling steps on the I-V curves of the adjacent junction. It has been reported[79] that the coupled power of such flux flow can be as large as 1μW over the frequency range of 100-400GHz.

In summary, we have observed chaotic behaviors of single Josephson junctions driven at far-infrared frequencies. Our experimental data agree well with the results of the simulation based on the RCSJ model and modified to include the nonlinearity of the quasiparticle I-V characteristic and the quantum noise. Much work remains to be done to extend this work to a broader frequency range and multi-junction arrays.

REFERENCES

1. B.D. Josephson, Phys. Lett. 1, 251 (1962b).
2. N.R. Werthamer, Phys. Rev. 147, 255 (1966).
3. Mitchell J. Feigenbaum, J. Stat. Phys. 19, 25 (1978).
4. P. Manneville and Y. Pomeau, Phys. Lett. 75A, 1 (1979); Y. Pomeau and P. Manneville, Commun. Math. Phys. 74, 189 (1980).
5. Scott J. Shenker, Physica 5D, 405 (1982); David Rand and Stellan Ostlund, James Sethna, and Eric D. Siggia, Phys. Rev. Lett. 19, 132 (1982); Mitchell J. Feigenbaum, Leo P. Kadanoff, Scott J. Shenker, Physica 5D, 370 (1982); Thomas Bohr, Per Bak, and Mogens Høgh Jensen, Phys. Rev. A30, 1970 (1984).
6. B.A. Huberman, J.P. Crutchfield and N.H. Packard, Appl. Phys. Lett. 37, 750 (1980).
7. N.F. Pedersen and A. Davidson, Appl. Phys. Lett. 39, 830 (1981).
8. M. Cirillo and N.F. Pedersen, Phys. Lett. 90A, 150 (1982).
9. D. D'Humieres, M.R. Beasley, B.A. Huberman, and A. Libchaber, Phys. Rev. A26, 3483 (1982).
10. Miguel Octavio, Phys. Rev. B29, 1231 (1984).
11. R.L. Kautz, J. Appl. Phys. 52, 3528 (1981).
12. R.L. Kautz, J. Appl. Phys. 52, 6241 (1981).
13. W.J. Yeh and Y.H. Kao, Phys. Rev. Lett. 49, 1888 (1982); W.J. Yeh and Y.H. Kao, Appl. Phys. Lett. 42, 299 (1983); W.J. Yeh and Y.H. Kao, Phys. Rev. Lett. 52, 480 (1984).
14. P. Alstrøm and M.T. Levinsen, Phys. Rev. B31, 2753 (1985).
15. Robert F. Miracky, John Clarke, and Roger H. Koch, Phys. Rev. Lett. 50, 856

(1983).

16. V.N.Gubankov, K.I. Konstantinyan, V.P. Koshelets, and G.A. Ovsyannikov, IEEE Trans. MAG-19, 637 (1983);

17. M. Octavio and C. Readi Nasser, Phys. Rev. B30, 1586 (1984).

18. Qing Hu, J.U. Free, M. Iansiti, O. Liengme, and M. Tinkham, IEEE Trans. MAG-21, 590 (1985).

19. D.C. Cronemeyer, C.C. Chi, A. Davidson, and N.F. Pedersen, Phys. Rev. B31, 2667 (1985); C. Vanneste, C.C. Chi, and D.C. Cronemeyer, Phys. Rev. B32, 4796 (1985).

20. A. Davidson, B. Dueholm, and M.R. Beasley, Phys. Rev. B33, 5127 (1986).

21. M. Tinkham, M. Octavio, and W.J. Skocpol, J. Appl. Phys. 48, 1311 (1977).

22. A.J. Leggett, Prog. Theor. Phys. (Suppl.) 69, 80 (1980);
A.O. Caldeira and A.J. Leggett, Phys. Rev. Lett. 46, 211 (1981).

23. R.F. Voss and R.A. Webb, Phys. Rev. Lett. 47, 647 (1981).

24. L.D. Jackel, J.P. Gordon, E.L. Hu, R. E. Howard, L.A. Fetter, D.M. Tennant, R.W. Epworth, and J. Kurkijarvi, Phys. Rev. Lett. 47, 697 (1981).

25. John M. Martinis, Michel H. Devoret, and John Clarke, Phys. Rev. Lett, 55, 1543 (1985).

26. A.H. Dayem and R.J. Martin, Phys. Rev. Lett. 8, 246 (1962);
P.K. Tien and J.P. Gordon, Phys. Rev. 129, 647 (1963).

27. Sidney Shapiro, Andre R. Janus, and Sandor Holly, Rev. Mod. Phys. 36, 223 (1964).

28. D.A. Weitz, W.J. Skocpol, and M. Tinkham, Appl. Phys. Lett. 31, 227 (1977);
D.A. Weitz, W.J. Skocpol, and M. Tinkham, Phys. Rev. B18, 3282 (1978).

29. W.C. Danchi, F. Habbal, and M. Tinkham, Appl. Phys. Lett. 41(9), 883 (1982).

30. V.N. Belykh, N.F. Pedersen and O.H. Soerensen, Phys. Rev. B16, 4853

(1977).

31. R.L. Kautz and R. Monaco, J. Appl. Phys. 57, 875 (1985).

32. R.L. Kautz, to appear in J. Appl. Phys.

33. V.N. Gubankov, S.L. Ziglin, K.I. Konstantinyan, V.P. Koshelets, and G.A. Ovsyannikov, Sov. Phys. JETP 59, 198 (1984).

34. M. Bartuccelli, P.L. Christiansen, N.F. Pedersen, and M.P. Soerensen, Phys. Rev. B33, 4686 (1986).

35. M. Tinkham, p194 & p34, "Introduction to Superconductivity", McGraw-Hill, New York, 1975.

36. Vinay Ambegaokar and B.I. Halperin, Phys. Rev. Lett. 22, 1364 (1969).

37. Michael Stephen, Phys. Rev. 182, 531 (1969);
Michael Stephen, Phys. Rev. 186, 393 (1969).

38. Patrick Lee, J. Appl. Phys. 42, 325 (1971).

39. H.A. Kramers, Physica, 7, 284 (1940).

40. C.M. Falco, W.H. Parker, S.E. Trullinger, and Paul K. Hansma, Phys. Rev. B10, 1865 (1974).

41. T.A. Fulton and L.N. Dunkleberger, Phys. Rev. B9, 4760 (1974).

42. W.C. Danchi, J. Bindslev Hansen, M.Octavio, F. Habbal, and M. Tinkham, Phys. Rev. B30, 2503 (1984).

43. Qing Hu, C.J. Lobb, and M. Tinkham, to appear in Phys. Rev. B (1987).

44. W.H. Henkels and W.W. Webb, Phys. Rev. Lett. 26, 1164 (1971).

45. M. Iansiti, Qing Hu, R.M. Westervelt, and M. Tinkham, Phys. Rev. Lett. 55, 746 (1985).

46. A.J. Dahm, A. Denenstein, D.N. Langenberg, W.H. Parker, D. Rogovin, and D.J. Scalapino, Phys. Rev. Lett. 26, 1416 (1969).

47. Richard F. Voss and Richard A. Webb, Phys. Rev. B24, 7447 (1981).

48. David A. Weitz, Technical Report No. 14, (Tinkham series, Div. of Appl. Sci., Harvard University, 1978).

49. W.C. Danchi, Technical Report No. 22, (Tinkham series, Div. of Appl. Sci., Harvard University, 1983)

50. D.W. Jillie, L.N. Smith, H. Kroger, L.W. Currier, R.L. Payer, C.N. Potter, and D.M. Shaw, IEEE J. Sol. St. circuits SC-18, 173 (1983);
D.W. Jillie, L.N. Smith, and H. Kroger, IEEE Trans. MAG-19, 1170 (1983).

51. L.N. Smith, J.B. Thaxter, D.W. Jillie, and H. Kroger, IEEE Trans. MAG-18, 1571 (1982);
L.N. Smith, H. Kroger, and D.W. Jillie, IEEE Trans. MAG-19, 787 (1983).

52. Greg E. Blonder, Technical Report No. 19, (Tinkham series, Div. of Appl. Sci., Harvard University, 1982).

53. L.N. Smith, private communication.

54. Optovac, data sheet.
Janos, data sheet.

55. Ronald W.P. King, "The Theory of Linear Antennas", Harvard University Press, Cambridge, Massachusetts, 1956; Ronald W.P. King and Charles W. Harrison, "Antenna and Waves", The M.I.T. Press. Cambridge, Massachussets.

56. Ronald W.P. King, private communication.

57. K. Mizuno, Y. Daiku, and S. Ono, IEEE Trans. MTT-25, 470 (1977).

58. Henry W. Ott, "Noise Reduction Techniques in Electronic Systems", John Wiley & Sons, New York.

59. C.T. Rogers and R.A. Buhrman, Phys. Rev. Lett. 53, 1272 (1984).

60. C.A. Hamilton, Rev. Sci. Instrum. 43, 445 (1972); C.K. Bak and N.F. Pederson, Appl. Phys. Lett. 22, 149 (1973); C.K. Bak, Revue Phys. Appl. 9, 15 (1974); J.C. Taunton and M.R. Halse, J. Phys. E10, 505 (1977); A. Yagi

and I. Kurosawa, Rev. Sci. Instrum. 51, 41 (1980).

61. Richard W. Henry and Daniel E. Prober, Rev. Sci. Instrum. 52, 902 (1981).

62. J.H. Magerlein, Rev. Sci. Instrum. 49(4), 486 (1978).

63. W.C. Stewart, Appl. Phys. Lett. 12(8), 277 (1968).

64. H. Akoh, O. Liengme, M. Iansiti, M. Tinkham, and J.U. Free, Phys. Rev. B33, 2038 (1986).

65. M. Octavio, private communication.

66. Cornell Chun, private communication.

67. W.C. Danchi, J.U. Free, F. Habbal, M. Tinkham, and L.N. Smith, IEEE, Trans. MAG-21, 219 (1985).

68. C. Grebogi, S.W. McDonald, E. Ott, and J.A. Yorke, Phys. Lett. 99A, 415 (1983);

C. Grebogi, E. Ott, and J.A. Yorke, Physica 7D, 181 (1983).

69. B.B. Mandelbrot, *Fractals -- Form, Chance and Dimension* (Freeman, San Francisco, 1977).

70. E.G. Gwinn and R.M. Westervelt, Phys. Rev. Lett. 54, 1613 (1985).

71. Stefan Machlup, J. Appl. Phys. 25, 341 (1954).

72. R.L. Kautz, private communication.

73. A.K. Jain, K.K. Likharev, J.E. Lukens, and J.E. Sauvageau, Phys. Reports, 109, 309 (1984).

74. D.B. Rutledge, and M.S. Muha, IEEE Trans. AP-30, 535 (1982).

75. M.J. Wengler, D.P. Woody, R.E. Miller, and T.G. Phillips, Inter. J. Infrared and Millimeter Wave, 6, 697 (1985).

76. R.H. DuHamel and D.E. Isbell, IRE Natl. Conv. Record, Pt. 1, 119 (1957).

77. M.J. Wengler, private communication.

78. J.E. Sauvageau, and J.E. Lukens, Proc. 1986 Applied Superconductivity

Conference.

79. T. Nagatsum, K. Enpuku, F. Irie, and K. Yoshida, J. Appl. Phys. 54, 3302 (1983);

T. Nagatsum, K. Enpuku, K. Yoshida, and F. Irie, J. Appl. Phys. 56, 3248 (1984).

ACKNOWLEDGEMENT

The author owes much thanks to his numerous colleagues and friends during this work; without them, this experience would not have been nearly as enjoyable.

I would first like to thank my advisor Prof. M. Tinkham for providing the steady guidance and the encouragement throughout this work. His insistence on careful analysis and clear presentation has always been a key factor in turning a set of raw data into clear and meaningful results. Also, his rigorous, word-by-word critical reading always makes my manuscripts more digestable to readers.

I would also like to thank my other advisor Prof. Chris Lobb for his invaluable academic advice, technical help, and constant encouragement during this work. Chris has helped me with his expertise on many subjects, quite often in a humorous manner. Also, he remembers every word I said many years ago no matter how meaningless it was.

Dr. Jørn Binslev Hansen and Dr. W.C. Danchi were instrumental in helping me get started on the experimental track. Jørn taught me how to operate the far-infrared laser while he was learning himself. I learned the optical microfabrication techniques from Bill.

I would like to thank Marco Iansiti and John Free, whose digital simulations compose part of this work.

I would like to thank the many people whom I shared the lab with during the past years. They have provided a friendly, cooperative, challenging, and sometimes stimulating atmosphere in the lab. Among them, Martin Forrester is a special friend. He has givien selfless help whenever I need it. I would also like to thank my office mates over the past few years. James Gordon introduced me to the group while we were sharing an office in Jefferson. Charlie Johnson has shared a pleasant office as well as a taste for spicy Chinese food with me in the past year.

Louis DeFeo always quickly transformed my drawings into useful objects.

I would like to thank specially Prof. T.D. Lee of Columbia University for the CUSPEA (China-U.S. Physics Examination and Application) program he sponsored, through which I came to Harvard; without this program, this work would be unimaginable.

Finally, I would like to thank my parents for their great sacrifice for sending me to pursue higher education overseas, and the tremendous emotional support they have provided throughout this work. This work is dedicated to them.

This research was supported by the U.S. Office of Naval Research under Contract No. N00014-83-K-383 and by the Joint Services Electronic Program under Contract No. N00014-84-K-0465.